

Characterization of High Temperature Polymer Electrolyte Fuel Cells

Yasser Rahim

Energie & Umwelt / Energy & Environment

Band / Volume 437

ISBN 978-3-95806-359-4

“Characterization of High Temperature Polymer Electrolyte Fuel Cells”

“Charakterisierung von Hochtemperatur-Polymerelektrolyt-Brennstoffzellen”

Von der Fakultät für Maschinenwesen der Rheinisch-Westfälischen Technischen Hochschule Aachen zur Erlangung des akademischen Grades eines Doktors der Ingenieurwissenschaften genehmigte Dissertation

vorgelegt von

Yasser Rahim

Berichter: Univ.-Prof. Dr. rer. nat. Werner Lehnert

Univ.-Prof. Dr.-Ing. Lorenz Singheiser

Tag der mündlichen Prüfung: 26.09.2018.

Forschungszentrum Jülich GmbH
Institut für Energie- und Klimaforschung
Elektrochemische Verfahrenstechnik (IEK-3)

Characterization of High Temperature Polymer Electrolyte Fuel Cells

Yasser Rahim

Schriften des Forschungszentrums Jülich
Reihe Energie & Umwelt / Energy & Environment

Band / Volume 437

ISSN 1866-1793

ISBN 978-3-95806-359-4

Bibliografische Information der Deutschen Nationalbibliothek.
Die Deutsche Nationalbibliothek verzeichnet diese Publikation in der
Deutschen Nationalbibliografie; detaillierte Bibliografische Daten
sind im Internet über <http://dnb.d-nb.de> abrufbar.

Herausgeber
und Vertrieb: Forschungszentrum Jülich GmbH
 Zentralbibliothek, Verlag
 52425 Jülich
 Tel.: +49 2461 61-5368
 Fax: +49 2461 61-6103
 zb-publikation@fz-juelich.de
 www.fz-juelich.de/zb

Umschlaggestaltung: Grafische Medien, Forschungszentrum Jülich GmbH

Druck: Grafische Medien, Forschungszentrum Jülich GmbH

Copyright: Forschungszentrum Jülich 2018

Schriften des Forschungszentrums Jülich
Reihe Energie & Umwelt / Energy & Environment, Band / Volume 437

D 82 (Diss., RWTH Aachen University, 2018)

ISSN 1866-1793
ISBN 978-3-95806-359-4

Vollständig frei verfügbar über das Publikationsportal des Forschungszentrums Jülich (JuSER)
unter www.fz-juelich.de/zb/openaccess.



This is an Open Access publication distributed under the terms of the [Creative Commons Attribution License 4.0](https://creativecommons.org/licenses/by/4.0/),
which permits unrestricted use, distribution, and reproduction in any medium, provided the original work is properly cited.

Characterization of High Temperature Polymer Electrolyte Fuel Cells

by Yasser Rahim

Abstract

A Fuel cell is a clean and efficient energy converting device. High temperature polymer electrolyte fuel cell (HT-PEFC) is a particular type of fuel cell which offers fuel flexibility and system level simplicity. It is considered to be a viable solution for the transition period from a fossil fuel based economy to a sustainable, renewable energy based economy due to its potential to be efficiently utilized in combined heating and power, transport and backup power applications where fossil fuels continue to play a significant role.

This thesis concentrates on development of methods and strategies to quantify performance related electrochemical parameters in HT-PEFC membrane electrode assemblies (MEA) at the single cell level. Both commercial and in-house assembled MEAs are utilized for this purpose. The in-house assembled MEAs are used for characterizing the most important material parameters for the HT-PEFC MEAs such as the platinum (Pt) loading, cathode catalyst layer (CCL) thickness and the phosphoric acid doping level (PADL) of the MEA. The parameter settings for maximum cell performance are systematically determined. An MEA with these parameters is used for investigating the effect of hydrogen and oxygen content in the anode and cathode streams respectively on cell impedance.

The commercial MEAs are used to study the effect of various operating conditions on fuel cell performance. The design of experiments (DoE) is utilized to analyze the effect of various operating conditions on four different MEAs and regression models for each of the MEAs are developed for a comparison of the effect of sample size on the accuracy of the regression models. It is determined that a small sample size is accurate enough for an initial screening design, which can reduce the experimental effort by one-sixth, thus saving valuable time and resources.

An accelerated degradation study is conducted on two different commercial MEAs to study the dominant degradation mechanisms for the HT-PEFC MEA. Various stressors are used for both MEA types for 100 hours. Polarization curves, EIS data and cyclic voltammetry data before and after stressor operation are compared and analyzed. Thermal cycling, high temperature operation and high cathode stoichiometry are determined to be the most effective stressors related to loss of phosphoric acid, loss of platinum surface area and carbon corrosion as the degradation mechanisms.

Charakterisierung von Hochtemperatur-Polymerelektrolyt-Brennstoffzellen

von Yasser Rahim

Kurzfassung

Eine Brennstoffzelle ist ein sauberer und effizienter Energiewandler. Die Hochtemperatur-Polymerelektrolyt-Brennstoffzelle (HT-PEFC) ist ein spezieller Typ Brennstoffzelle, der Brennstoffflexibilität und einen einfachen Systemaufbau bietet. Sie wird als eine praktikable Lösung für den Übergang von einer auf fossilen Brennstoffen basierenden Wirtschaft zu einer nachhaltigen, auf erneuerbaren Energien basierenden Wirtschaft angesehen, da sie in Kraft-Wärme-Kopplung, Transport- und Notstromanwendungen, in denen fossile Brennstoffe weiterhin eine bedeutende Rolle spielen, effizient genutzt werden kann.

Diese Arbeit konzentriert sich auf die Entwicklung von Methoden und Strategien zur Quantifizierung leistungsbezogener elektrochemischer Parameter in HT-PEFC Membran-Elektroden-Einheiten (MEA) auf Einzelzellebene. Zu diesem Zweck werden sowohl kommerzielle als auch intern hergestellte MEAs verwendet. Die selbst assemblierten MEAs werden zur Charakterisierung der wichtigsten Materialparameter für die HT-PEFC MEAs wie die Platin- (Pt) Beladung, die Kathodenkatalysatorschichtdicke und der Phosphorsäure-Dotierungsgrad der MEA verwendet. In einer Studie werden die Parameter systematisch variiert und die Kombination ermittelt, die insgesamt zu einem Leistungsmaximum im untersuchten Bereich führt. Eine MEA mit diesen optimalen Parametereinstellungen wird verwendet, um die Wirkung des Wasserstoff- und Sauerstoffgehalts in den Anoden- und Kathodenströmen auf die Zellimpedanz zu untersuchen.

Die kommerziellen MEAs werden verwendet, um die Auswirkung verschiedener Betriebsbedingungen auf die Brennstoffzellenleistung zu untersuchen. Die Statistische Versuchsplanung wird verwendet und Regressionsmodelle für jede der MEAs werden für einen Vergleich der Auswirkung der Stichprobengröße auf die Genauigkeit der Regressionsmodelle entwickelt. Es wird festgestellt, dass eine kleine Stichprobengröße für ein anfängliches Screening-Design ausreichend genau ist, was den experimentellen Aufwand auf ein Sechstel reduzieren kann und somit wertvolle Ressourcen spart.

Eine Studie zur beschleunigten Alterung wird an zwei verschiedenen kommerziellen MEAs durchgeführt, um die dominanten Alterungsmechanismen für die HT-PEFC MEA zu untersuchen. Beide MEAs werden verschiedenen Stressfaktoren über 100 Stunden ausgesetzt. Polarisationskurven, Impedanzdaten und Daten aus der Zyklischen Voltammetrie vor und nach der Stressphase werden miteinander verglichen und analysiert. Thermische Zyklisierung, Hochtemperaturbetrieb und hohe Kathodenstöchiometrie werden als die effektivsten Stressfaktoren im Zusammenhang mit Phosphorsäureverlust, Verlust der Platinoberfläche und Kohlenstoffkorrosion als Alterungsmechanismen bestimmt.

Contents

1	Introduction and Literature Review	1
1.1	Polymer electrolyte membrane fuel cells (PEFC)	2
1.1.1	Comparison of LT-PEFC and HT-PEFC	8
1.1.2	Challenges faced by the HT-PEFC and current research	9
1.2	Motivation and experimental goals	11
2	Experimental Methods	13
2.1	Design of Experiments (DoE)	13
2.1.1	One factor at a time (OFAT) method and DoE comparison	13
2.1.2	DoE approaches and methodology	15
2.2	Electrochemical impedance spectroscopy (EIS)	20
2.2.1	EIS basics	20
2.2.2	Equivalent circuit models (ECM) for EIS data analysis	23
2.2.3	Analytical modeling for EIS data analysis	25
3	Experimental Setup and Procedures	29
3.1	Test cells	29
3.1.1	Break-in Procedure and BOL and EOL data acquisition	32
3.1.2	UI curve	33
3.2	Test station	34
3.3	EIS and CV measurement equipment and settings	37
3.3.1	EIS measurements	38
3.3.2	CV measurements	38
4	Commercial MEA Characterization	41
4.1	HT-PEFC MEA characterization with DoE	41
4.1.1	Detailed calculation procedure for MEA D	43
4.1.2	Comparison of regression coefficients and discussion	49
4.2	MEA degradation	52
4.3	Summary	55
5	In-house Assembled MEA Study	57
5.1	Material parameters and MEA preparation	57
5.1.1	Material parameters	57

5.1.2 MEA preparation	59
5.2 DoE study	61
5.2.1 Experimental	61
5.2.2 Results	62
5.3 EIS study	81
5.3.1 Experimental	81
5.3.2 Results	82
5.4 Summary	88
6 Effects of Anode and Cathode Gas Concentration on Cell Impedance	89
6.1 Experimental	89
6.2 UI curves and Nyquist plots	90
6.3 Comparison of fitting results	97
6.3.1 Hydrogen concentration change with air on the cathode side	97
6.3.2 Hydrogen concentration change with oxygen on the cathode side	100
6.3.3 Oxygen concentration change with hydrogen on the anode side	103
6.4 Summary	106
7 Accelerated Degradation Study	109
7.1 Experimental	109
7.1.1 Stressors and their implementation	110
7.1.2 Benchmarking with BOL UI and U_t curves for constant current density operation ...	111
7.2 Results	114
7.2.1 UI curves and degradation rate comparison (AAM MEA)	115
7.2.2 UI curves and degradation rate comparison (APM MEA)	116
7.2.3 EIS and CV analysis	119
7.3 Summary	124
8 Discussion and Conclusions	127
8.1 Discussion	127
8.2 Conclusions	132
Nomenclature	133
Bibliography	138
List of Figures	155

List of Tables.....160

Acknowledgments161

1 Introduction and Literature Review

The fossil fuel based economy is not sustainable. Besides that, the depleting resources of fossil based fuels, the dependence on politically unstable foreign nations for its supply and the global warming caused by its consumption make the fossil fuel economy unattractive as a long term choice [1]. Although there is disagreement about the way forward, the foreseeable implications of climate change on the society [2–4] more or less necessitate immediate action.

Fuel cell technology offers realistic hope of decarbonizing the energy sector in our quest to mitigate the environmental impact of the industrial age [5]. Renewable energy resources like wind and solar energy, coupled with fuel cells and electrolyzers form the basis of the envisaged environment friendly and sustainable hydrogen based economy [6]. The road ahead however, is not without its fair share of obstacles. On one hand, the intermittent nature of the renewable energy sources is challenging for grid compatibility and storage, while on the other hand, electrolyzers and fuel cells are far from being commonplace at the moment, with cost, performance and lifetime being the main hurdles to commercialization and subsequent widespread utilization [7].

Fuel cells are clean energy converting devices. They present many advantages in comparison to conventional energy converting devices like internal combustion engines (ICE). They convert the chemical energy of the fuel directly to electrical energy by means of an electrochemical reaction and thus have the potential for high efficiency, especially in the low power range. They don't have moving parts so they are quiet and do not need frequent maintenance. If hydrogen is used as a fuel, there is no emission of greenhouse gases (GHG) and if a fossil based fuel is used, the emission is still lower than comparable conventional energy sources [8]. Fuel cells find many applications in the energy sector such as portable, transport and stationary power.

In its simplest form, a fuel cell consists of two electrodes (anode and cathode) separated by an electrolyte material. An electrochemical reaction is separated into two parts by using a catalyst and the electrolyte. One of these reactions takes place at the anode side and the other at the cathode side of the fuel cell. Since the electrolyte material conducts only ions but not electrons, the electrons are forced to travel to the other side of the fuel cell through a load. This flow of electrons is then harnessed as electrical energy. The electrons, ions and an oxidant react on the other side of the fuel cell to complete the electrochemical reaction and form the products. Table 1.1 lists the major types of fuel cells with their electrolyte materials, operating temperatures, commonly used fuels and application areas.

1.1. Polymer electrolyte membrane fuel cells (PEFC)

Table 1.1: Major types of fuel cells with their properties and application areas

Fuel Cell Type	Electrolyte	Operating Temperature (Range)	Commonly used fuel	Application areas
Alkaline fuel cell (AFC)	Potassium hydroxide (KOH)	60-220°C	Hydrogen	Transport (Space shuttles)
Low temperature polymer electrolyte membrane fuel cell (PEFC) or (LT-PEFC)	Proton conducting membrane (Nafion® based)	60-80°C	Hydrogen, Reformate	Transport, Stationary
High temperature polymer electrolyte fuel cell (HT-PEFC)	Proton conducting membrane (PBI based, doped with phosphoric acid)	140-200°C	Hydrogen, Reformate	Transport, Stationary
Direct methanol fuel cell (DMFC)	Proton conducting membrane (Nafion® based)	80-130°C	Methanol	Portable, Special applications
Phosphoric acid fuel cell (PAFC)	Concentrated phosphoric acid (H ₃ PO ₄)	160-200°C	Natural gas	Stationary
Molten carbonate fuel cell (MCFC)	Molten carbonate salt (Li ₂ CO ₃ , K ₂ CO ₃)	650°C	Natural gas, Biogas	Stationary
Solid oxide fuel cell (SOFC)	Metal oxide (Commonly Yttria-stabilized Zirconia (YSZ))	800-1000°C	Natural gas, Biogas	Stationary

1.1 Polymer electrolyte membrane fuel cells (PEFC)

Polymer electrolyte membrane fuel cells (PEFC) have received much attention recently due to their potential in mobile applications for the decarbonization of the transport sector [9–12]. A polymer based membrane is used as the electrolyte in these fuel cells. In the case of low temperature PEFC (LT-PEFC), this membrane is Nafion® based. For high temperature PEFC

(HT-PEFC), this membrane is usually polybenzimidazole (PBI) based and doped with phosphoric acid (PA).

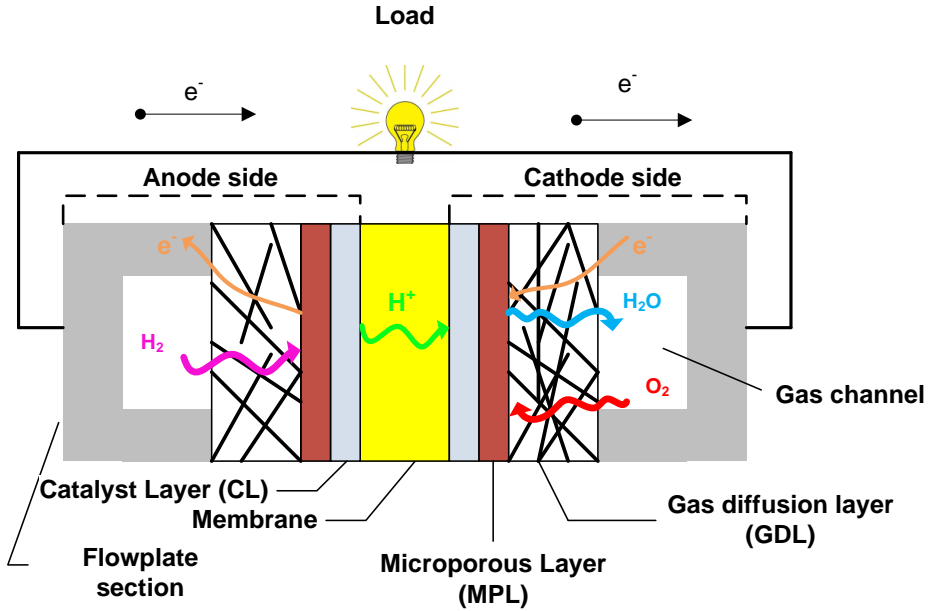


Figure 1.1: Working principle of a PEFC

Figure 1.1 presents a schematic of a PEFC and its working principle. Hydrogen is fed into the anode side whereas oxygen (or air) is fed into the cathode side. The hydrogen diffuses from the gas channel into a porous gas diffusion layer (GDL) and passes through another porous layer called the microporous layer (MPL) before reaching the catalyst layer (CL). The CL (also called the electrode) contains the platinum catalyst supported on carbon (Pt/C catalyst). The electrodes are often assembled with the GDL to produce the so called gas diffusion electrode (GDE). The combination of the membrane and the GDEs assembled together is called the membrane electrode assembly (MEA). The interface between carbon support, CL pores and the electrolyte membrane is called the triple phase boundary (TPB). When a platinum (Pt) particle is present in the vicinity, the electrochemical reaction can take place and separates the hydrogen molecules into ions and electrons. The anode side reaction is the hydrogen oxidation reaction (HOR) as shown in Eqn. (1.1);

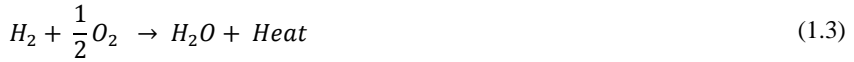


1.1. Polymer electrolyte membrane fuel cells (PEFC)

The oxygen on the cathode side also reaches the TPBs after passing through the GDE on the cathode side. The hydrogen ions produced on the anode side pass through the proton conducting membrane to the cathode side, whereas the electrons pass through an outer route through a load to the cathode side, thereby producing an electric current which can be utilized. The hydrogen ions, electrons and oxygen combine on the cathode side for the oxygen reduction reaction (ORR) and formation of water as follows;



The overall reaction of the PEFC is also called a Redox reaction and is given by Eqn. (1.3) below;



Thermodynamically, the heat or enthalpy change (ΔH) of the chemical reaction in the PEFC can be given as;

$$\Delta H = \Delta G + T\Delta S \quad (1.4)$$

Where,

ΔG = change in Gibbs free energy of the reaction (kJ mol^{-1})

T = reaction temperature (K)

ΔS = change in entropy of the reaction ($\text{kJ mol}^{-1} \text{K}^{-1}$)

The Gibbs free energy represents the maximum energy available for utilization as electrical energy in the fuel cell and therefore, the maximum theoretical efficiency (η_{\max}) of the fuel cell can be calculated as;

$$\eta_{\max} = \frac{\Delta G}{\Delta H} \quad (1.5)$$

The values of ΔG and ΔH for standard temperature and pressure (STP) conditions (1atm and 298K) for production of water in liquid or vapor state are different. The value of ΔH related to liquid water production is called the higher heating value (HHV) of hydrogen (286.02kJ mol^{-1}) and the value related to water vapor production is called the lower heating value (LHV) of hydrogen (241.98kJ mol^{-1}) [13]. The maximum theoretical efficiency of the PEFC when calculated with the HHV of hydrogen is about 83% and 94.5% when calculated using the LHV of hydrogen.

The theoretical fuel cell potential is given by;

$$E_0 = \frac{-\Delta G}{n \cdot F} \quad (1.6)$$

Where,

E_0 = Theoretical fuel cell potential (Volts)

n = number of electrons per molecule of $H_2 = 2$

F (Faraday's constant) = 96485 C mol^{-1}

So the theoretical fuel cell potential for hydrogen/oxygen fuel cell comes out to be 1.23V at STP. However, real fuel cell operation is seldom under STP conditions and the dependence of the Gibbs free energy on temperature and pressure is stipulated on the cell potential through the following form of the Nernst equation;

$$E = E_0 + \frac{RT}{nF} \cdot \ln \left(\frac{P_{H_2} P_{O_2}^{0.5}}{P_{H_2O}} \right) \quad (1.7)$$

Where,

E = Nernst fuel cell potential (Volts)

R (Universal gas constant) = $8.314 \text{ J mol}^{-1} \text{ K}^{-1}$

T = Operating temperature of the fuel cell (K)

P_{H_2} , P_{O_2} , P_{H_2O} = normalized partial pressures $\left(\frac{p_i}{p_0} \right)$ of hydrogen, oxygen and water vapor, where p_0 is atmospheric pressure

Eqn. (1.7) is valid for reactants and product water in gaseous state. For water produced in liquid state, $P_{H_2O} = 1$. The actual fuel cell potential is different from the Nernst potential due to characteristic losses encountered during fuel cell operation. These losses can be divided into three categories and the regions dominated by them can be readily identified in a polarization curve, which is a plot of the fuel cell voltage against the current density.

1.1. Polymer electrolyte membrane fuel cells (PEFC)

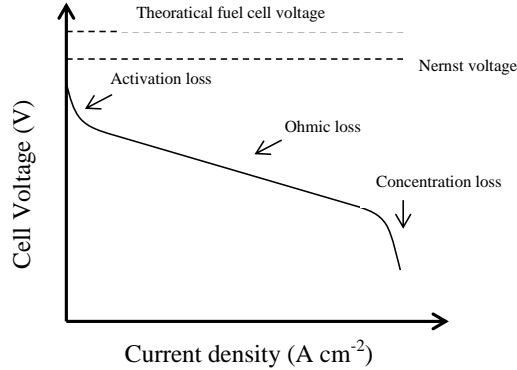


Figure 1.2: A typical polarization curve for a PEFC with regions of each dominant loss indicated

A typical polarization curve (UI curve) for the PEFC is shown in Figure 1.2. It is the standard way of evaluating the fuel cell performance and the three losses can be identified by the different slopes of the UI curve. The high losses encountered at low current density are related to the activation energy required for the electrochemical reaction and hence termed as activation losses (η_{act}). The losses encountered at intermediate current densities are related to the ohmic resistance of the cell. Since these losses follow the ohm's law, they are called ohmic losses (η_{ohm}). Finally, at very high current density, the slope of the UI curve increases dramatically again due to limitations to the transport of reactants to the reaction site (CL). These losses are called concentration losses (η_{conc}). The actual cell voltage (E_{cell}) can be calculated by the Eqn.(1.8) given below [14];

$$E_{cell} = E_{Nernst} - \eta_{act} - \eta_{ohm} - \eta_{conc} \quad (1.8)$$

Since the maximum theoretical potential of a fuel cell is fixed by thermodynamics, the fuel cell performance can only be improved by reducing the characteristic fuel cell losses.

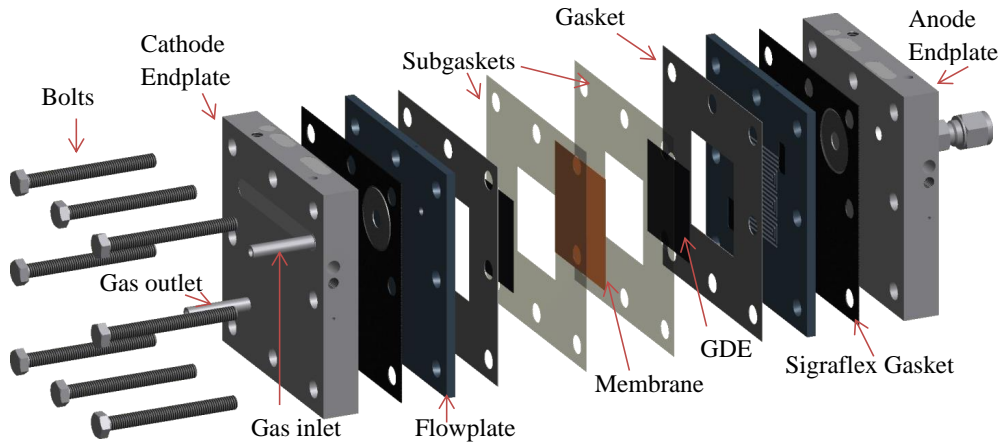


Figure 1.3: Exploded view of a PEFC single cell at IEK-3

The main components of a typical PEFC single cell construction at IEK-3 can be seen in Figure 1.3. The membrane is in the middle and is considered to be the heart of the fuel cell. It facilitates the electrochemical reaction as described above in detail. It also acts as a barrier to prevent the gasses passing through to the other side of the fuel cell besides providing the protonic conductivity for the hydrogen ions to flow through to the cathode side. The GDE is a porous layer (GDL) that also hosts the electrodes. It also provides an electric contact to the flowplates for the electrons. Also, product water can pass through the GDL into the gas channels for ultimate removal. GDLs based on carbon paper as well as carbon cloth are used in PEFC [15,16].

The gaskets and sub gaskets, usually made of polytetrafluoroethylene (PTFE) or perfluoroalkoxy (PFA) are used as hard stops for sealing of the MEA [17]. Selecting proper thicknesses of the hard stops also provides adequate compression of the MEA when the cell components are bolted together through the endplates [18]. The graphite based flowplates used on both sides contain the flow fields for the gases and also provide the electrical path for the electrons. In the case of a fuel cell stack (many single cells stacked together in series to generate higher power), they contain flow fields on both sides and hence are called bipolar plates. In the case of a single cell, however, only one side has the flow field and thus it is more accurate to call it a flowplate. The material of flowplates needs to be electrically conductive, chemically and thermally stable, mechanically tough and impermeable to gases [19]. Graphite based composites possess these properties and are usually used as flow/bipolar plate material. A modern alternative is to use metallic bipolar plates to reduce stack weight, but that presents challenges of its own such as corrosion and formation of a passivation layer reducing the electrical conductivity of the bipolar plate [20,21]. Sigraflex (a specialized graphite based conductive material from the SGL group) gaskets are used for sealing between the flowplates and the endplates on either side. The endplates used on both the anode and cathode sides of the single cell contain the inlets and outlets of the respective gases as well as bolting arrangements for screwing the cell together. They are usually made of stainless steel (SS)

1.1. Polymer electrolyte membrane fuel cells (PEFC)

and hold the fuel cell components together and provide mechanical stability to them. They are also used to accommodate heating elements for heating the cell as well as thermocouples for measuring the cell temperature during operation.

1.1.1 Comparison of LT-PEFC and HT-PEFC

The PEFC can be further classified into LT-PEFC and HT-PEFC with the main differences being the electrolyte membrane (Nafion[®] based for LT-PEFC while PBI based doped with PA for HT-PEFC) and the operating temperatures at atmospheric pressure as listed in Table 1.1. The proton conductivity of the Nafion[®] based membrane is highly dependent on the liquid water content of the membrane [22]. The fuel cell must be operated below the boiling point of water within a narrow window of operating temperature (about 60-80°C at 1 atm) due to a dramatic increase in voltage loss above 90°C [23]. These limitations necessitate LT-PEFC operation below this temperature and also the inlet gases must be humidified and complex water and heat management systems must be employed for constant water and heat removal for the proper functioning of the fuel cell [24–27]. The sluggish reaction kinetics of the ORR is also considered to be a major challenge for better PEFC operation and commercialization [28–31].

High temperature operation presents many advantages such as improved reaction kinetics, much higher tolerance to fuel impurities like carbon monoxide (CO), little need for humidification of inlet gases and much simpler heat and water management [32–35]. The HT-PEFC is designed for high temperature operation to harness some of these advantages by employing a PBI based membrane doped with phosphoric acid (PA) as the electrolyte. The protonic conductivity of this membrane does not depend on liquid water and is mainly provided by the PA, which can maintain good protonic conductivity upto 200°C [36]. The HT-PEFC can therefore be operated at temperatures from 140°C upto 200°C at atmospheric pressure and with dry gases [37]. Also, CO tolerance in the fuel stream of the HT-PEFC is 1 to 3% [38–44], which is much higher than the LT-PEFC, whose performance can be significantly affected by as little as 5-10 ppm of CO in the fuel stream [45]. This allows the use of a hydrogen rich gas (reformat) containing CO within the range tolerable by HT-PEFC, produced by reforming onboard fuels in heavy transport applications, as the fuel in HT-PEFC stacks for auxiliary power generation [46].

There are not many direct comparisons published in the literature between the performance of LT-PEFC and HT-PEFC at the single cell level. However, Zhu et al. [47] compared the performance of an LT-PEFC and HT-PEFC stack by electrochemical impedance spectroscopy (EIS) and determined that the ORR reaction kinetics of the HT-PEFC stack was much better. Authayanun et al. [48] compared HT-PEFC and LT-PEFC systems integrated with a glycerol steam reformer. They determined that the LT-PEFC system performed better under pure hydrogen operation and atmospheric pressure, but the HT-PEFC system performed better under high current density operation as well as pressurized and reformat operation. The HT-PEFC system with a water gas shift reactor also showed the highest system efficiency (60%) for the systems tested. Further comparative studies and investigation is required for a broader understanding of the effect of temperature on the rate of ORR at the single cell, stack and system

level. Also, a common testing and comparison protocol among various research groups and the industry would help standardize such investigations.

1.1.2 Challenges faced by the HT-PEFC and current research

A lot of research has been conducted recently in the field of HT-PEFCs due to their potential advantages as discussed in the previous section. The higher operating temperature also causes some serious challenges for the HT-PEFC. This includes much longer start-up times in comparison with LT-PEFC [49,50], which is critical for transport applications. The degradation rates of cell components are also much higher [32,35], with severe degradation expected for operation above 180°C [33]. Loss of PA due to PA leaching [51], uptake of the PA by the bipolar plates [18], dehydration and unfavorable redistribution of PA [52–54] in the MEA is also a main cause for lower performance and MEA degradation. Pt particle size growth due to agglomeration at elevated temperatures has also been reported as a major cause of performance degradation [55,56]. Pt dissolution also causes loss of electrochemical surface area (ECSA) at high temperature operation [57,58]. Severe corrosion of the carbon support of the Pt catalyst takes place at the cathode at high potential and high oxygen partial pressure [59,60]. This can cause a significant loss in ECSA and thus cause significant irreversible losses in the fuel cell performance [61,62]. Carbon corrosion can also effect the GDL material and cause loss of hydrophobicity [63] resulting in pore blockage and possible flooding of the GDL at higher current densities, thus reducing the operational window of the fuel cell. Thinning of the PBI membrane [64] and creep failure has also been reported in the literature as a major cause of membrane degradation [55,65–67]. The adsorption of phosphate anions onto the Pt surface is also an area of serious concern for HT-PEFC operation [68,69].

Most of the current research in the field of HT-PEFC is focused on resolving the issues faced by the HT-PEFC as described in the previous paragraph. At the component level, there has been a lot of research on membranes with higher protonic conductivity and more thermal, chemical and mechanical stability for increased longevity. Ozdemir et al. [70] achieved a protonic conductivity of 0.2 S cm^{-1} and improved thermal stability by dispersion of 5 wt. % ZrP nanoparticles in the PBI polymer before doping with phosphoric acid to obtain a high phosphoric acid doping level (PADL). The GDE is also a vital component of the MEA with several important functions as described previously. Mazur et al. [71] optimized the preparation procedure and chemical composition of the GDE for HT-PEFC and found spraying and brushing to be the most effective methods for CL deposition. They also tested PTFE and PBI as binder materials and found similar performance of the GDEs prepared by the spraying method with each binder. Lowering the Pt loading of the CL of the HT-PEFC is of utmost importance from a cost viewpoint. Martin et al. [72] achieved a stable performance of a HT-PEFC for over 1700 hours with a Pt loading of 0.1 mg cm^{-2} by using no binder material to prepare the CL. Zamora et al. [73] demonstrated improved electrochemical stability of the MPL by using carbon nanostructures (CNS) based MPLs and comparing it to carbon black (CB) based MPLs.

1.1. Polymer electrolyte membrane fuel cells (PEFC)

Studying the effects of various operating conditions on fuel cell performance is vital for determining the best operational window. Yan et al. [74] compared the steady state and dynamic performance of a LT-PEFC single cell under widely varying operating conditions. They tested the cell performance with different feed gas humidity and stoichiometry, operating temperature, operating pressure and fuel cell size. They used polarization curves and EIS to analyze and compare the cell performance at different operating conditions and determined the optimum level for each operating condition. Zhang et al. [75] compared the steady state and dynamic behavior of a HT-PEFC by comparing cell performance in flow-through mode and dead end mode. Rastedt et al. [76] investigated the effect of contact pressure cycling between 0.2 and 1.5MPa on single cell performance with a non-woven GDL. They determined a correlation between the loss of internal resistance and hydrogen crossover current and the emergence of small cracks and fiber intrusions in the GDL. Andreasen et al. [77] analyzed the performance of a single cell with varying CO, CO₂ and H₂ content in the anode gas by utilizing EIS. They measured impedance at different operating temperatures and currents in addition to the anode gas composition and found undesirable transient effects for measurements conducted at low temperatures and high CO content in the anode gas. Taccani et al. [78] investigated the effects of different flow field geometries on single cell performance and found that using a serpentine flow field results in better performance than a parallel flow field but also causes higher pressure drop. Finally, Korsgaard et al [79] developed a semi empirical model for fuel cell voltage versus current density, cathode stoichiometry and operating temperature by using linear regression and found excellent agreement with the experimental values.

Determination of the electrochemical parameters representing the electrode performance is a very useful way of understanding the causes of lower fuel cell performance. Mitigation strategies can then be developed for the isolated causes. EIS has been used successfully by many researchers around the world not only for this purpose, but also to identify and isolate different electrochemical processes within the cell, although the models used for fitting EIS data and the interpretation of the results differ considerably. Numerical, analytical and equivalent circuit models (ECM) have been used in the literature for fitting EIS data. Springer et al. [80] applied EIS to differentiate between the three different types of PEFC losses in the low and high frequency loops present in typical impedance spectra. Makharia et al. [81] applied the transmission line model to extract the ohmic resistance, catalytic layer electrolyte resistance and the double layer capacitance by fitting EIS data of a PEFC. Yi et al. [82] presented a numerical model based analysis of EIS data of PEFC to determine the charge transfer resistance, protonic resistance and the double layer capacitance along the thickness of the CL. Kulikovsky [83] presented an exact solution based analytical model for PEFC cathode impedance at low current densities and high cathode stoichiometry. EIS continues to be an intense area of research due to its powerful in situ characterization potential for PEFC, but interpretation of EIS data with simple and reliable fitting models for extraction of physically relevant fuel cell electrochemical parameters remains disputed.

Degradation of HT-PEFC is a very important issue since the higher operating temperature causes faster degradation of cell components. Modestov et al. [55] determined Pt particle growth as the main cause of degradation in a 780 hour life test of a HT-PEFC with more than double increase in the average Pt particle size. Galbiati et al. [84] determined that increased gas crossover and short circuit currents were the main causes of performance loss for the HT-PEFC in a 600 hour parametric test. Sondergaard et al. [85] found a correlation between the operating temperature and the accumulated gas-flow volume through the HT-PEFC and loss of PA by evaporation. They determined the loss of PA as the major degradation mechanism. Ossiander et al. [86] examined the effect of molecular weight and different reinforcement strategies for PBI based membranes and achieved significant reduction in degradation by enhancing the interactions between PBI polymer chains by cross-linking. Tang et al. [87] used a single and dual cell configuration to measure cathode potentials as high as twice the open circuit voltage in PEFC during startup and shutdown due to the air/fuel boundary developed at the anode. They determined the carbon corrosion at the cathode as the main degradation mechanism at high potentials. Eberhardt et al. [88] found the loss of PA to be only a function of gas flowrates and operating temperature. They suggested a PA management strategy to be employed for operating temperatures higher than 160°C at high current densities in HT-PEFC to achieve the 50,000 hour lifetime goal of the US department of energy for HT-PEFC. Accelerated degradation testing helps determine the main causes of degradation in a relatively small amount of time so that relevant mitigation strategies can be formulated to achieve lifetime goals for HT-PEFC set by the department of energy of United States. Reimer et al. [61] used load cycling to investigate four different HT-PEFC single cells. They used a simple polarization curve model to explore different possible degradation mechanisms. They concluded that loss of PA due to overall heat flux was a more likely interpretation under the operating conditions used than corrosion of the carbon based catalyst support due to high potential. De Beer et al. [63] used an accelerated acid leaching procedure to investigate degradation in HT-PEFC. Zhou et al. [89] used hydrogen starvation as the stressor to investigate HT-PEFC degradation. Park et al. [90] tested the mechanical stability of PBI based membranes under thermal cycling conditions and found that PBI composite membranes with pretreated PTFE had lower degradation rates than membranes with untreated PTFE. High temperature operation, start/stop cycling and potential cycling have also been applied as stressors to HT-PEFC for accelerated degradation testing.

1.2 Motivation and experimental goals

As discussed in the previous section, there are many areas of improvement for HT-PEFC operation. This thesis is mainly concerned with addressing some of the challenges faced by HT-PEFC as described above. The focus is at the MEA level and the experiments concentrate on identifying the effects of important operational and material parameters on the MEA performance in single cell operation. The underlying physical phenomena are identified and ideas for improvement are developed and tested. The overall goal of this study is to suggest ways to improve the long term single cell performance of the HT-PEFC by;

1.2. Motivation and experimental goals

- Identifying the effects of important operational parameters on the performance of the fuel cell and selecting the most suitable operating conditions for long term operation.
- Investigating the material parameters of the MEA and their interactions to compare the effect of different combinations of these parameters and suggest the best combinations.
- Minimizing the cell resistance by studying the effects of different operating conditions on characteristic electrochemical parameters related to the cathode catalyst layer (CCL) using EIS.
- Examining the effect of different stressors on fuel cell performance degradation and identifying the underlying degradation mechanisms for the development of mitigation strategies.

These four goals lead to the experimental studies presented in chapters 4, 5, 6 and 7. Chapter 4 addresses the issue of determination of the best operating conditions for fuel cell operation as well as development of statistical models to predict the cell performance with a small amount of experimental data available by utilizing the design of experiments (DoE). Chapter 5 is devoted to investigation of the effects of the most important material parameters on MEA performance and evaluation of their interactions and effects on cell impedance by the DoE and EIS methods. Chapter 6 covers the effects of gas composition on cell impedance and compares the different electrochemical parameters determined by the ECM and analytical models for analyzing EIS data. Finally, in chapter 7, a short accelerated degradation study is conducted to determine the effects of various stressors on cell performance and postulate some of the related degradation mechanisms and mitigation strategies.

2 Experimental Methods

This chapter presents the two most extensively used experimental methods in this thesis, the design of experiments (DoE) and electrochemical impedance spectroscopy (EIS) in detail.

2.1 Design of experiments (DoE)

2.1.1 One factor at a time (OFAT) method and DoE comparison

Fuel cell technology is a relatively complex field with electrochemistry, heat transfer, fluid mechanics and structural mechanics playing an important part among others in the overall cell performance. Also, as the search for cheaper and more efficient materials goes on, there are a large number of material and operating parameters which can affect the fuel cell performance. The traditional method used for investigating the effect of different variables on an output variable of interest has been the one factor at a time (OFAT) method. The procedure is to hold all variables constant except one, and then study the effect of varying this variable on the output variable. This method works well for a small number of variables. However, an increase in the number of variables to be analyzed requires a greater experimental effort, which is sometimes unrealistic. Another drawback of the OFAT method is the inability to determine interactions among the studied variables (different effect of varying a variable on the output variable, when another variable has a different value), which may be very important in some cases. Disregarding interactions may lead to incorrect interpretation of the obtained results. The DoE is a statistical approach to planning and analyzing scientific experiments, with many advantages. As most of the experimental characterization in fuel cell materials and operation usually involves a large number of variables, it is suggested as an alternative approach to the OFAT method. DoE has been around for quite a while now, especially in industrial quality control, where it is routinely a part of product and process improvement campaigns with a large number of variables. The DoE has the twofold advantage of not only reducing the experimental effort required for a large number of variables, but also yielding more reliable results in the cases where interactions are significant. The DoE method has enormous potential for application in the field of fuel cells and electrolyzers due to its versatility and suitability to the wide range of variables usually involved in typical characterization campaigns.

In DoE terminology, the independent variables, whose effect on the output is desired to be analyzed, are called factors. The dependent variable or the output, whose change with respect to the factors is to be analyzed, is called the response. Multiple responses can also be analyzed simultaneously. The effect of each factor on the response in isolation is called its main effect. The effect on two or more factors combined is called a factor interaction. Although, higher order factor interactions (involving 3 or more factors) exist for a DoE with k factors, usually the most important ones are the two factor interactions. Interactions involving more than two factors are

2.1. Design of experiments (DoE)

usually assigned to random noise and used as degrees of freedom for calculating the experimental error [91–93].

The so called 2^k design of the DoE refers to the case with k factors, each with 2 levels. These levels are usually carefully selected minimum and maximum values of interest of the factor, but they can also be qualitative attributes. The DoE can be either a full factorial or a fractional factorial depending on the number of experiments conducted. A full factorial design has the maximum number of experiments and also the maximum detail possible in the results, whereas a fractional factorial can be conducted with lesser number of experiments but the level of detail and accuracy is also reduced.

It is easy to verify that as the number of factors increases, the experimental effort required for the OFAT method increases many-fold. This renders planning and executing an effective experimental plan very tedious if not impossible when a large number of factors are involved.

A 2^k full factorial DoE requires 2^k experiments, whereas an OFAT with same detail and accuracy would require $(k+1)*2^{k-1}$ experiments [94]. Therefore, a full factorial DoE would reduce the experimental effort by a factor of $(k+1)/2$ in comparison to the OFAT as depicted in Figure 2.1.

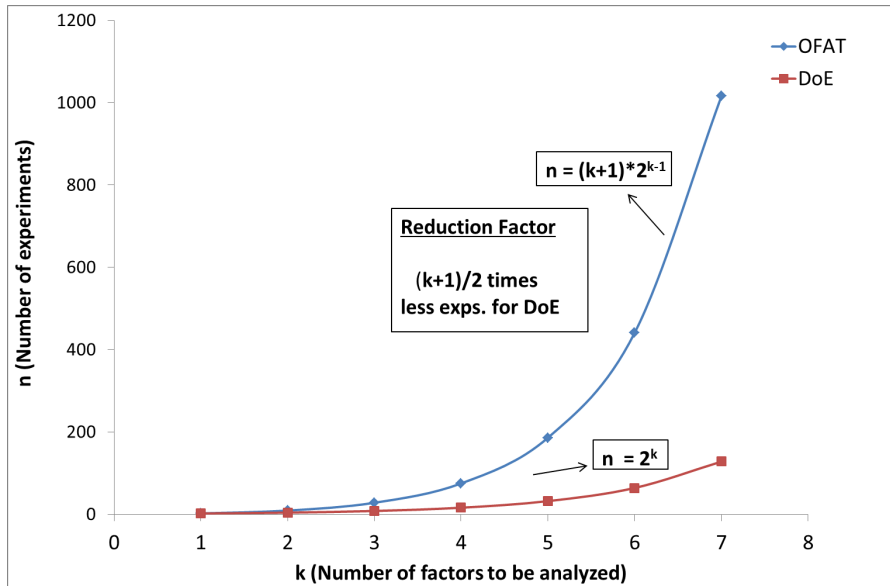


Figure 2.1: OFAT and DoE; comparison of experimental effort

When all the experiments required by a DoE design are performed, it is known as the full factorial design. When only a part of these experiments is performed, it is known as a fractional

factorial design. A fractional factorial design is preferred in the case of a large number of factors or expected linearity of the process under investigation [95].

It is evident from the above discussion that DoE should be the preferred method for dealing with a large number of variables. Nevertheless, it is still far from being the universally accepted methodology and there remains plenty of untapped potential for application of DoE in all areas of fuel cell research, mainly due to lack of knowledge and resistance to change, given its clear superiority over OFAT for experimental campaigns with a large number of factors. This is so, because, the DoE not only optimizes the experimental process itself by reducing the required number of experiments to a manageable minimum, but also improves the reliability and repeatability of the results by including the effects of factor interactions in the results alongside the main effects of the investigated factors.

2.1.2 DoE approaches and methodology

There are three main approaches to applying the DoE method to experimentation. These are the classical approach, the Taguchi approach and the Shainin systemTM. The classical approach was first developed and used by R.A. Fischer in 1920 [96] to an agricultural problem to produce the best crop of potatoes by analyzing many factors affecting the crop. The Taguchi approach was first published in Japan and gained popularity in the west after the 1980s. The Shainin systemTM is a legally protected system with little literature available. The Taguchi and Shainin approaches may be considered quality improvement strategies rather than just experimental designs [97] and their use in the industry for various purposes, especially quality control is increasing. The classical approach is especially suitable, valid and robust in the case of cheap experimentation or a small (less than five) number of factors or both [98]. Through the contributions of many scientists and authors, this remains to be true till this day with classical textbooks from Hunter et al. [91] and Montgomery [92] available for reference. All the three approaches to applying the DoE are superior to the OFAT methodology [98]. The response surface methodology (RSM) as developed by Box & Wilson [99], enhanced the classical approach by providing the ability to obtain results quickly and plan the experiments sequentially to improve new experimental designs on the basis of the results from the previous experiments [92]. The classical approach is followed in this thesis since the number of factors is small and experimental costs are also not prohibiting. Also, most of the literature and software available about DoE presume the classical approach.

2.1. Design of experiments (DoE)

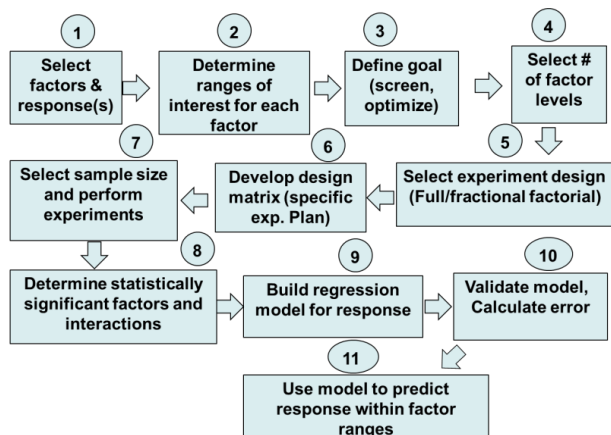


Figure 2.2: Typical steps for conducting a classical DoE procedure

Figure 2.2 shows the typical steps required for conducting a classical DoE procedure. After selecting the response and factors with their ranges of interest, the goal of the experiment is defined. It may be only to see the most important factors affecting a response (screen) or to find the factor settings to minimize or maximize the response (optimize). A 2 level DoE is most common, but a 3 level design can be selected when more details are required on the response behavior or non-linearity is expected in the response [100]. After selecting either full or fractional factorial design (full factorials are used in this thesis due to relatively low number of factors), the design matrix is constructed in its standard form as detailed in [91]. A sample size is selected and the experiments are then performed and the results are analyzed to construct and validate a regression model in steps 8 to 10. An example of a two level two factor full factorial DoE and its comparison with an equivalent OFAT plan is presented next.

The aim of a full factorial DoE is to develop a regression model for the response and factors by statistical analysis. This model is then valid within the selected ranges of each factor. The actual procedure of conducting a DoE is best explained with a simple example. Let us assume that a chemist wants to investigate the effects of pressure (P) and temperature (T) on the yield (Y) of a particular chemical reaction. He has selected the range of interest for pressure as 1 atm to 2 atm and for temperature as 100°C to 200°C. As there are two factors, using the OFAT methodology, he will have to conduct $(2+1)*2^{(2-1)} = 6$ experiments, whereas the 2^k full factorial DoE requires $2^2 = 4$ experiments. Table 2.1 and Table 2.2 show the OFAT and DoE experimental designs respectively.

Table 2.1: OFAT experimental design for two factors

Exp. #	P (atm)	T(°C)	Y(Grams)
1	1	100	?
2	1	150	?
3	1	200	?
4	2	100	?
5	2	150	?
6	2	200	?

Table 2.2: A 2 Level full factorial DoE for two factors

Exp. #	P (atm)	Factor level (P)	T(°C)	Factor Level (T)	Y(Grams)
1	1	-	100	-	?
2	2	+	100	-	?
3	1	-	200	+	?
4	2	+	200	+	?

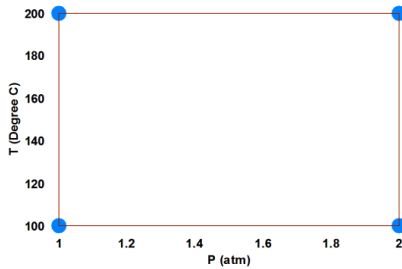


Figure 2.3: Design points for a 2 level 2 factor full factorial DoE

Figure 2.3 shows the design points for the DoE design in graphical form with the four experimental points shown as blue dots. In this case, the design points can be represented with a rectangle, but in the case of three factors, they will be the eight corners of a three dimensional cube. It should be noted that additional experiments are required in the OFAT method to “capture” the effects of the factors at “all corners” in the range of interest as visible in Table 2.1. This is not required in the DoE, as will be apparent, shortly. This is also the reason for the exponential increase in the required number of experiments in the OFAT method with increasing number of factors.

The formulation of the experimental campaign as given in Table 2.2 is called the “design matrix” in DoE terminology. It consists of each factor at its low (-) and high (+) value in successive

2.1. Design of experiments (DoE)

columns in a special order called the standard order. It is optional to add center points to the design matrix to check for the linearity of the response. The number of times the experiments in the design matrix are repeated or replicated is called the sample size and usually denoted by n . Increasing the sample size requires more experimental effort but provides higher accuracy by increasing the confidence interval of the constructed statistical model and vice versa [101]. Since the DoE is primarily a statistical method, a fine balance between sample size and model accuracy is very important.

Once the experiments are performed and results are available for the rightmost column (Y) of Table 2.2, the results are processed with a special algorithm called the Yates algorithm (detailed procedure can be found in [91]) to yield the required constant and coefficients for the regression model of the following form;

$$Y = a_0 + a_1P + a_2T + a_3PT + \varepsilon \quad (2.1)$$

Where a_0 is the constant term and a_1 , a_2 and a_3 are the coefficients of the pressure, temperature and their interaction respectively and ε is the experimental error. The term involving the factor interaction may be very important and cannot be determined using the OFAT approach. It captures the behavior of the response, when one factor is changed while holding another factor at different levels. For our example, this means that the chemist may observe that if he holds the pressure at 1atm and varies the temperature from 100°C to 200°C, this affects the yield not so much, but when he holds the pressure at 2atm and varies the temperature, this has a much larger effect on the yield of the reaction. The pressure and temperature are said to have a strong interaction in this case, quantified by the coefficient a_3 in Eqn.(2.1). In case of no or only a weak interaction between factors, the DoE and OFAT results are expected to be close, but the DoE achieves this result much more efficiently. In the presence of strong interactions, the OFAT results can actually be misleading [91]. The coefficients a_1 and a_2 are called the main effects of pressure and temperature in this case and quantify the sole effect of each factor on the response in the selected ranges.

Once the main effects and interactions are determined, the next step is to plot them on a normal probability plot to determine outliers. It is actually the outliers (which do not fall along the normal probability trend line) which are statistically significant, and must be included in the regression model. The normally distributed main effects and interactions are statistically insignificant and can be discarded from the regression model without significant effect on the response for a high sample size [102]. In our example, if the interaction of pressure and temperature was to be along the normal probability line and thus statistically insignificant, we would then simplify our regression model from Eqn. (2.1) as follows;

$$Y = a_0 + a_1P + a_2T \quad (2.2)$$

Eqn. (2.2) is the required regression model for the evaluation of the yield within the selected ranges of temperature and pressure. However, if the interaction is not normally distributed and thus statistically significant, then the regression model would contain the additional term of the interaction with its coefficient a_3 as given below in Eqn. (2.3);

$$Y = a_0 + a_1P + a_2T + a_3PT + \varepsilon \quad (2.3)$$

Figure 2.4 contrasts the scenarios where the two factor interaction is insignificant and significant respectively.

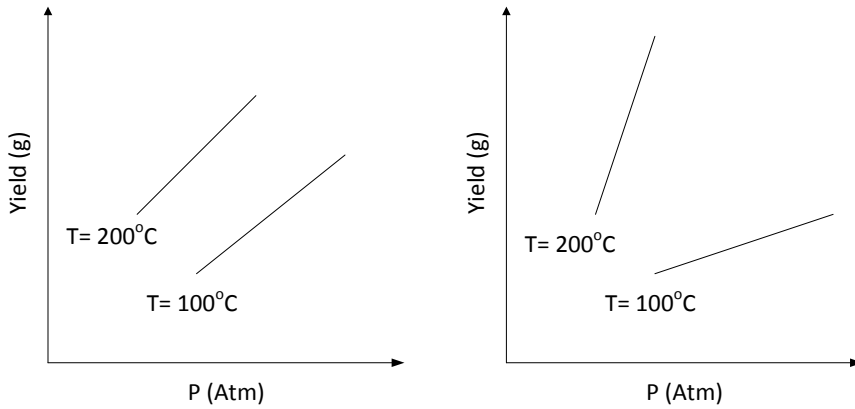


Figure 2.4: Comparison of an insignificant (left) and significant (right) interaction of pressure and temperature.

It should be noted that when a strong interaction is present between two factors, the lines connecting the two values of one variable at a particular level of the other are not parallel, whereas they are almost parallel in case of insignificant interaction.

Although it is possible to analyze the results using simple tools like Microsoft® Excel, for larger experimental campaigns performed with the DoE, it is recommended to use commercial software. This is especially useful for arranging and depicting the results readily in many useful forms typically used in DoE analysis. Some of the DoE analysis in this thesis was performed by utilizing the commercial software Statgraphics Centurion XVII version 17.1.12 (64 bit).

The DoE has been successfully utilized by many research groups in the area of fuel cells, however, given its capabilities, it still remains vastly underutilized. Wahdame et al. reviewed the application of DoE in various areas relevant to fuel cells [103]. Flick et al. applied the methodology for material properties and performance characterization for the PEFC [104]

2.2. Electrochemical impedance spectroscopy (EIS)

whereas Kahveci et al. applied response surface methodology to water and heat management investigations in PEFC [105]. Lohoff et al. applied the DoE methodology for the characterization of a DMFC stack [106] and finally, Barari et al. applied DoE to improve the temperature measurement accuracy in a SOFC [107]. The list is long, but this should suffice as evidence of the growing popularity of application of DoE in fuel cell research worldwide.

2.2 Electrochemical impedance spectroscopy (EIS)

Electrochemical impedance spectroscopy (EIS) is a powerful in-situ technique for the characterization of interfacial processes involving redox reactions at electrodes. EIS is a special electrochemical method as it presents the signal as a function of frequency at a constant voltage (or current) in contrast to classical electrochemical methods, which present current, voltage or charges as a function of time. This provides a potentially large amount of information about the behavior of the process under study at different frequencies, but special techniques and knowledge is required for the correct interpretation of this data and there exists significant difference of opinion in this regard. This is one of the reasons that EIS data is not always analyzed or interpreted in a similar fashion in the literature.

In the case of fuel cells it can be used to isolate and quantify the three main sources of voltage loss in fuel cells; the activation loss R_{act} , the ohmic loss R_{Ω} and the mass transport loss R_m , as well as the charge storing capacity of the electrode/electrolyte interface (termed as the double layer capacitance (C_{dl}) in most fuel cell literature). The physiochemical processes causing the losses have unique characteristic time constants due to the nature of the process and thus occur at different AC frequencies. Therefore, they can be easily identified in the impedance data and the information gained can then be used to minimize the losses and improve fuel cell performance.

2.2.1 EIS basics

Electrochemical systems are inherently non-linear systems. However, if a small enough voltage or current perturbation is applied, the response of the system is almost linear. This is called pseudo linearity. EIS measurements of electrochemical systems utilize the pseudo linearity of their response for very small AC voltage or current perturbations [108]. EIS measurements in fuel cells utilize a frequency response analyzer (FRA) to impose an AC signal (current or voltage) of very small amplitude on the fuel cell through a load. If a small current signal is applied, it is called a galvanostatic measurement and if the signal applied is voltage, it is termed as a potentiostatic measurement.

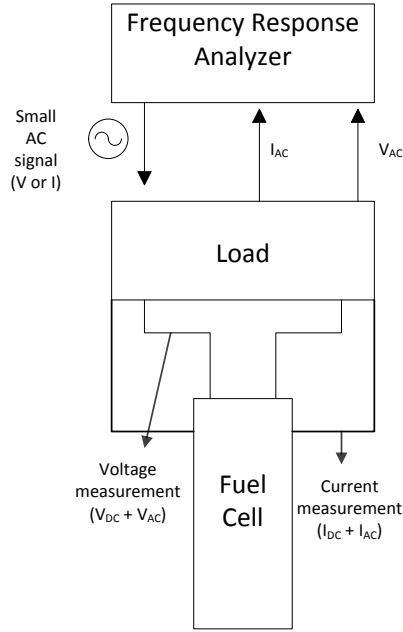





Figure 2.5: Measurement principle of fuel cell impedance

Figure 2.5 shows the schematic of the hardware and connections for an EIS measurement. The four terminal measurement technique is recommended for low impedance systems such as fuel cells to avoid large measurement errors [109]. These four terminals includes a counter electrode (CE), which provides current to the cell, a working electrode (WE), which measures the current through the cell and two reference electrodes for voltage measurement. The FRA analyzes the AC voltage and current response of the fuel cell to determine the resistive, inductive and capacitive behavior (the impedance) of the cell at that frequency. When conducted over a broad range of frequencies, EIS can provide a wealth of information about cell behavior with a single measurement.

Since the resistive, inductive and capacitive behavior of the cell at a particular frequency in response to a small AC perturbation signal determines the overall impedance of the cell [110], it is useful to list these basic electrical elements with their ideal impedances. Table 2.3 lists this information along with the symbols and voltage and current relationships for each element. As can be seen, the ideal impedance of the resistor is a real number, but the impedances of the inductor and capacitor are complex, therefore, the total impedance is represented by a complex number. The real part is called the real impedance ($\text{Re } Z$) and the imaginary part is called the imaginary impedance ($\text{Im } Z$).

2.2. Electrochemical impedance spectroscopy (EIS)

Table 2.3: Basic electrical elements with their voltage and current relation and ideal impedances

Electrical element	Symbol	Voltage current relationship	Impedance
Resistor (R)		$V = iR$	$Z = R$
Inductor (L)		$V = L di/dt$	$Z = j\omega L$
Capacitor (C)		$i = C dV/dt$	$Z = 1/j\omega C$

The series and parallel connections of the basic electrical elements follow the laws of electrical connections as shown in Figure 2.6. The total impedance is the sum of the impedances of elements connected in series, however, in the case of a parallel connection, the inverse of the total impedance equals the sum of the inverses of the impedances of the individual elements.

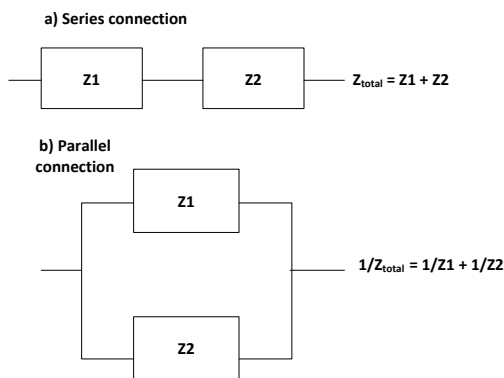


Figure 2.6: a) series connection of impedances b) parallel connection of impedances

EIS offers many advantages such as:

- Measurements possible for typical fuel cell operating conditions
- Measurements can be automated in many cases
- Measurements are non-intrusive and highly precise
- Many parameters can be determined from a single measurement

The main disadvantage of EIS is the ambiguity and complexity in the interpretation of the data.

There are two basic plot types used to represent EIS data. They are the Nyquist plot and the Bode plot. Examples of both of these plots are shown in Figure 2.7. The Nyquist plot presents impedance data as shown in Figure 2.7 a); the real part of impedance is plotted on the x-axis, while the negative of the imaginary part is plotted along positive y-axis. The impedance vector in

the complex plane makes an angle Φ (phase angle) with the x-axis and its magnitude $|Z|$ represents the absolute value of impedance. One obvious disadvantage of this representation is that frequency is not explicitly shown. The negative x direction is the direction of increasing frequency in a Nyquist plot.

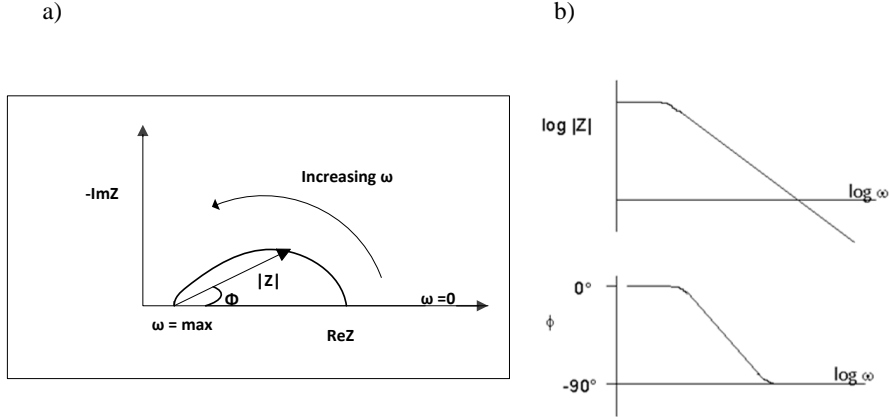


Figure 2.7: Representation of impedance data in the form of Nyquist (a) and Bode (b) plots

The Bode plot can show the impedance data in two different forms as depicted in Figure 2.7 b). The log of the magnitude of impedance can be plotted with the log of frequency on a log-log plot (top); or the phase angle (Φ) can be plotted against the log of frequency on a semi-log plot (bottom). Both forms of the Bode plot have the frequency as an explicit parameter.

2.2.2 Equivalent circuit models (ECM) for EIS data analysis

Since impedance measurements determine the resistive, capacitive and inductive behavior of the electrochemical system under study at a particular frequency, an equivalent circuit model (ECM) can be used to fit the impedance data. Physical processes do not always behave in ideal manner, but a resistor can model the bulk resistance pretty accurately. However, the charging of a double layer (electrolyte – electrode interface) can be better modeled by a constant phase element (CPE) rather than a pure capacitor as its distributed nature is a better representation of the inhomogeneous double layer interface [109]. It is common practice to use the CPE in ECMs for modelling the double layer in fuel cells [111]. The CPE is defined by a pre-factor Q representing capacitance and an exponent n and its impedance is defined as below in Eqn.(2.4) [112];

$$\frac{1}{Z_{CPE}} = Q \cdot (j\omega)^n \quad (2.4)$$

The CPE behaves as an ideal capacitor when the exponent n is 1.

2.2. Electrochemical impedance spectroscopy (EIS)

The capacitance of a CPE can be calculated by using the relation from Abouzari et al. [113] or M. Boudalia et al. [114]. The relation from Abouzari et al. is used in this thesis as shown below in Eqn.(2.5);

$$C = R^{\frac{1-n}{n}} \cdot Q^{\frac{1}{n}} \quad (2.5)$$

The value of R is taken from the resistance in parallel with the CPE (Figure 2.8). This equation is only valid if the product RQ or the value of the exponent n is close to unity [115].

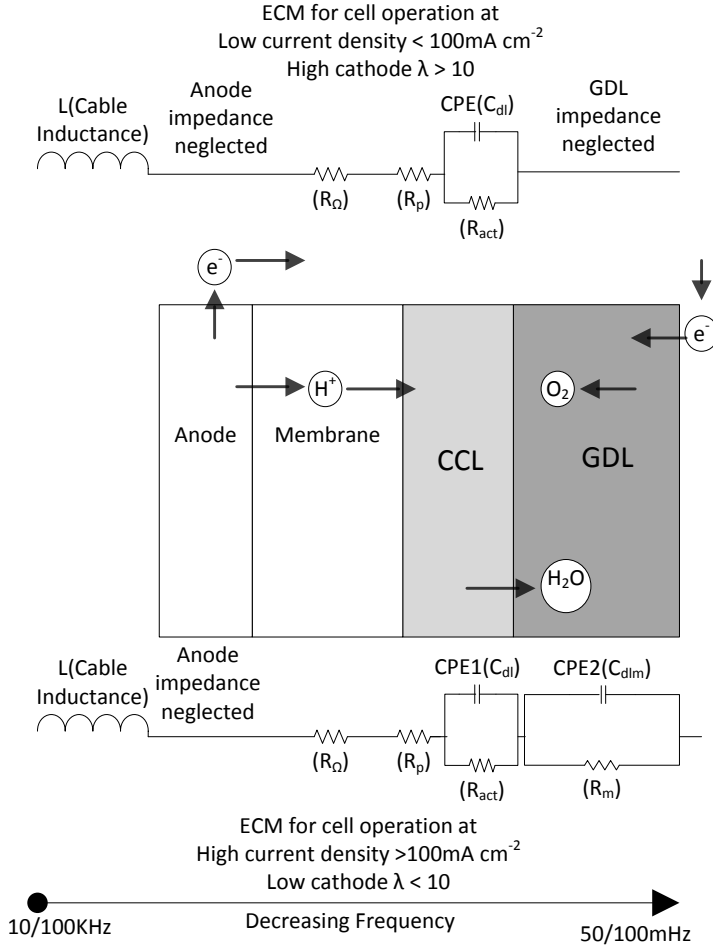


Figure 2.8: Schematic of EIS data analysis with ECM and the physical domains modelled in the low cathode λ , high current density (bottom) and the high cathode λ , low current density (top) regimes with pure H_2 on the anode side for both cases

Two different ECMs as shown in Figure 2.8 have been used in this thesis to fit the EIS data for extracting the electrochemical parameters of the fuel cell. Since pure hydrogen is used on the anode side, the anode impedance is neglected [116] in both cases. For high cathode λ and low current density, the model (top) is used with only one parallel R/CPE combination to model the double layer of the CCL, along with the ohmic resistance of the fuel cell (mainly membrane) (R_Ω) and the protonic resistance of the CCL (R_p). The resistance in the parallel R/CPE combination models the activation resistance (R_{act}) of the CCL and the CPE element models the double layer capacitance (C_{dl}) of the CCL. GDL mass transport losses are neglected in this case. The model (bottom) for low cathode λ and high current density uses an additional parallel R/CPE combination to model the mass transport resistance in the GDL (R_m) and the double layer property of mass transport $C_{dl,m}$ respectively. The frequency increases from right to left in the figure. Table 2.4 summarizes the electrical elements used in the two ECMs and the physical parameters they model.

Table 2.4: Elements used to fit the impedance data in the two ECMs with the physical parameters they are used to model

Element	Unit	Physical parameter modelled
L	H (Henry)	cable inductance
R_Ω	Ω (Ohm)	Ohmic resistance (mainly membrane resistance)
R_p	Ω (Ohm)	Protonic resistance of the CCL
R_{act}	Ω (Ohm)	Activation resistance (CCL)
CPE_1	F (Farad)	Double layer capacitance (C_{dl})
R_m	Ω (Ohm)	Mass transport resistance (GDL)
CPE_2	F (Farad)	Capacitance property related to mass transport

2.2.3 Analytical modeling for EIS data analysis

Physical modelling of fuel cell impedance can be divided into numerical and analytical modelling. Many numerical models for fuel cell impedance have been presented in the literature

2.2. Electrochemical impedance spectroscopy (EIS)

[82,117–120] . Using numerical models in least square fitting algorithms for fitting impedance data is theoretically possible, but it is a very time consuming process due to the need to solve complex differential equations multiple times numerically. Analytical equations for the CCL impedance have been derived for the case of fast oxygen transport in [81,121,122]. A simplified 1D analytical model of the CCL impedance has been suggested as a fast and reasonably accurate alternative to numerical models for sufficiently low current densities by Kulikovsky [83,123]. This model also allows calculating the oxygen diffusivity in the CCL which is a key CCL transport parameter not readily measurable. This model is described in more detail below and is used for fitting the low current density impedance of the in-house assembled MEA in this thesis for a comparison with the fitted electrochemical parameters by ECM modelling.

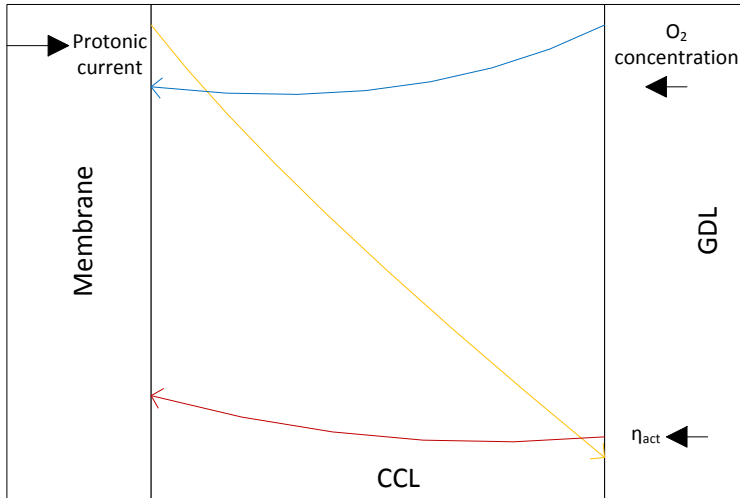


Figure 2.9: Schematic depicting the variations in the O₂ and protonic concentrations and the local activation loss in the CCL for high cathode λ and low current density operation redrawn from [123].

The model assumes small changes in oxygen concentration and local ORR overpotential (see Figure 2.9) within the CCL at low current densities (typically upto 100mA cm^{-2}) and high cathode stoichiometry ($\lambda > 10$). The model then solves the physical equations for characteristic cell parameters analytically, which can be obtained by fitting the impedance spectra by the Maple[®] worksheet provided in [83,123]. This is a fast analytical model for impedance data fitting which is valid for low current densities. It is interesting in the sense that it uses actual physical relationships for fitting rather than equivalent circuits, whose interpretation is still disputed among the EIS community [124,125].

The basic nomenclature followed by this 1D analytical model (called AM from here on for brevity) is as follows;

b = Tafel slope (V)

l_t = CCL thickness (cm)

σ_p = Protonic conductivity of the CCL ($\Omega^{-1} \text{ cm}^{-1}$)

j_0 = Current density (A cm^{-2})

F = Faraday's constant (C mol^{-1})

D_{oxp} = Diffusion constant of oxygen in the CCL ($\text{cm}^2 \text{ s}^{-1}$)

C_{ref} = Reference oxygen concentration (mol cm^{-3})

R_p = Protonic resistance of CCL ($\Omega \text{ cm}^2$)

R_{act} = Activation resistance of the CCL ($\Omega \text{ cm}^2$)

R_{oxp} = Oxygen transport resistance of the CCL ($\Omega \text{ cm}^2$)

C_{dl} = Volumetric double layer capacitance (F cm^{-3})

The values of j_0 , F , C_{ref} and l_t are known in our case (l_t is 0.012 cm for the in-house assembled MEA). The Maple[®] worksheet implementing the analytical model calculates the values of b , σ_p , C_{dl} and D_{oxp} analytically by fitting the impedance data. The characteristic fuel cell resistances are then calculated by using the Eqns. (2.6) to (2.8) below;

$$R_p = \frac{l_t}{3\sigma_p} \quad (2.6)$$

$$R_{\text{act}} = \frac{b}{j_0} \quad (2.7)$$

$$R_{\text{oxp}} = \frac{b l_t}{3(4FDC_{\text{ref}})} \quad (2.8)$$

The double layer capacitance is calculated according to Eqn. (2.9);

$$C_{\text{dl}} = \frac{1}{\omega_* R_{\text{act}}} \quad (2.9)$$

2.2. Electrochemical impedance spectroscopy (EIS)

Where ω_* is the angular frequency at the peak value of negative imaginary impedance (top of the semi arc in the Nyquist plot) in radians per second with the conversion from the regular frequency (f) in Hertz (Hz) is as in Eqn. (2.10);

$$\omega = 2\pi f \quad (2.10)$$

The impedance data needs to be entered into the Maple worksheet along with initial guesses for each of the parameters to be calculated. It is essential to use reasonable initial guesses otherwise the solution may not converge.

The AM does not explicitly calculate the ohmic resistance R_Ω , but it can be obtained from the left intercept of the Nyquist plot. The AM instead calculates the mass transport resistance of the CCL R_{oxp} (indirectly) based on the value of the diffusion coefficient of oxygen inside the CCL (D_{oxp}). This is a parameter not provided by the ECM. In fact, another parameter D_b , the diffusion coefficient of oxygen in the GDL can also be calculated by the AM for sufficiently thin CCLs (around 40 μm which is typical for LT-PEFC) but the actual used CCL in this thesis is much too thick (120 μm) therefore the value of D_b is not realistic and thus not used. These two parameters are of very high practical importance and methods for their accurate determination are scarce in the literature.

3 Experimental Setup and Procedures

This chapter describes the used test cells and their components and preparation, the test station, and EIS and CV measurement equipment and settings in detail.

3.1 Test cells

Two different types of test cells are used in the experiments for this work. They differ only in the maximum cell area available for electrochemical reaction. The hardware components have a similar design with minor differences and different sizes. The smaller test cell has a maximum area of 17.64cm^2 while the larger cell has a maximum area of 50cm^2 .

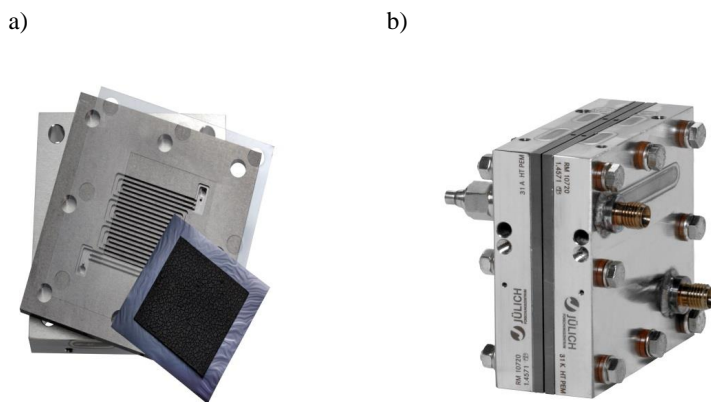


Figure 3.1: a) A stainless steel endplate, graphitic flowplate, PFA gasket and commercial MEA for the single cells b) In-house assembled single cell

Figure 3.1a) presents a graphite based flowplate and a stainless steel based endplate used for single cell construction. The flowplate for the smaller test cell (17.64cm^2) has a 3-fold serpentine flow field, whereas the flowplate for the larger test cell (50cm^2) has a 5-fold serpentine flow field. Figure 3.1b) shows an assembled single cell. The single cell is prepared by sandwiching a MEA (in-house or commercial) between PFA gaskets and placing it between the anode and cathode flowplates. This assembly is then bolted together between the two endplates.

3.1. Test cells

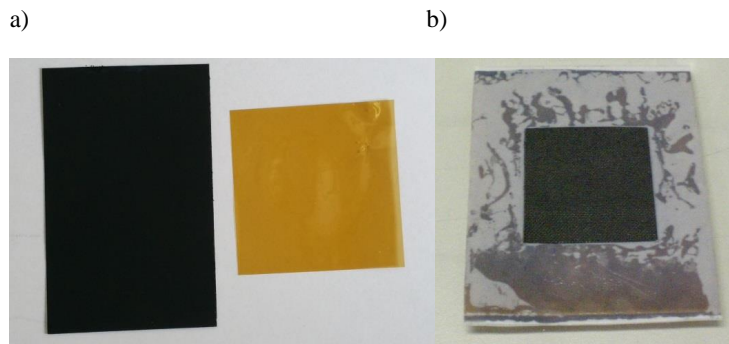


Figure 3.2: a) Left: Freudenberg H2315C2 GDL Right: PBI based membrane (AM-55) from FUMA-Tech, Germany b) An in-house assembled MEA with PFA gasket

An in-house assembled MEA is presented in Figure 3.2. The MEA is prepared by doping a PBI membrane with PA and pressing it between two gas diffusion electrodes (GDE). The membrane used in this study is PBI based (AM-55), purchased from FUMA-Tech, Germany. It is immersed in 85% PA solution for 12 hours at a temperature of 110°C to achieve a PADL of $15.5 \pm 0.5 \text{ mg cm}^{-2}$.

The GDEs are prepared by the doctor blade method. To produce the catalyst ink, Pt/C catalyst (Alfa Aesar) is mixed with the solvent (Propan-1-ol: Propan-2-ol (1:1)), deionized water and the PTFE binder and then the mixture is sonicated for 30 minutes. The catalyst ink is then coated onto a commercial non-woven GDL with microporous layer (MPL) (Freudenberg H2315C2). The GDE is then left overnight for drying. Each MEA is prepared just one day before its intended use to avoid loss of PA from the membrane.

PFA gaskets are used as hard stops between the MEA and the flowplates on both sides. The total thickness of the gaskets is calculated as 80-85% of the total MEA thickness to achieve 15-20% MEA compression which is suggested as the optimum compression by BASF. Sigraflex gaskets are used between the flow plates and the stainless steel endplates on both sides for sealing as well as maintaining good electric conductivity. The endplates are also used as the current collectors for the single cells.

The single cell is screwed together with eight bolts on the endplates. The torque applied on each bolt is usually 6Nm, but it is permissible to go upto 8Nm to prevent gas leakage in the cell. A torque higher than this value may cause permanent damage to the flowplates and the MEA. A leakage test is conducted with dry nitrogen after tightening the bolts on each single cell. A leakage of more than 40mbar per minute is not allowed on either of the anode or cathode sides to the environment or between the anode and cathode side (across the membrane). This value translates to $10^{-3} \text{ mbar l s}^{-1}$ if the total volume of the system including the pressure testing device is taken into account. If this is the case, the cell is disassembled and all the components, especially the MEA and gaskets are examined again and replaced if necessary. The cell

preparation procedure is standardized in this way to minimize the variance in cell assembly due to change of personnel.

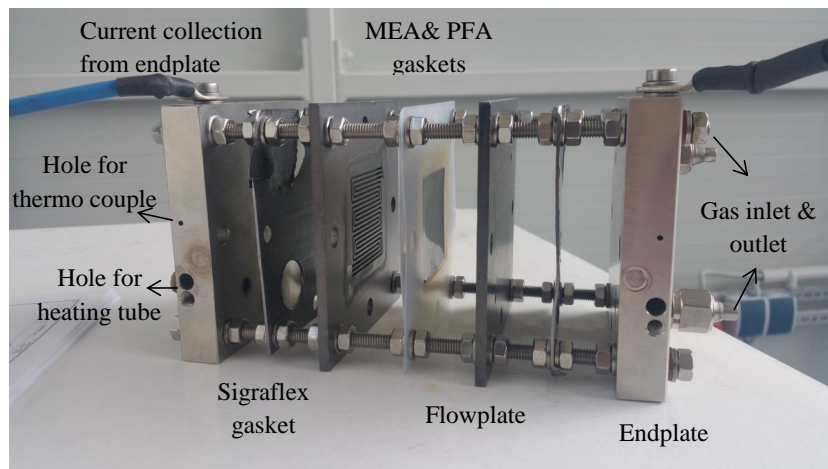


Figure 3.3: Exploded view of a single cell at IEK-3

An “exploded” single cell is presented in Figure 3.3. It can be seen that the current collecting cables are directly connected to the endplates on both the anode and cathode sides. Also, there is no separate heat removal system for the single cell. The endplates are also used to dissipate the heat produced during cell operation by heat convection to the environment.

The heating of the cell is done through heating tubes inserted in the endplates. Also, the gas inlets and outlets are available in each endplate. The endplates also have special holes for temperature measurement as shown in Figure 3.3. Voltage measurement is done through special holes in the flowplates.

Once the cell is correctly assembled and the gas leakage is below the specified limit, it is installed in the test station and a standardized break-in procedure is run on the cell. This procedure is necessary before any testing for optimized cell operation as the PA redistributes from the membrane into the CLs and the PA in the membrane reaches its equilibrium concentration [18]. The break-in procedure is described in detail in the next section.

3.1.1 Break-in procedure and BOL and EOL data acquisition

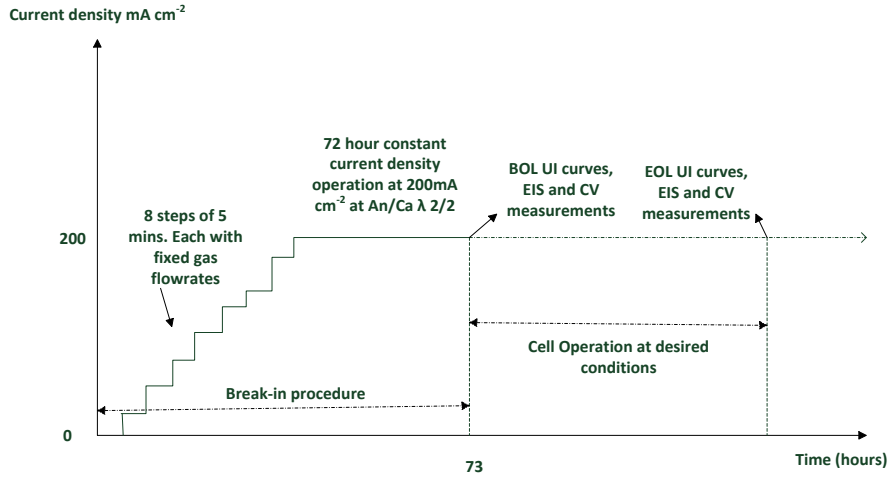


Figure 3.4: Break-in procedure and typical testing of a single cell

Once the leakage of the cell is below the specified limit, it is installed into the test station and a break-in procedure is run on the cell before any testing. Figure 3.4 shows the details of the break-in procedure and later testing of a single cell. The break-in procedure consists of initially heating the cell above 100°C without gas flow on either side. After the temperature is higher than 100°C, flow of the gases is started on both the anode and cathode sides. The anode is fed with dry hydrogen and the cathode is fed with dry air. The flowrates of the gases are kept constant for an anode/cathode stoichiometry of 2/2 at a current density of 200mA cm⁻². After 20 minutes, the load is applied to the cell and eight steps of five minutes each are used to reach the current density of 200mA cm⁻².

When the cell reaches a current density of 200mA cm⁻², it is operated at this current density for 72 hours continuously. This completes the break-in procedure. Beginning of life (BOL) UI curves, EIS and CV measurements are performed immediately after the break-in procedure finishes. Then the cell is operated on the desired operating conditions as planned. The end of life (EOL) testing is performed before disassembling the cell for EOL data acquisition and comparison with BOL.

3.1.2 UI curve

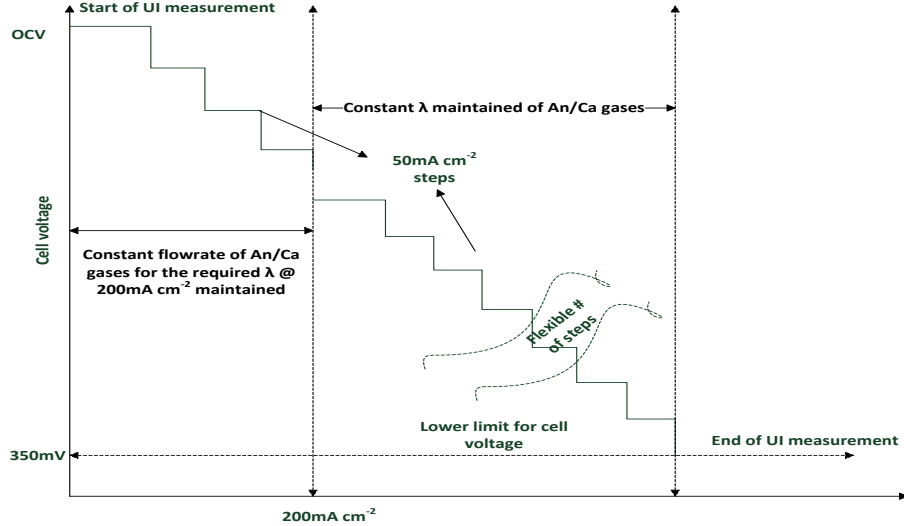


Figure 3.5: UI curve procedure for a single cell

A UI curve is obtained as shown in Figure 3.5. Firstly, the load is set to 0A cm^{-2} so that the cell is at the open circuit voltage. The gas flowrates are fixed below the current density of 200mA cm^{-2} to the values of the required anode/cathode λ at this current density. The current density is increased in steps of 50mA cm^{-2} in time steps of 1 minute and the corresponding cell voltages are saved. This process is automatically stopped if the cell voltage falls below a value of 350mV. Sometimes, the steps used below 200mA cm^{-2} are 10mA cm^{-2} instead of 50mA cm^{-2} to have more data points in the activation region (for low current density and high cathode λ measurements of EIS) for comparison with EIS data. The procedures for break-in and UI curves are automated with prewritten Microsoft Excel sheets loaded into the LabVIEW program of the test station.

3.2 Test station



Figure 3.6: The test station for single cell testing

The test rig used for most of the single cell testing is shown in Figure 3.6. It is equipped with supply of hydrogen or reformat on the anode side and oxygen or air on the cathode side. In addition to this, there is a nitrogen connection to both sides of the cell to spray the cell with nitrogen in the case of an unexpected shutdown during automated operation. The attached computer runs the LabVIEW program which can be used to operate the cell remotely for long time periods. A Microsoft excel sheet can be loaded into the computer with predefined operating conditions and duration of cell operation. This makes it possible to automate cell operation and collect continuous data without interruption. A maximum of four single cells can be operated simultaneously at the test station. A simplified flow diagram of the test station is presented in Figure 3.7.

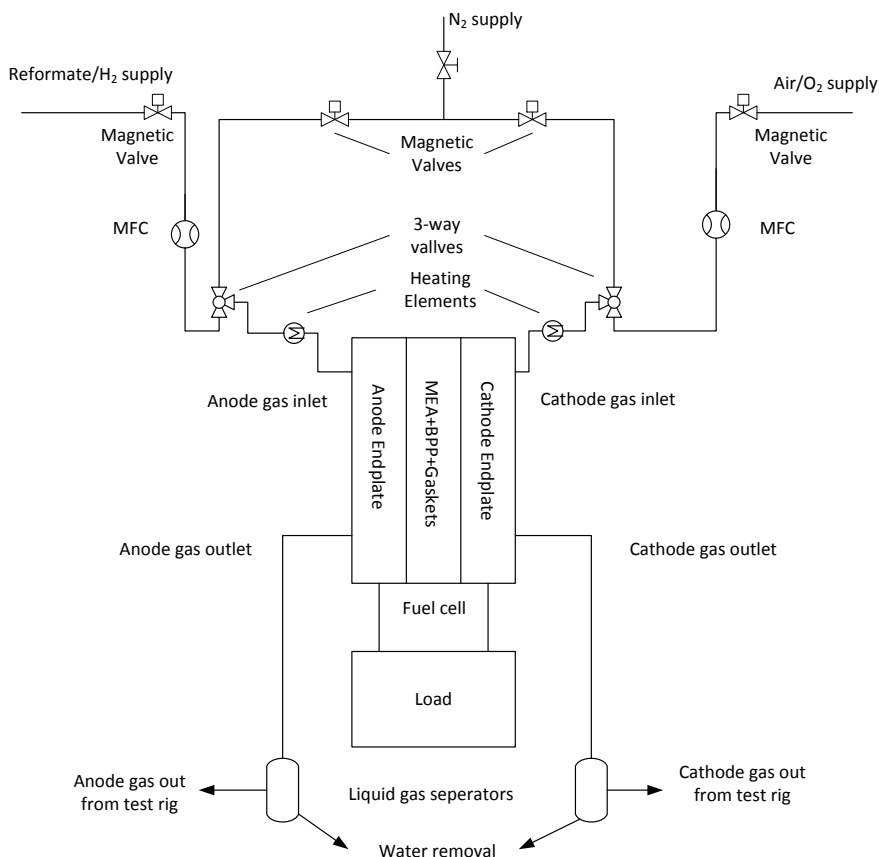


Figure 3.7: Simplified flow diagram of the single cell test station used for the experiments

A single cell installed in the test rig with gas inlets and outlets and voltage and current measurement cables and heating arrangements for the cell are shown in Figure 3.8. Both of the available cell types at the IEK-3 were utilized in this study, sometimes depending on the size of the available MEA. The results are always normalized with the cell area for a reliable comparison in case of different cell areas for two MEAs.

3.2. Test station

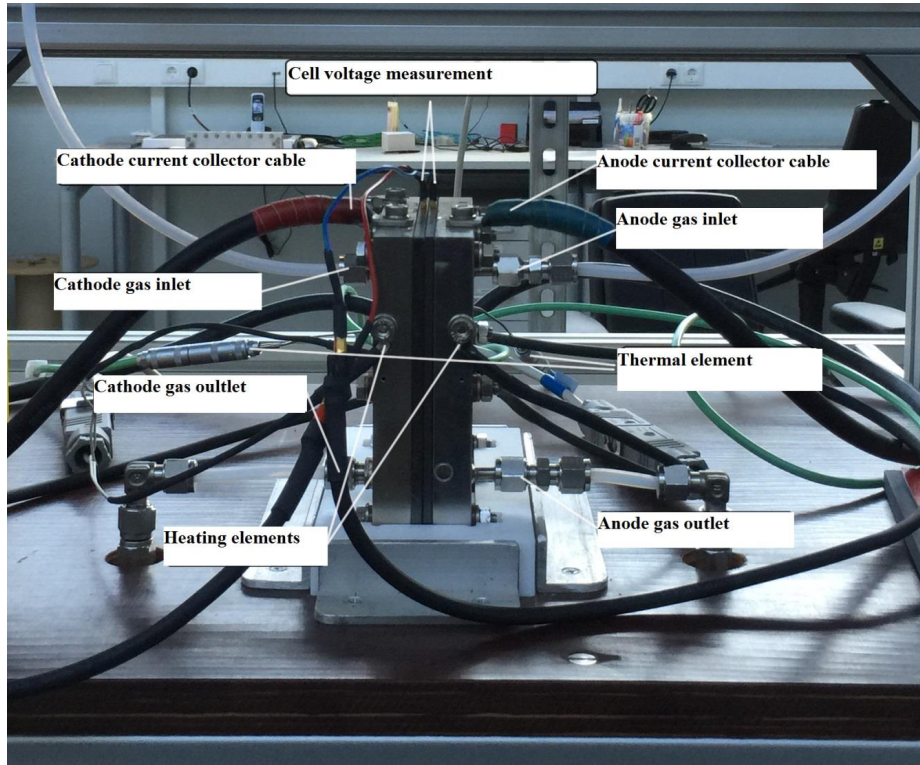


Figure 3.8: Single cell installed in the test station for testing, co-flow configuration

The measurement equipment along with their ranges and accuracies of different important physical values of the test cell in the test station are presented in Table 3.1.

Table 3.1: Measurement equipment and their range and accuracy (Source: Test station manual)

Physical value	Measuring equipment	Measurement range	Accuracy	Resolution
Cell current in Amperes and Cell voltage in Volts	H&H Last ZS Electronic Load (Model ZS506-4NV) [Höcherl & Hackl GmbH: S. 23 ff.]	0 – 60A 0 – 60V Max. 500W	0.2 % of the set value \pm 15mA 0.2% of the set value \pm 15mV	0.01A 0.01V
Volume flowrate of the reactant gases in Nml/min	Bronkhorst EL-Flow® [Bronkhorst High Tech B.V.]	0.16Nml/min to 6Nl/min (cathode) 0.16Nml/min to 3Nl/min (Anode)	\pm 0.5 % of measured value plus \pm 0.1 % of set value	\pm 0.1 % V of the set value

Temperature of the endplates in Degree C	Keithley Thermocouple Type K [Keithley Instruments Inc. 2003: S. 1]	-20 to 1372°C	1.26°C	0.001°C
--	---	---------------	--------	---------

3.3 EIS and CV measurement equipment and settings

The EIS and CV measurements are performed by a Zahner Zennium electrochemical workstation by ZAHNER-Elektrik GmbH & Co. KG with an additional PP series power potentiostat PP241 for high current measurements. These potentiostats are designed to apply and sink high currents upto ± 40 A at a total power dissipation upto 200W. Both devices can be operated in galvanostatic and potentiostatic modes. Table 3.2 presents some relevant specifications of the Zennium workstation while Table 3.3 presents those of the PP241 power potentiostat.

Table 3.2: Important specifications of the Zahner Zennium workstation used for EIS measurements (Source: Zahner product catalog)

Characteristic	Value	Accuracy
Frequency range	10 μ Hz to 4Mhz	<0.0025%
Output current range	± 100 nA to ± 2.5 A	$\pm 1\%$ of set value
Maximum voltage	± 4 V	$\pm 250\mu$ V (0.025%)

Table 3.3: Important specifications of the PP241 power potentiostat used for EIS measurements (Source: Zahner product catalog)

Characteristic	Value	Accuracy
Potential range	± 5 V	$\pm 0.1\%$ / ± 1 mV
Current range	0A to ± 40 A	$\pm 0.25\%$ / ± 1 mA
Output power	200W	--
Frequency range	10 μ Hz - 200kHz	--
Impedance range	1 $\mu\Omega$ - 1k Ω	--

The EIS and CV data obtained can be analyzed by the pre-installed Thales Z software package on the PC connected to the Zahner Zennium electrochemical workstation. Standardized procedures are used for in-house EIS and CV measurements too as described below.

3.3.1 EIS measurements

EIS is used to obtain impedance measurements for different cells at different operating conditions. The setup for the EIS measurements consists of a conventional two-electrode setup with the anode serving as a quasi-reference and counter electrode and the cathode serving as the working electrode. A frequency range of $10^{-1} - 10^5$ Hz and AC signal voltage amplitude of ± 10 mV is usually chosen in this study; however a minimum frequency of 50 mHz is also chosen at times when higher resolution is required at the low frequency end of the impedance spectrum. Other important parameters which must be selected include measurement points to be recorded per decade of frequency (steps per decade) and measure periods for each EIS measurement. For each of these parameters, two values must be given, one below 66 Hz and the other above this frequency. This enables optimization of resolution over measuring time and accuracy over measuring time since measuring time is dominant below the frequency of 66 Hz. In this thesis, four measure points per decade are used below 66 Hz for both of these parameters and ten measure points per decade are used above 66 Hz. Also, four measure periods are selected below 66 Hz and ten measure periods above 66 Hz. These settings are used for all the measurements unless otherwise stated. This helps achieve better reproducibility and comparable results as well as optimization of the measuring time for each EIS measurement while maintaining reasonable accuracy. Care is taken to measure impedance at stationary conditions for reliable measurements. The fuel cell is first run on the required conditions for at least five minutes and then the impedance measurement is started. The cables connecting the Zennium workstation to the cell are twisted together properly to minimize cable inductance and noise. Each measurement is repeated at least once for comparison of the reproducibility and backup of the impedance spectra.

3.3.2 CV measurements

The Zahner Zennium electrochemical workstation is also used for the CV measurements. The CV measurements are done in potentiostatic mode. In order to perform the measurement, the fuel cell is fed with dry hydrogen (70 Nml min^{-1}) and dry nitrogen (100 Nml min^{-1}) at the anode and cathode sides respectively. The anode works as pseudo-reference and counter electrode, while the cathode is the working electrode. The potential of the working electrode is scanned between 0.05 V and 1.2 V with a scan rate of 50 mV s^{-1} and four cycles are performed. The CV data is analyzed using the Thales Z CV software. The cathode catalyst active area is estimated considering the positive current density peak related to hydrogen desorption for the last cycle.

The estimation is done according to Eqn. (3.1) assuming that the cathode catalyst (Pt loading $\cong 1\text{mg cm}^{-2}$) is covered by a monolayer of hydrogen with a charge density of $210\mu\text{C m}^{-2}$ as suggested by Liang et al. [126];

$$ECSA(m^2 g^{-1} Pt) = \frac{Q(C\text{ cm}^{-2})}{\{210 \times 10^4 (\mu\text{C m}^{-2} Pt) \times Pt\text{ loading } (mg\text{ cm}^{-2})\}} \quad (3.1)$$

3.3. EIS and CV measurement equipment and settings

4 Commercial MEA Characterization

This chapter is devoted to the characterization of the commercially available HT-PEFC MEAs at IEK-3. It is imperative to characterize the MEAs for performance with similar operating conditions not only to be able to judge them from a performance viewpoint, but also to investigate the effect of important operating conditions on the performance of each MEA.

4.1 HT-PEFC MEA characterization with DoE

The commercially available HT-PEFC MEAs at IEK-3 are listed in Table 4.1 below.

Table 4.1: Commercial HT-PEFC MEA information

Serial #	MEA Name	Code	Active area (cm ²)	Manufacturer	Date of Purchase
1	Celtec [®] P1100W	A	45	BASF	Oct 2013
2	Advent TPS [®]	B	50	Advent Technologies [®]	Jan 2014
3	Elcomax	C	50	Elcomax	March 2012
4	Dapozol 100	D	46.2	Danish power systems [®]	Jan 2014

The Celtec[®] PW1100 MEA from BASF is a PBI based membrane doped with PA using a proprietary membrane doping method with the sol-gel technique. This method can increase the PA content in the membrane by a factor of 3 or more in comparison to other doping methods [36]. The GDL material is woven carbon cloth. The Advent TPS[®] MEA is based on pyridine type structures incorporated around a stable polymer backbone [127]. A carbon cloth material is used as GDL. Dapozol 100 MEAs are PBI based membranes with carbon paper based GDL materials [128]. The Elcomax MEA also has a PBI based membrane with a carbon paper based GDL.

The standard 50cm² cell at IEK-3 (as described in section 3.1) is used for operating all the MEAs in this chapter. The standard break-in procedure is run prior to any testing. Dry gases are used with hydrogen on the anode side and air on the cathode side for actual cell testing.

The DoE is used to characterize all four MEAs. The four most important operating parameters affecting cell performance as listed in Table 4.2 are considered as factors with two levels. The cell voltage (V) is considered as the only response variable. A two level four factor (2⁴) full factorial design is used for this purpose with the aim of extracting maximum information for

4.1. HT-PEFC MEA characterization with DoE

developing reasonably accurate statistical regression models [129]. The ranges for the factors are selected by keeping realistic fuel cell operation in mind.

Table 4.2: List of factors and their investigated levels

Serial #	Factor	Symbol	Code	Low level (-1)	High level (+1)	Mean (0)
1	Anode stoichiometry	λ_a	A	1.2	3	2.1
2	Cathode stoichiometry	λ_c	C	2	4	3
3	Current density	i (A cm ⁻²)	I	0.2	0.6	0.4
4	Operating temperature	T (°C)	T	140	180	160

A 2⁴ DoE requires a total of (2⁴) sixteen experiments for each MEA to obtain one replication (run) excluding any middle points. It is decided to introduce middle points systematically into the experiments to cater for any non-linearity in the response [93] (in which case a 3⁴ DoE maybe required for more accurate results) as well as cell degradation. One middle point is decided at the beginning, and then one after every four data points. This translates into a total of five middle points for each run. The design matrix for the 2⁴ DoE with middle points is given in Table 4.3. The actual experimental order is randomized to avoid systematic influences to the response variable [100].

Table 4.3: Design matrix for a 2 level four factor (2⁴) DoE with middle points

Serial #	Treatment combination	A	C	I (A cm ⁻²)	T (°C)
1(M)	Middle	2.1	3	0.4	160
1	(1)	1.2	2	0.2	140
2	A	3	2	0.2	140
3	C	1.2	4	0.2	140
4	AC	3	4	0.2	140
2(M)	Middle	2.1	3	0.4	160
5	I	1.2	2	0.6	140
6	AI	3	2	0.6	140
7	CI	1.2	4	0.6	140
8	ACI	3	4	0.6	140
3(M)	Middle	2.1	3	0.4	160
9	T	1.2	2	0.2	180
10	AT	3	2	0.2	180
11	CT	1.2	4	0.2	180
12	ACT	3	4	0.2	180
4(M)	Middle	2.1	3	0.4	160

13	IT	1.2	2	0.6	180
14	AIT	3	2	0.6	180
15	CIT	1.2	4	0.6	180
16	ACIT	3	4	0.6	180
5(M)	Middle	2.1	3	0.4	160

It is decided to use two sample sizes for the whole campaign. One small sample size ($n=5$) and a large sample size ($n=30$). A large sample size is normally recommended for achieving a confidence interval higher than 95% [101]. As described earlier, one run takes 21 experimental readings (including middle points) with varying operating conditions. The required number of experiments rises dramatically with sample size. It is intended to compare the results of the two sample sizes to evaluate the possibility to reduce the sample size without compromising too much on accuracy. This can result in significant savings in time, money and effort while maintaining reasonable accuracy.

4.1.1 Detailed calculation procedure for MEA D

As a comparison is planned between a low sample size ($n=5$) and a high sample size ($n=30$) to estimate the effect of sample size on the regression model, this translates to a minimum of 30 runs and thus ($21 * 30 = 630$) experimental values of the cell voltage per MEA. This task is automated via an excel program loaded in the LabVIEW program at the test station to run the cell continuously under desired conditions and retrieve the corresponding results. Table 4.4 depicts the calculation of the average response variable (cell voltage) for the small sample size ($n=5$) in the case of Danish Power Systems[®] (Dapossy) MEA which has the MEA code D.

Table 4.4: Calculation of average cell voltage for Dapossy MEA ($n=5$)

S. #	A	C	I (A cm ⁻²)	T (°C)	V(n=1) (mV)	V(n=2) (mV)	V(n=3) (mV)	V(n=4) (mV)	V(n=5) (mV)	Avg. V (mV)
1	1.2	2	0.2	140	595.79	593.90	601.68	600.27	599.80	598.29
2	3	2	0.2	140	593.66	596.49	596.02	600.74	603.81	598.14
3	1.2	4	0.2	140	606.64	608.05	612.30	615.13	619.14	612.25
4	3	4	0.2	140	606.64	608.05	615.84	614.19	616.07	612.16
5	1.2	2	0.6	140	467.22	463.69	466.99	470.76	467.22	467.18
6	3	2	0.6	140	450.00	456.61	462.74	460.38	463.21	458.59
7	1.2	4	0.6	140	478.78	479.26	485.39	486.57	487.04	483.41
8	3	4	0.6	140	479.02	478.55	482.79	481.38	486.33	481.61
9	1.2	2	0.2	180	638.72	642.26	644.85	644.85	648.15	643.77
10	3	2	0.2	180	637.77	644.62	644.14	645.79	647.45	643.95
11	1.2	4	0.2	180	650.28	654.52	655.70	656.88	659.24	655.32
12	3	4	0.2	180	648.86	651.22	654.29	655.70	658.30	653.67
13	1.2	2	0.6	180	523.13	528.79	529.50	532.33	533.75	529.50
14	3	2	0.6	180	521.72	525.96	524.31	527.85	528.79	525.73

4.1. HT-PEFC MEA characterization with DoE

15	1.2	4	0.6	180	539.88	538.70	543.18	545.07	545.30	542.43
16	3	4	0.6	180	535.16	536.11	538.46	542.00	542.95	538.94

The Yates algorithm is applied as described by Box et al. [91] to determine the main effects of each factor and the factor interactions. Table 4.5 shows the estimates and codes of each main effect and interaction. A similar calculation is carried out with the average cell voltages obtained from 30 replications (n=30) (not shown here).

Table 4.5: Yates algorithm for calculation of main effects and interactions for Daposity MEA

1	2	3	4	Divisor	Estimate (mV)	Effect/interaction	Effect/interaction (Code)
1196.43	2420.84	4311.63	9044.93	16	565.31	Grand Avg.	(1)
1224.41	1890.79	4733.31	-19.35	8	-2.42	λ_a	A
925.76	2596.72	-10.62	114.65	8	14.33	λ_c	C
965.02	2136.59	-8.73	5.29	8	0.66	$\lambda_a * \lambda_c$	AC
1287.72	-0.24	67.24	-990.19	8	-123.77	i	I
1309.00	-10.38	47.41	-15.95	8	-1.99	$\lambda_a * i$	AI
1055.23	-1.46	6.84	16.14	8	2.02	$\lambda_c * i$	CI
1081.36	-7.26	-1.55	8.87	8	1.11	$\lambda_a * \lambda_c * i$	ACI
-0.14	27.98	-530.06	421.68	8	52.71	T	AT
-0.09	39.26	-460.13	1.89	8	0.24	$\lambda_a * T$	T
-8.59	21.28	-10.14	-19.82	8	-2.48	$\lambda_c * T$	CT
-1.79	26.14	-5.80	-8.40	8	-1.05	$\lambda_a * \lambda_c * T$	ACT
0.19	0.05	11.28	69.93	8	8.74	i * T	IT
-1.65	6.79	4.86	4.34	8	0.54	$\lambda_a * i * T$	AIT
-3.77	-1.84	6.74	-6.42	8	-0.80	$\lambda_c * i * T$	CIT
-3.49	0.28	2.12	-4.62	8	-0.58	$\lambda_a * \lambda_c * i * T$	ACIT

The first thing to check is the middle points. Remember that we included them for two specific reasons. To check for the linearity of the response variable and also to check for significant cell degradation. Table 4.6 shows the comparison of middle points for the Daposity MEA for both sample sizes.

Table 4.6: Comparison of middle point standard deviation for Daposity MEA

Sample size (n)	Avg. value 1(M) (mV)	Avg. value 2(M) (mV)	Avg. value 3(M) (mV)	Avg. value 4(M) (mV)	Avg. value 5(M) (mV)	Standard deviation (mV)
5	566.11	565.01	563.33	567.01	567.71	1.73
30	579.77	577.88	576.74	579.62	580.02	1.43

It can be seen that the standard deviation of the cell voltages at the middle points changes very little in going from a small sample size (n=5) to a very large sample size (n=30). This proves that

the response variable behaves in a linear manner [130] and also no significant cell degradation has taken place. In fact the Daposity MEA improves performance over time as will be seen in section 4.2, and thus the average values of the middle points are significantly higher for the sample size of 30.

The next step is to determine the statistically significant main effects and interactions (outliers) by plotting them on a normal probability plot. To plot the effects and interactions normally on standard graph paper, first, all the effects and interactions are arranged in ascending order and a serial number (i) starting at 1, is assigned to each entry. The individual frequency or f score (f_i) and the expected Z value (Z_i) are determined for each of the effects by using the relations given in Eqns. (4.1) and (4.2) below [131];

$$f_i = \frac{i - 0.375}{n + 0.25} \quad (4.1)$$

Where n is the total number of effects (15 in this case).

$$Z_i = P(Z < Z_i) = P(f_i) \quad (4.2)$$

The probabilities can be calculated using the NORM.INV.S function in Microsoft Excel or found in the standard normal distribution tables. Table 4.7 shows f_i and Z_i values for each of the effects and interactions.

Table 4.7: Normal probability calculation table for Daposity MEA

Effect/interaction code	Effect/interaction Value	(i) Effect/int #	(f_i) f score	(Z_i) Expected Z value
I	-123.77	1	0.041	-1.74
AT	-2.48	2	0.107	-1.25
AIT	-2.42	3	0.172	-0.95
AI	-1.99	4	0.238	-0.71
ACI	-1.05	5	0.303	-0.51
AT	-0.80	6	0.369	-0.33
CIT	-0.58	7	0.434	-0.17
AC	0.24	8	0.500	0.00
ACT	0.54	9	0.566	0.17
ACIT	0.66	10	0.631	0.33
CI	1.11	11	0.697	0.51
A	2.02	12	0.762	0.71
IT	8.74	13	0.828	0.95
C	14.33	14	0.893	1.25
T	52.71	15	0.959	1.74

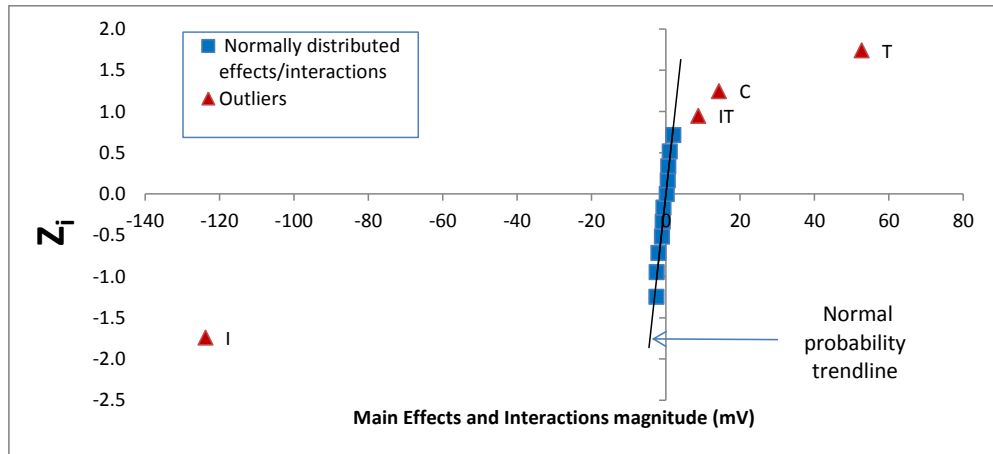


Figure 4.1: Normal probability plot for main effects and factor interactions for Daposp MEA (n=5) (Redrawn from [132])

Figure 4.1 shows the normal probability plot of all the effects and interactions. The effects/interactions lying along a straight line are normally distributed and thus statistically insignificant [91]. In other words, these effects/interactions do not have a significant effect on the response variable (the cell voltage) and thus can be safely ignored when building a statistical regression model. It is the effects/interactions that do not lie along the normal probability trend line and hence are not normally distributed (outliers), which have a statistically significant effect on the response variable and must be included in the regression model [91]. It can be seen that there are four outliers in this case. Three of them are main effects of current density (I), operating temperature (T) and cathode stoichiometry (C). The two factor interaction of current density and operating temperature (IT) is also an outlier. Table 4.8 shows the estimates and statistical significance of all factors and their interactions.

Table 4.8: Main effects and interactions with their statistical significance for Daposp MEA (n=5)

Effect/Interaction (code)	Estimate	Coefficients	Outlier
(I)	565.31	565.31	y
A	-2.42	-1.21	n
C	14.33	7.17	y
AC	0.66	0.33	n
I	-123.77	-61.89	y
AI	-1.99	-1.00	n
CI	2.02	1.01	n
ACI	1.11	0.55	n
T	52.71	26.35	y
AT	0.24	0.12	n
CT	-2.48	-1.24	n
ACT	-1.05	-0.52	n

IT	8.74	4.37	y
AIT	0.54	0.27	n
CIT	-0.80	-0.40	n
ACIT	-0.58	-0.29	n

The final task is to develop the statistical regression models based upon the outliers. A transformation of each factor range to a scale of -1 to 1 is used for this purpose, which is given in Table 4.9. The transformed values between -1 and 1 will be used in the regression model for calculation of the predicted cell voltages. It is also possible to build a regression model that does not require this transformation [101].

Table 4.9: Transformation of factors to a range of -1 to 1

Transformation	-1	-0.5	0	0.5	1
A	1.2	1.65	2.1	2.55	3
C	2	2.5	3	3.5	4
I(A cm⁻²)	0.2	0.3	0.4	0.5	0.6
T (°C)	140	150	160	170	180

The regression model for the Daposty MEA with the smaller sample size (n=5), is formed by only considering the intercept along with the outliers. The coefficients of the outliers are simply half of the calculated estimates in Table 4.5 [133]. Eqn. (4.3) shows the regression model for calculating the cell voltage of this MEA. Note the two subscripts of V (cell voltage). The first one, D in this case, is the MEA code and the second one, 5 in this case, denotes the sample size. This nomenclature is maintained for all the subsequent regression models of different MEAs.

$$V_{D,5} = 565.31 - 61.89I + 7.17C + 26.35T + 4.37IT \quad (4.3)$$

Model validation

Table 4.10 shows the comparison of actually measured cell voltages at selected points and the predicted values using the regression model given in Eqn. (4.3). It is clear that the model is very accurate for such a small sample size, the largest percentage error being 0.57%.

Table 4.10: Comparison of predicted and measured cell voltages at selected points for MEA D

C (Cathode stoichiometry) level	I (Current density) level	T (Temperature) level	Predicted value (mV)	Avg. measured value (mV)	Residual (mV)	%age error
-1	-1	-1	598.05	598.22	0.17	0.03
-1	-1	1	642.01	643.86	1.85	0.29
-1	1	-1	465.53	462.88	-2.65	0.57

4.1. HT-PEFC MEA characterization with DoE

-1	1	1	526.97	527.61	0.64	0.12
1	-1	-1	612.39	612.21	-0.18	0.03
1	-1	1	656.35	654.50	-1.85	0.28
1	1	-1	479.87	482.51	2.64	0.55
1	1	1	541.31	540.68	-0.63	0.12

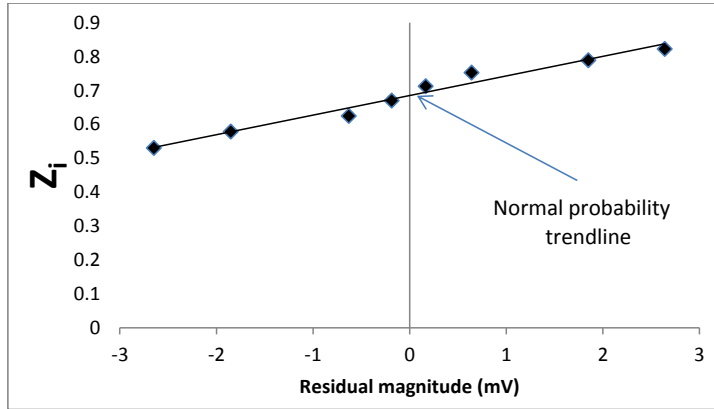


Figure 4.2: Normal probability plot of residuals for Dapossy MEA (Redrawn from [132])

Figure 4.2 shows the residuals from Table 4.10 plotted on normal probability graph. The residuals are found to be normally distributed indeed. This authenticates the accuracy of the regression model [91].

Individual regression models based on the same procedure as presented above are formed for each MEA and sample size. These models are presented in Eqns. (4.4) to (4.10) below;

$$V_{B,5} = 528.27 - 99.43I + 11.13C + 39.07T + 9.02IT \quad (4.4)$$

$$V_{C,5} = 505.37 - 87.10I + 4.99C + 22.93T + 3.96IT \quad (4.5)$$

$$V_{A,5} = 527.96 - 82.18I + 13.01C + 31.31T + 6.78IT \quad (4.6)$$

$$V_{D,30} = 577.93 - 64.54I + 7.93C + 30.05T + 4.54IT \quad (4.7)$$

$$V_{B,30} = 529.27 - 103.15I + 11.66C + 41.99T + 8.92IT \quad (4.8)$$

$$V_{C,30} = 491.53 + 96.01I + 6.97C + 25.72T + 2.98IT \quad (4.9)$$

$$V_{A,30} = 527.77 - 80.83I + 13.49C + 33.10T + 6.60I \quad (4.10)$$

4.1.2 Comparison of regression coefficients and discussion

A comparison of the effect of the sample size on the coefficients of the regression variables is conducted for all four MEAs and is presented below with discussion.

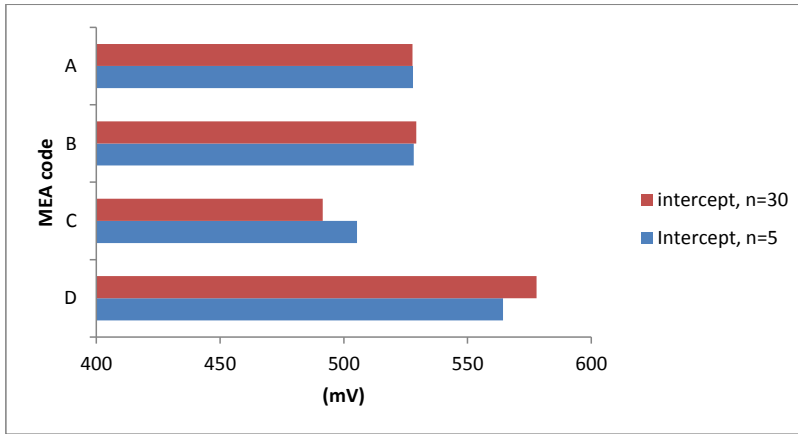


Figure 4.3: Comparison of intercepts (Redrawn from [132])

It can be seen in Figure 4.3 that the intercepts for MEAs A and B show negligible change in the cell voltage from the smaller sample size to the larger sample size, whereas the intercept for MEA C decreases by about 15mV, indicating decreased cell performance over a longer period of time (one replication takes about nine hours for completion, with load cycling between a current density of 200mA cm^{-2} and 600mA cm^{-2} , and also temperature cycling from 140°C to 180°C). MEA D intercept actually increases by about 15mV indicating slightly increased cell performance at the end of testing. Since the intercept is mathematically the value of the response variable with all the significant factors and interactions at their respective mean (0) levels [134], a higher intercept can be interpreted as an indicator of higher cell performance for similar operating conditions in this case.

4.1. HT-PEFC MEA characterization with DoE

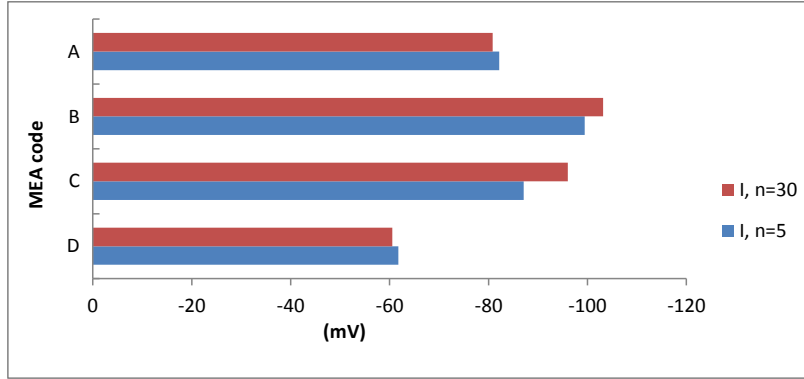


Figure 4.4: Comparison of current density coefficient (I) (Redrawn from [132])

Figure 4.4 shows that the current density coefficients of MEAs B and C decrease slightly for the higher sample size indicating a performance loss (as the current density coefficient is negative) whereas in the case of MEAs A and D, the current density coefficient (I) remains more or less constant. A larger current density co-efficient relates to a narrow operating window for the relevant MEA due to higher voltage loss by the same increase in the load applied. Since the range of the current density ($0.2 - 0.6 \text{ A cm}^{-2}$) falls typically in the ohmic region, a higher current density co-efficient indicates a higher ohmic resistance (R_{Ω}) for the corresponding MEA. MEA D, therefore, has the lowest R_{Ω} .

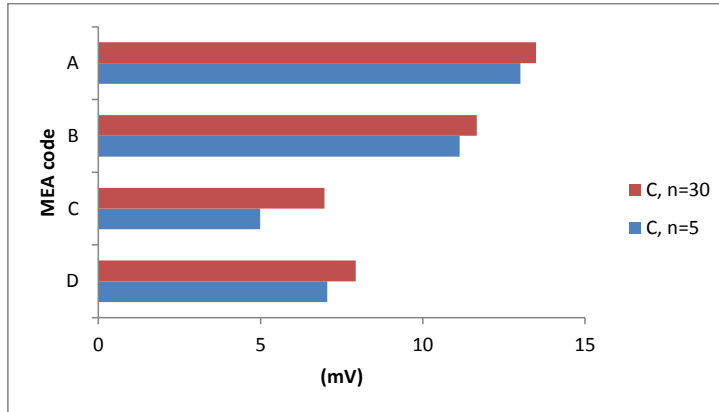


Figure 4.5: Comparison of cathode λ coefficient (C) (Redrawn from [132])

The cathode λ coefficient (C), as depicted in Figure 4.5, increases for all MEAs in moving from the lower to the higher sample size. This indicates increased cell performance with a higher cathode λ with an aging cell. This effect has been reported in the literature [135] and can be attributed to the higher mass transport loss at a lower cathode λ , however, it is interesting to note that the effect of cathode λ for MEAs A and B (carbon cloth GDL) is about two times that of

MEA C and D (carbon paper GDL). This indicates that a higher cathode λ has a larger (positive) effect on the cell voltage in case of the MEAs with carbon cloth as the GDL material. This is due to major differences in the properties of the GDL materials regarding porosity, hydrophobicity, conductivity [136] and compressibility leading to different mass transport behavior [137–140] with similar cell assembly and operating conditions.

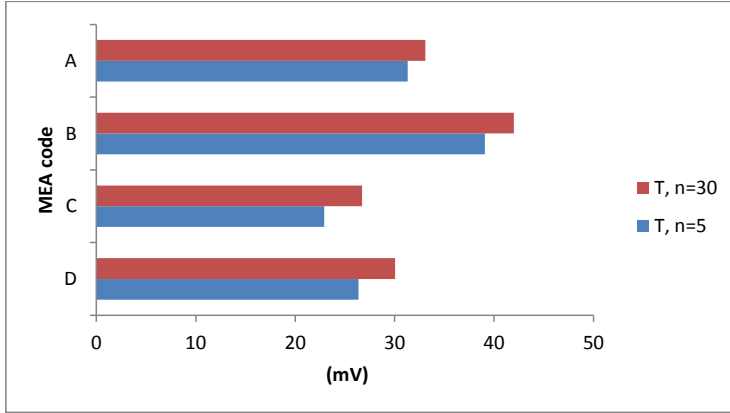


Figure 4.6: Comparison of temperature coefficient (T) (Redrawn from [132])

The temperature coefficient shows a proportional increase in all the investigated MEAs from $n = 5$ to $n = 30$ (Figure 4.6). Higher temperature increases the cell performance by improving reaction kinetics, but it also increases cell degradation [141].

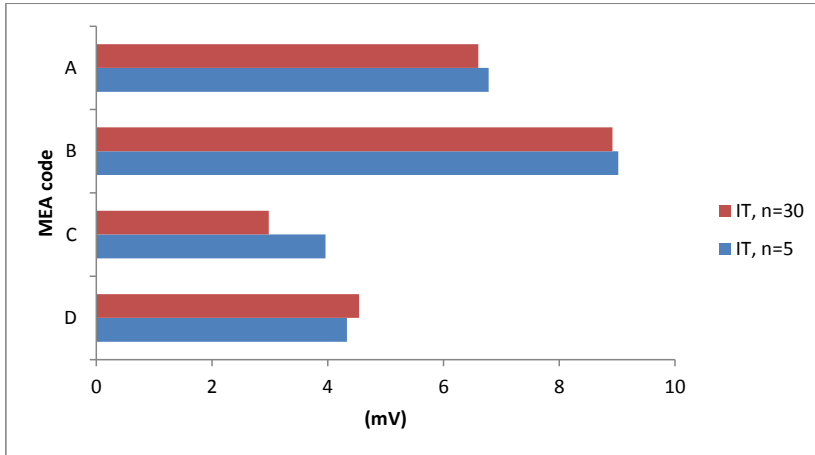


Figure 4.7: Comparison of current density and temperature interaction ($I * T$) (Redrawn from [132])

4.2. MEA degradation

The only significant change (2mV decrease) for the current density and temperature interaction (IT) is seen in MEA C (Figure 4.7). This is also a factor causing slightly lower cell performance due to the weaker interaction, since the interaction is positive and decreases for the higher sample size. Another point of interest is the much higher (almost two times) values of the interaction in MEAs A and B in comparison with MEAs C and D. This can also be explained by the different GDL materials used by the MEAs signifying a stronger interaction of current density and temperature with carbon cloth as GDL material than carbon paper.

A possible extension to the idea of building statistical regression models to characterize MEA performance is to remove the current density from the regression model itself and instead take a complete UI curve for the remaining factor settings. This would give rise to a two level three factor (2^3) DoE in our case with operating temperature and the anode and cathode stoichiometries as the three factors. The advantage is that not only current density data is available for the complete range of cell operation (upto the maximum current density of the cell), but also more measured data points are available for validation of the regression models. These UI curves are termed as DoE UI curves.

4.2 MEA degradation

Since all the four MEAs were operated for about 270 hours excluding the break-in procedure with extensive load and temperature cycling to obtain the necessary data for the DoE characterization campaign therefore some degradation, at least in some of the MEAs, was expected. Figure 4.8 through Figure 4.11 compare the BOL and EOL UI curves for all the four MEAs at the standard operating conditions of 160°C and anode/cathode λ of 2/2 for HT-PEFC MEAs at IEK-3.

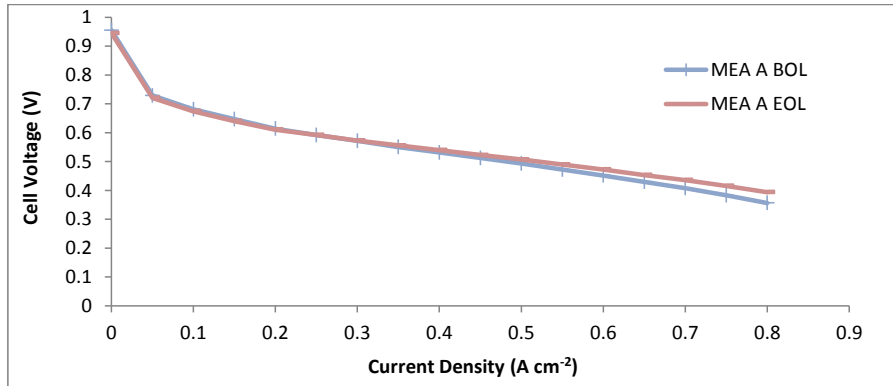


Figure 4.8: BOL and EOL UI curve comparison for MEA A at 160°C with anode/cathode λ of 2/2

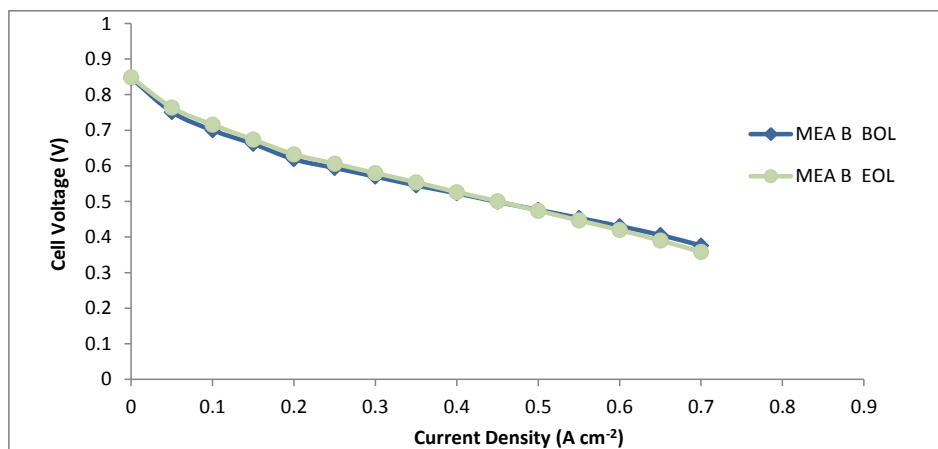


Figure 4.9: BOL and EOL UI curve comparison for MEA B at 160°C with anode/cathode λ of 2/2

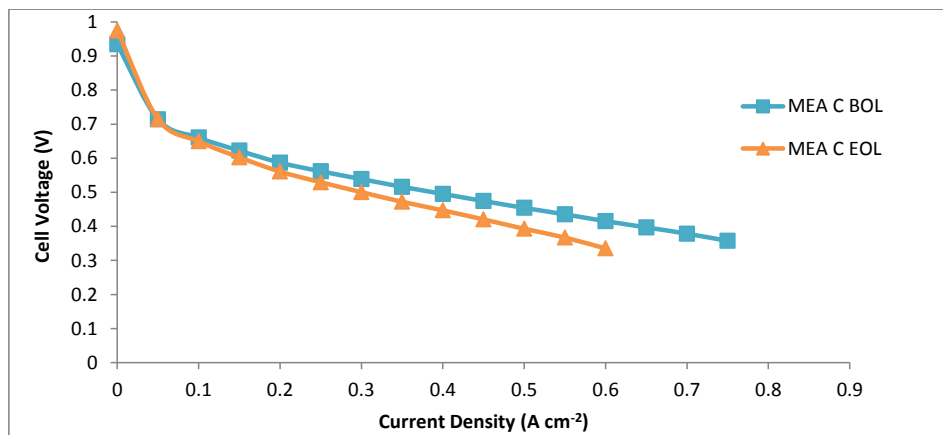


Figure 4.10: BOL and EOL UI curve comparison for MEA C at 160°C with anode/cathode λ of 2/2

4.2. MEA degradation

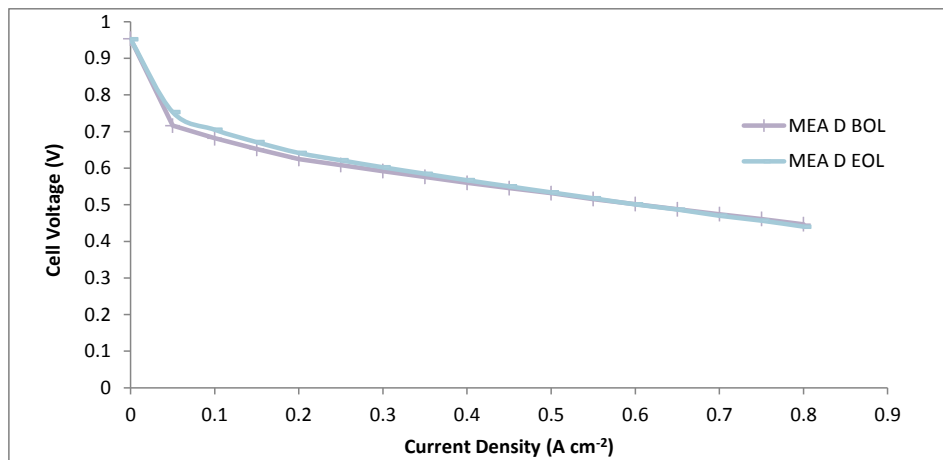


Figure 4.11: BOL and EOL UI curve comparison for MEA D at 160°C with anode/cathode λ of 2/2

The BOL and EOL UI curve comparison of all the four MEAs shows that there is some degradation in the MEAs B and C where as MEAs A and B show little degradation. MEA A shows a significant improvement in the high current density region ($I > 0.5 \text{ A cm}^{-2}$), while MEA D shows improvement in the low current density region ($I < 0.3 \text{ A cm}^{-2}$). Table 4.11 below lists the calculated degradation rates for each MEA upto a current density of 0.6 A cm^{-2} .

Table 4.11: Degradation rates for all MEAs at current densities upto 0.6 A cm^{-2}

Current density (A cm^{-2})	Degradation Rates ($\mu\text{V h}^{-1}$)			
	MEA A	MEA B	MEA C	MEA D
0	33.96	10.50	-158.89	3.58
0.05	28.98	69.44	-1.85	-133.58
0.1	24.00	86.50	43.70	-83.69
0.15	23.15	66.83	77.16	-66.81
0.2	12.42	77.27	103.14	-59.17
0.25	-0.80	66.83	126.37	-46.52
0.3	-4.14	53.72	151.49	-38.02
0.35	-20.70	48.44	172.87	-31.29
0.4	-28.14	18.33	190.55	-25.37
0.45	-36.42	10.50	211.92	-16.91
0.5	-48.00	-13.11	241.65	-6.77
0.55	-61.22	-38.00	268.62	-7.63
0.6	-72.80	-60.27	315.59	2.50

It can be seen that MEAs A and D show mostly a negative degradation rate (and hence improved cell performance) at the EOL, whereas MEAs B and C have mostly a positive degradation rate.

MEA C shows the highest degradation at almost all current densities. It is deduced that MEAs A and D are more robust for operation in fluctuating operating conditions.

4.3 Summary

This chapter deals with the characterization of four commercially available HT-PEFC MEAs by using the DoE method. The main results are listed as follows;

1. It is demonstrated that the DoE can be successfully employed to characterize MEA performance, hence considerably reducing the experimental effort while maintaining or improving the accuracy of results.
2. Statistical regression models are developed to predict MEA performance within a preselected range of operating parameters. These models are based on a low sample size ($n=5$) and a high sample size ($n=30$). A comparison of the model coefficients stipulates that the smaller sample size ($n=5$) is adequate for a first evaluation of the MEA.
3. The DoE application can be further extended by utilizing the DoE UI curves for MEA characterization.
4. Two of the MEAs (A and D) improve in performance while the other two (B and C) show some degradation.

4.3. Summary

5 In-house Assembled MEA Study

This chapter is dedicated to finding the best material parameters for the construction of the HT-PEFC MEA assembled at the IEK-3. The previous chapter focused on the characterization of commercial HT-PEFC MEAs on the basis of most important operating conditions such as current density, anode and cathode stoichiometries and the operating temperature. Besides developing some valuable statistical models for reasonably accurate performance prediction of the MEAs, this also helped in estimating the effects of each operating condition on the cell voltage in the form of main effects and factor interactions of the considered operating conditions. The next step is to evaluate the effect of material parameters on the HT-PEFC performance, which is unfortunately not possible with the commercial MEAs. On one hand, the material parameters are fixed and quite often confidential, for the commercial MEAs and on the other hand, no post mortem analysis of the used MEAs is allowed due to non-disclosure agreements (NDA) with the manufacturers.

The influence of many important material parameters on the MEA performance is nevertheless, very significant and hence, must be investigated in a detailed manner to come up with a better performing MEA. It is therefore decided, to use in-house assembled HT-PEFC MEAs to investigate the most important material parameters influencing cell performance in a systematic manner utilizing both the DoE and EIS methods.

5.1 Material parameters and MEA preparation

5.1.1 Material parameters

Three of the most important material parameters (factors) for HT-PEFC operation are the Pt loading, CCL thickness and the PADL. A brief literature review of these parameters is already presented in section 1.1.2 and a short discussion of each factor is given in the next paragraphs.

The Pt loading is of course vital for the respective anode and cathode electrochemical reactions, but also it is very important from a cost point of view as Pt costs can account for upto 50% of the total cost of a fuel cell stack [72]. Different manufacturing techniques for the electrodes and the whole MEA have been tried to improve cell performance while reducing Pt loading in HT-PEFCs [126,142]. This will continue to be a very intense area of research until a reliable non-noble metal catalyst can replace platinum for PEFC operation.

The CCL thickness is also of utmost importance, since the ORR taking place on the cathode side is known to be the rate determining step with hydrogen operation [13]. The CCL thickness also affects vitally important electrochemical parameter such as the exchange current density and the Tafel slope [143]. The CCL thickness faces contradicting requirements from a design viewpoint. On the one hand, enough catalyst loading is needed for the required catalytic activity

5.1. Material parameters and MEA preparation

necessitating a thicker CCL, while on the other hand increasing CCL thickness beyond a certain limit can dramatically increase the protonic and mass transport resistances of the fuel cell [144]. Therefore, a delicate balance is required between catalyst loading and the CCL thickness to achieve maximum cell performance.

The PADL is important because the PA provides the protonic conductivity in the HT-PEFC, and an optimum PADL is therefore necessary for best cell performance. As the cell is operated, the PA is redistributed within the membrane as well as in the catalyst layers, and this redistribution is known to influence the overall cell performance strongly [52,145]. Furthermore, there is a strong interaction between CCL thickness and PADL [146], which must be investigated in detail.

The ranges for each of these factors are chosen based on literature and in-house experience regarding HT-PEFC MEA assembly and performance. Typical Pt loading values for both anode and cathode CLs in PBI based HT-PEFC are above 0.7mg cm^{-2} [142], with 1mg cm^{-2} being the norm in the CCL of commercial MEAs [127,128]. A range of 0.6 to 1mg cm^{-2} is selected based on these observations with the goal of reducing Pt loading of the CCL without much performance loss if possible. The CCL thickness is significantly higher in HT-PEFC in comparison with the LT-PEFC due to the higher Pt loading [34]. For LT-PEFC it can be as low as $15\mu\text{m}$ [147], whereas the norm in HT-PEFC is from $40\mu\text{m}$ upto $125\mu\text{m}$ [148,149]. The PADL range described in literature is also wide but a doping level of 15mg cm^{-2} has been used with reasonable cell performance in the in-house MEAs and it is decided to try to increase this level upto 25mg cm^{-2} in an effort to increase the protonic conductivity of the membrane [150] and achieve better cell performance. Table 5.1 summarizes the ranges and codes of each of the factors used in this study.

Table 5.1: Considered factors with their respective ranges

Serial #	Parameter	Code	Unit	Range
1	PADL	A	(mg cm^{-2})	15-25
2	Pt loading	B	(mg cm^{-2})	0.6-1
3	CCL thickness	C	(μm)	60-120

Since a DoE study is planned, a 2 level 3 factor (2^3) design matrix is formed with the three factors and their respective ranges. This results in eight unique MEAs with different factor levels as shown in Table 5.2.

Table 5.2: MEA IDs and their factor levels

Serial #	MEA ID	PADL (A) (mg cm^{-2})	Pt loading (B) (mg cm^{-2})	CCL thickness (C) (μm)
1	MEA 1	15	0.6	60
2	MEA 2	25	0.6	60
3	MEA 3	15	1	60

4	MEA 4	25	1	60
5	MEA 5	15	0.6	120
6	MEA 6	25	0.6	120
7	MEA 7	15	1	120
8	MEA 8	25	1	120

Each of these MEAs is also given a unique ID for easier subsequent referencing. The next step is to prepare these MEAs.

5.1.2 MEA preparation

The membranes and GDEs are prepared as described in section 3.1. The MEAs with a PADL of 25mg cm^{-2} use the normally doped membrane and additional 5mg cm^{-2} PA is added on both the anode and cathode GDEs. Two different types of catalysts, 20 wt % and 40 wt % Pt/C, are used for preparing the catalyst ink. To achieve different catalyst loadings and CCL thicknesses, inks with different proportion of ingredients are used. The anode GDEs are always prepared with a Pt loading of 0.6mg cm^{-2} . The absolute deviation of the Pt loading is 0.05mg cm^{-2} . Table 5.3 summarizes the prepared MEAs and their respective recipes for the CCL. The anode catalyst layer recipe is always the same with 1000mg 20 wt% Pt, 3mL water, 19.5mL isopropanol and 744 μL PTFE. This leads to a Pt loading of 0.6mg cm^{-2} and a CL thickness of $60\mu\text{m}$ for all the anodes.

Table 5.3: Cathode catalyst layer recipes and spacer thicknesses used for GDE preparation (Reprinted with permission from [151], Copyright [2017], The Electrochemical Society.)

MEA ID	Recipe for the CCL	Thickness of spacer (mm)
MEA 1	1000mg 20 wt.% Pt/C, 3.0mL water, 19.5mL isopropanol, 744 μL PTFE	0.5
MEA 2	1000mg 20 wt.% Pt/C, 3.0mL water, 19.5mL isopropanol, 744 μL PTFE	0.5
MEA 3	500mg 40 wt.% Pt/C, 1.178mL water, 7.66mL isopropanol, 225 μL PTFE	0.4
MEA 4	500mg 40 wt.% Pt/C, 1.178mL water, 7.66mL isopropanol, 225 μL PTFE	0.4
MEA 5	16 wt.% Pt/C (800mg 20 wt.%	0.8

5.1. Material parameters and MEA preparation

	Pt, 200mg C), 3.0mL water, 19.5mL isopropanol, 744μL PTFE	
MEA 6	16 wt.% Pt/C (800mg 20 wt.% Pt, 200mg C), 3.0mL water, 19.5mL isopropanol, 744μL PTFE	0.8
MEA 7	1000mg 20 wt.% Pt/C, 3.0mL water, 19.5mL isopropanol, 744μL PTFE	1
MEA 8	1000mg 20 wt.% Pt/C, 3.0mL water, 19.5mL isopropanol, 744μL PTFE	1

The ratios of PTFE binder, Pt/C catalyst and additional carbon (if any) in the CCL of each of the MEAs are presented in Table 5.4.

Table 5.4: Ratios (by weight) of PTFE, Pt/C catalyst and additional carbon in the CCL of each MEA

MEA ID	PTFE Binder	Pt/C Catalyst	Additional Carbon
MEA 1	2	3	0
MEA 2	2	3	0
MEA 3	2	5	0
MEA 4	2	5	0
MEA 5	2	2.4	0.3
MEA 6	2	2.4	0.3
MEA 7	2	3	0
MEA 8	2	3	0

5.2 DoE study

5.2.1 Experimental

The MEAs presented in Table 5.2 are used as the design points for the DoE study of the in-house assembled MEAs. These MEAs are assembled, one by one and then after running the break-in procedure, three UI curves are measured for anode/cathode stoichiometries of 2/2 and 2/6 respectively with hydrogen on the anode side and air on the cathode side and an operating temperature of 160°C.

The UI curves are averaged and the cell voltage at selected points (200, 400 and 600mA cm⁻²) is used as the response variable for the DoE design matrix. This gives two separate sets of data for the designed experiment for stoichiometries of 2/2 and 2/6 respectively. This is done not only to compare the effects of cathode stoichiometry on cell performance, but also due to the fact that the important electrochemical parameters of the CCL are determined by EIS analysis in section 5.3 at a stoichiometry of 2/6. The cell performance at a high cathode stoichiometry can then be matched with the corresponding electrochemical parameters. Table 5.5 and Table 5.6 present the (averaged) cell voltages at the predetermined current densities for stoichiometries of 2/2 and 2/6 respectively for each MEA.

Table 5.5: Cell voltage at selected current densities for anode/cathode λ of 2/2, T= 160°C

MEA ID	Cell voltage in mV @		
	200mA cm ⁻²	400mA cm ⁻²	600mA cm ⁻²
1	576	490	410
2	502	363	220
3	582	495	414
4	440	274	108
5	609	524	446
6	534	391	214
7	591	509	435
8	602	496	396

Table 5.6: Cell voltage at selected current densities for anode/cathode λ of 2/6, T= 160°C

MEA ID	Cell voltage in mV @		
	200mA cm ⁻²	400mA cm ⁻²	600mA cm ⁻²
1	587	503	434
2	584	480	378
3	595	513	440
4	528	415	315

5.2. DoE study

5	616	539	470
6	598	506	411
7	601	510	430
8	628	537	452

Each MEA is replicated twice and both sets of data are used for analysis of MEA performance since it is impractical to use a new MEA for each UI curve. This gives us a sample size of 6, which is admittedly low, but still can give a reasonably accurate model for cell performance based on the results from the previous chapter. The data and results are analyzed with the help of the commercial statistical software Statgraphics Centurion XVII version 17.1.12 (64 bit) which has a dedicated DoE experimental design wizard for constructing and analyzing experiments with the DoE. The cell voltages from all the MEAs are used as input response values to the experimental design wizard. The main effects of each factor and the three factor interactions are determined. Due to a low sample size, all the factors and their interactions are evaluated. The region of best cell performance is determined with contour plots using the desirability approach. The desirability is defined as the factor settings that maximize the response variable [152] (cell voltage, in our case). Therefore, a desirability level close to 1 suggests best factor setting and vice versa. The goal of most DoE studies is to find the factor settings which can maximize the desirability.

5.2.2 Results

The results are presented in the form of Pareto charts, which simply list the factors affecting cell performance in descending order, and contour plots, which help depict the best factor settings to maximize the response variable as described in the previous section.

Case of 2/2 Stoichiometry

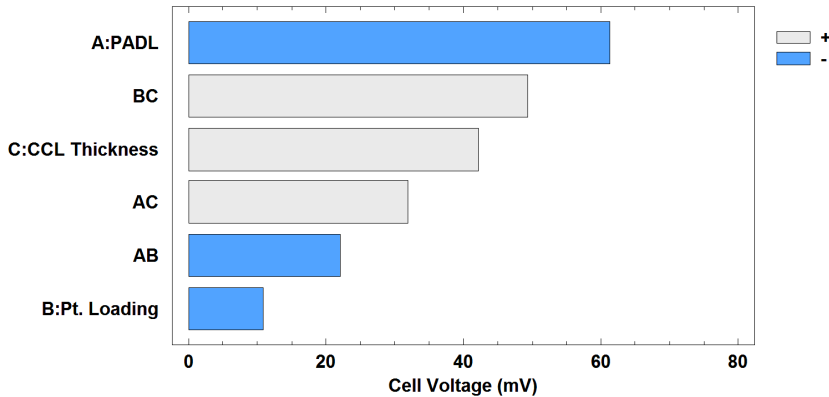
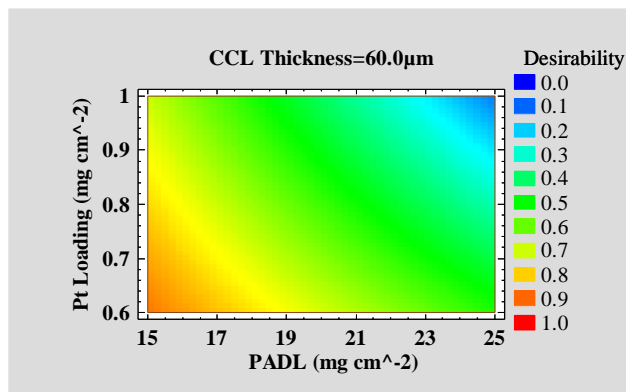


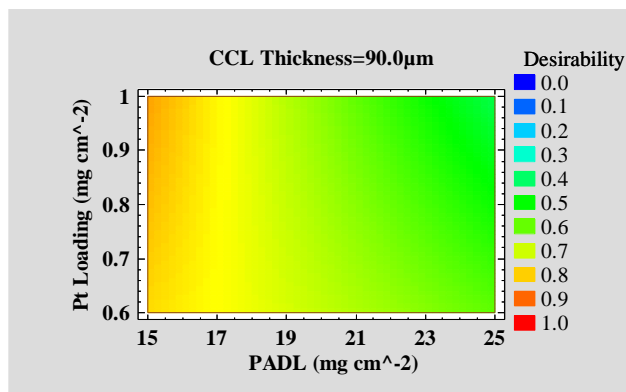
Figure 5.1: Pareto chart for 200mA cm⁻² and anode/cathode λ of 2/2, T= 160°C

The PADL main effect is the dominant factor at this current density with a voltage loss of slightly above 60mV by increasing the PADL from 15 to 25mg cm⁻². The two factor interaction of Pt loading and CCL thickness (BC) is the second largest in magnitude. It can be seen in Figure 5.1 that PADL, Pt loading and their interaction (AB) all have a negative effect on the cell voltage (i.e. the cell voltage goes down as their level is increased). This is especially significant for the case of Pt loading as it indicates a potential for decreasing the Pt loading of the CCL without significant performance loss resulting in sizable cost reduction. But since the two factor interaction of Pt loading with CCL thickness (BC) is much higher in magnitude and also positive, it turns out that a higher Pt loading is still desirable due to its interaction with the CCL thickness.

a)



b)



c)

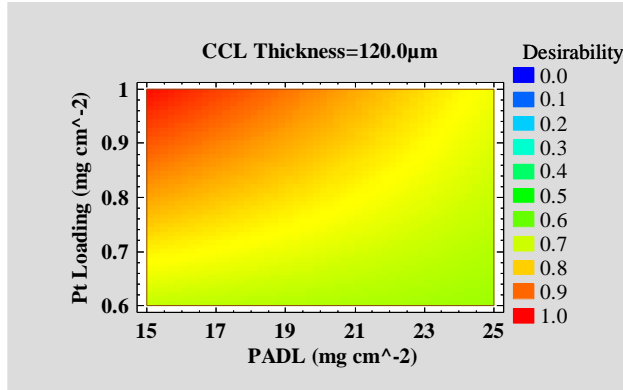


Figure 5.2: Contour plots of desirability for 200mA cm^{-2} and anode/cathode λ of 2/2, $T = 160^\circ\text{C}$

Figure 5.2 shows the desirability of the factors. Keeping in mind that a higher desirability shows the factor settings that tend to maximize the response variable, it can be seen that the highest desirability (close to 1) is with values of CCL thickness $120\mu\text{m}$, PADL 15mg cm^{-2} and Pt loading of 1mg cm^{-2} , whereas the desirability approaches zero with values of CCL thickness $60\mu\text{m}$, PADL 25mg cm^{-2} and Pt loading of 1mg cm^{-2} . This means that a higher CCL thickness along with a high Pt loading and a low PADL maximize cell performance. This seems to contradict the fact that the Pt loading main effect is negative. This is not the case, since as discussed previously, the two factor interactions of the Pt loading are much larger in magnitude than its main effect and since they are implicitly included in the contour plot, we can see that although the main effect of Pt loading is negative, a higher Pt loading is still best for cell performance when both the interactions are taken into account.

Another point of interest is the corner with factor settings of CCL thickness $60\mu\text{m}$, PADL 15mg cm^{-2} and Pt loading of 0.6mg cm^{-2} (Figure 5.2a). The desirability value is still in the vicinity of 0.9 indicating close to maximum cell voltage. The other corner with factor settings of CCL thickness $120\mu\text{m}$, PADL 15mg cm^{-2} and Pt loading of 1mg cm^{-2} (Figure 5.2c) has slightly higher desirability. It can be seen that the biggest decline in cell voltage is by moving from the left to right in Figure 5.2a, i.e. by increasing the PADL. This means that an increase in the PADL is very bad for cell performance with a $60\mu\text{m}$ CCL. This effect is not so pronounced in the case of a $120\mu\text{m}$ CCL. Increase in the PADL has a much lower effect on the desirability at a Pt loading of 0.6mg cm^{-2} than in the case of 1mg cm^{-2} at the CCL thicknesses of 90 and $120\mu\text{m}$.

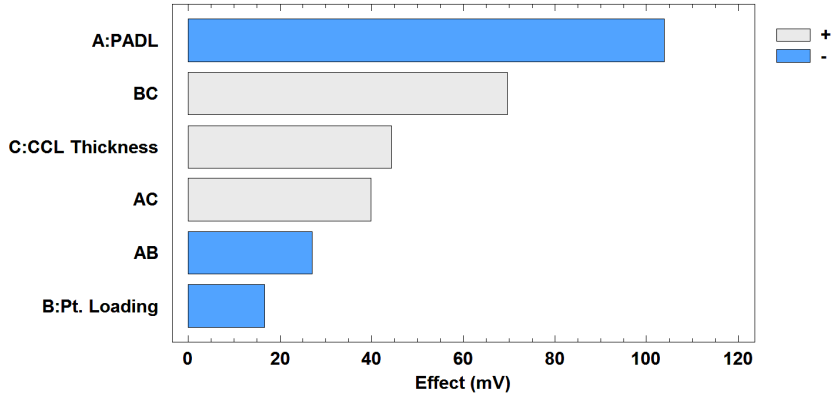
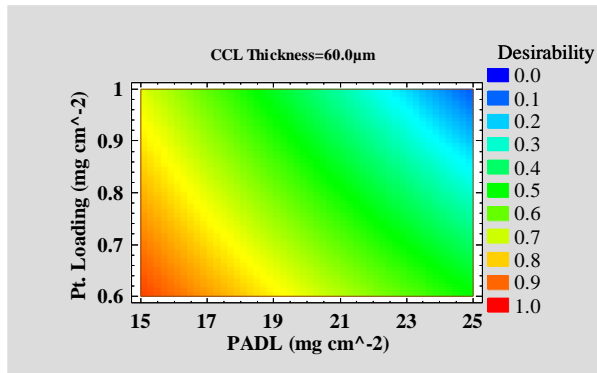


Figure 5.3: Pareto chart for 400mA cm^{-2} and anode/cathode λ of 2/2, $T=160^\circ\text{C}$

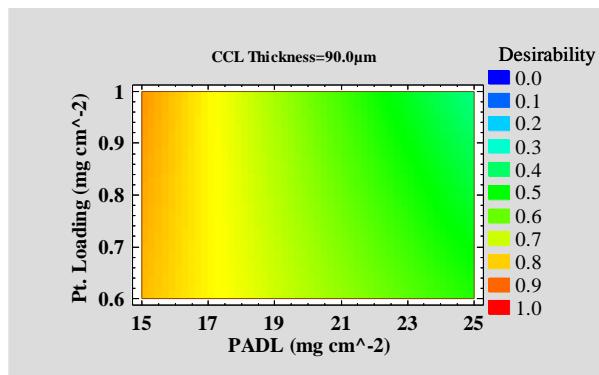
The main effects and interactions of the factors for a current density of 400mA cm^{-2} are depicted in Figure 5.3. The trends are quite similar to those in the case of 200mA cm^{-2} but the magnitudes of the effects are higher due to the higher current density and thus lower cell voltage.

a)



5.2. DoE study

b)



c)

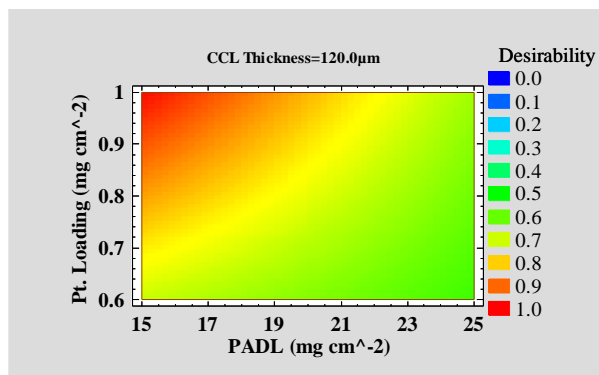


Figure 5.4: Contour plots of desirability for 400mA cm⁻² and anode/cathode λ of 2/2, T= 160°C

The desirability trends are also similar to the trends of 200mA cm⁻² (see Figure 5.2) for this current density as depicted in Figure 5.4 with a notable improvement in the cell performance at intermediate doping levels (upto 20mg cm⁻²).

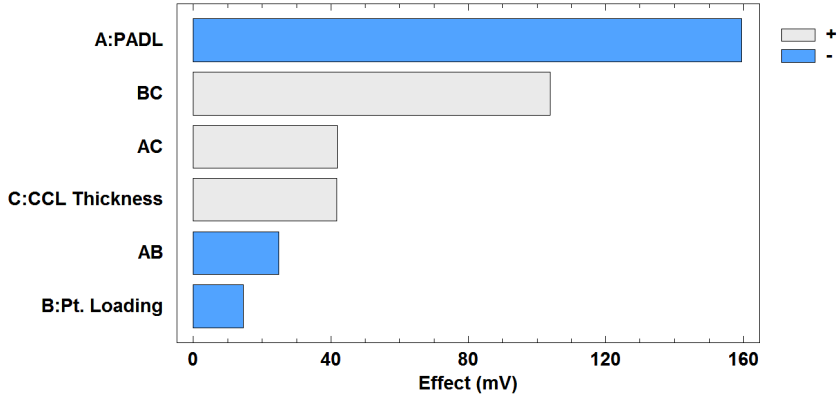
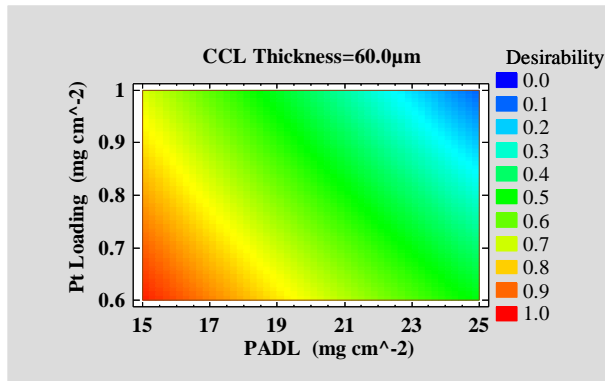


Figure 5.5: Pareto chart for 600mA cm^{-2} and anode/cathode λ of 2/2, $T=160^\circ\text{C}$

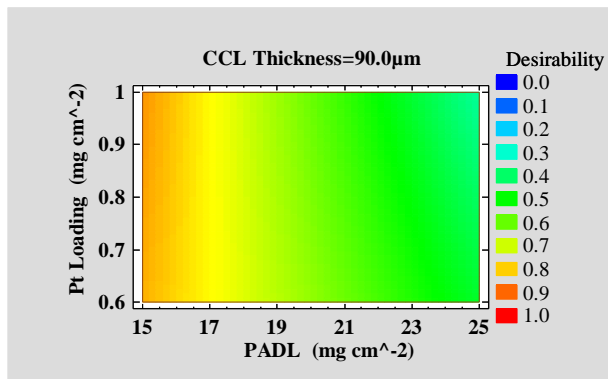
The trend remains similar for a current density of 600mA cm^{-2} with the exception that the CCL thickness main effect is now slightly lower than its interaction (AC) with PADL as shown in Figure 5.5. It shows that the CCL thickness main effect decreases whereas its interaction with PADL increases with current density.

a)



5.2. DoE study

b)



c)

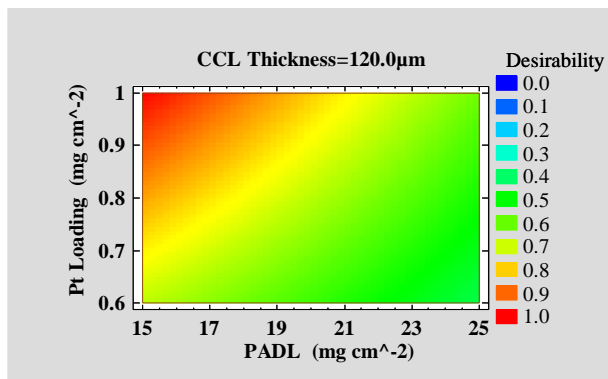


Figure 5.6: Contour plots of desirability for 600mA cm⁻² and anode/cathode λ of 2/2, T= 160°C

The contour plots shown in Figure 5.6 also have similar trends as for the previous two current densities but the high desirability areas from the bottom left of Figure 5.6a and the top left of Figure 5.6c have grown larger indicating increased tolerance of a higher PADL at higher current density.

Case of 2/6 Stoichiometry

The dataset for anode/cathode stoichiometry of 2/6 is analyzed in similar fashion.

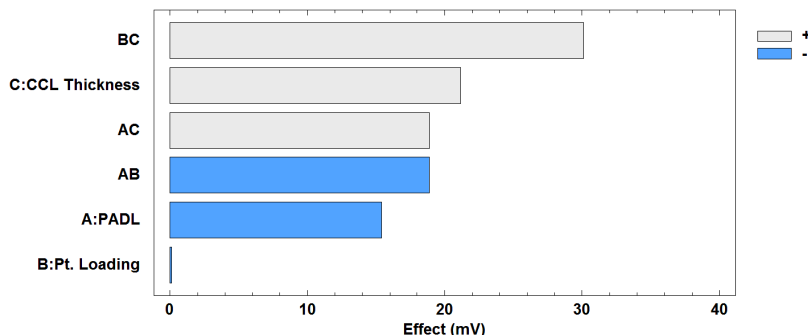
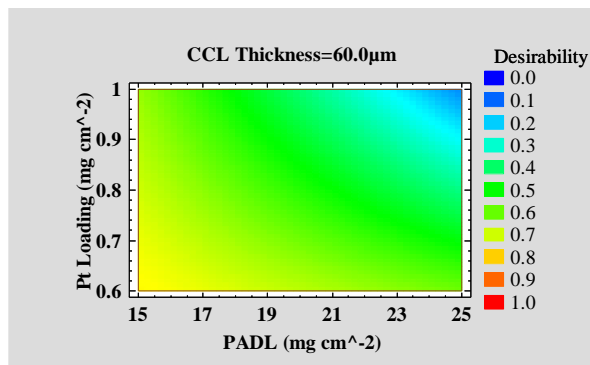


Figure 5.7: Pareto chart for 200mA cm^{-2} and anode/cathode λ of 2/6, $T=160^\circ\text{C}$

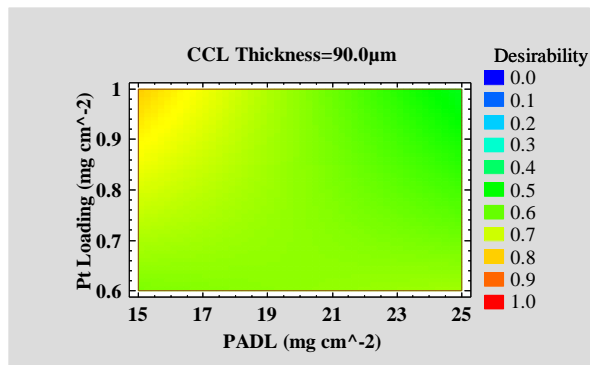
Figure 5.7 depicts the main effects and interactions for a current density of 200mA cm^{-2} with a higher cathode stoichiometry and the results are in stark contrast to those for the lower stoichiometry case. First of all, the negative effects remain the same as before; the PADL, Pt loading and their two factor interaction (AB), but their magnitudes are much lower and they are the last three effects listed on the Pareto chart signifying that they affect the cell performance the least. The CCL thickness and its interactions with the other two factors all affect cell performance positively and the CCL thickness and Pt loading interaction (BC) is the largest in magnitude. This again shows that although the main effect of Pt loading is negligible, yet it is involved in a highly significant interaction and therefore cannot be judged on the basis of its main effect alone. The combined effect of the main effects and two factor interactions is only visible in the contour plots presented in Figure 5.8. The highest desirability is on the top left for the higher CCL thickness of $120\mu\text{m}$ (Figure 5.8c) signifying best cell performance with high CCL thickness and platinum loading, but the lowest PADL level. Interestingly, the cell performance does not deteriorate dramatically even with increasing PADL, reaching a desirability of about 0.8 on the highest level of PADL, which is slightly higher as compared to the corresponding case for a stoichiometry of 2/2. This shows that the negative effect of PADL on cell voltage is significantly reduced in this case; a deduction also apparent from the Pareto chart. The worst desirability is still seen in the same region with high Pt loading and PADL, but low CCL thickness as for the case of 2/2 stoichiometry (Figure 5.8a, top right corner).

5.2. DoE study

a)



b)



c)

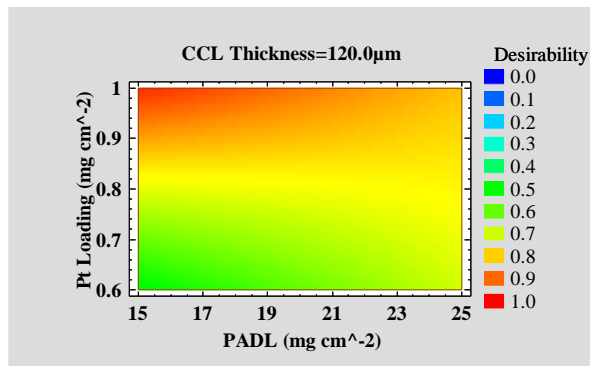


Figure 5.8: Contour plots of desirability for 200mA cm^{-2} and anode/cathode λ of 2/6, $T = 160^\circ\text{C}$

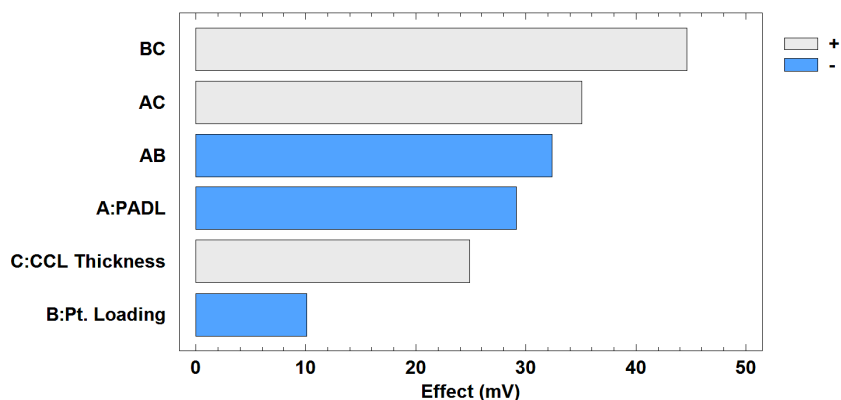
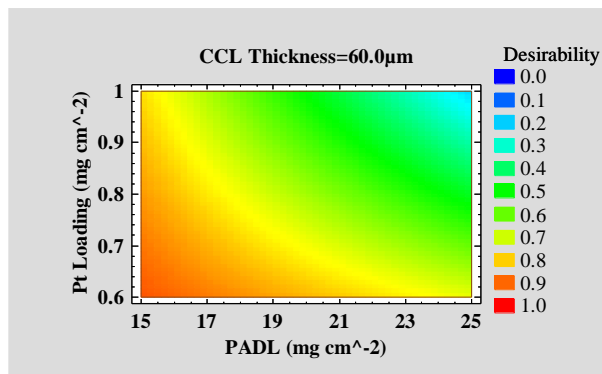


Figure 5.9: Pareto chart for 400mA cm^{-2} and anode/cathode λ of 2/6, $T=160^\circ\text{C}$

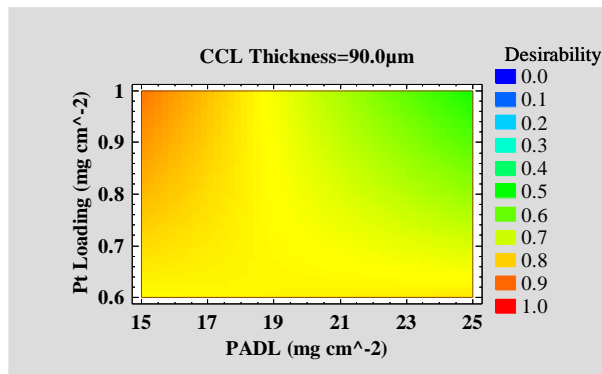
The trends of the effects seen in Figure 5.9 and Figure 5.10 (below) are similar to those at the current density of 200mA cm^{-2} , with the exceptions that the CCL thickness main effect is now the second lowest but it is still involved in two of the greatest interactions, with Pt loading (BC) and with PADL (AC) respectively.

a)



5.2. DoE study

b)



c)

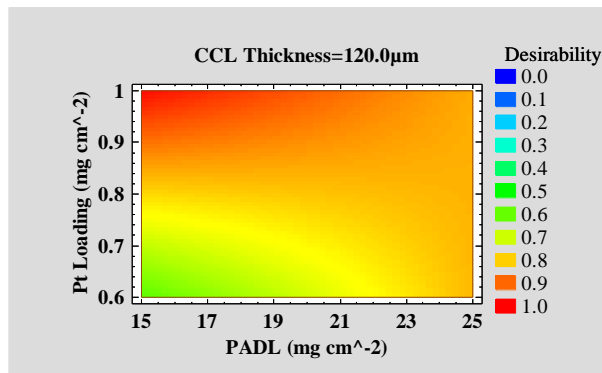


Figure 5.10: Contour plots of desirability for 400mA cm^{-2} and anode/cathode λ of 2/6, $T = 160^\circ\text{C}$

All the effects have a higher magnitude and the overall desirability is higher in the investigated region which is evident by the large yellow region (desirability between 0.7 and 0.8) as compared to the same region at a current density of 200mA cm^{-2} (see Figure 5.8), where it is mostly green (desirability between 0.4 and 0.6). The extreme value trends for the desirability remain the same, albeit, the worst desirability region is slightly shrunk in comparison to 200mA cm^{-2} and at intermediate doping levels (upto 20mg cm^{-2}) for a low CCL thickness, there is a high desirability.

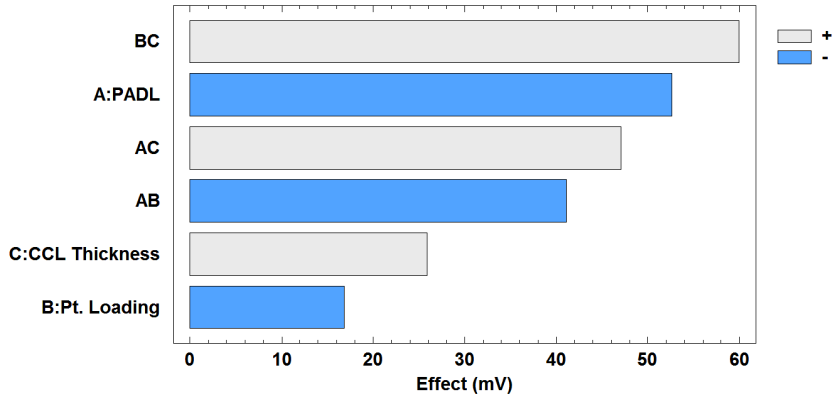
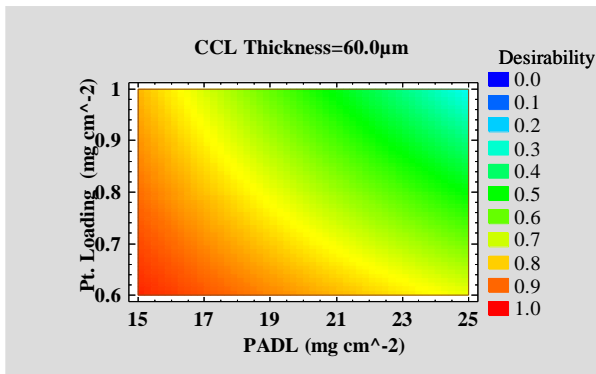


Figure 5.11: Pareto chart for 600mA cm^{-2} and anode/cathode λ of 2/6, $T = 160^\circ\text{C}$

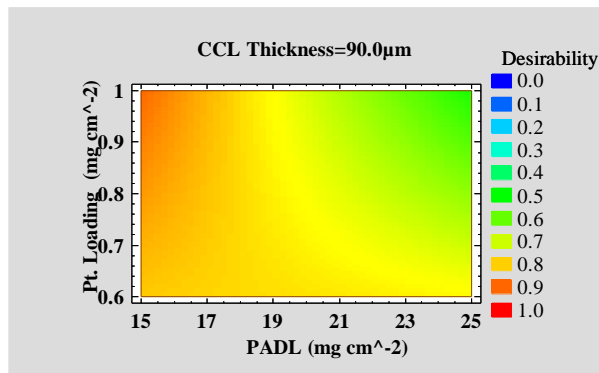
At the highest current density of 600mA cm^{-2} , the PADL main effect once again rises to the second largest effect in magnitude and all the effects are higher in magnitude than their previous counterparts (Figure 5.11).

a)



5.2. DoE study

b)



c)

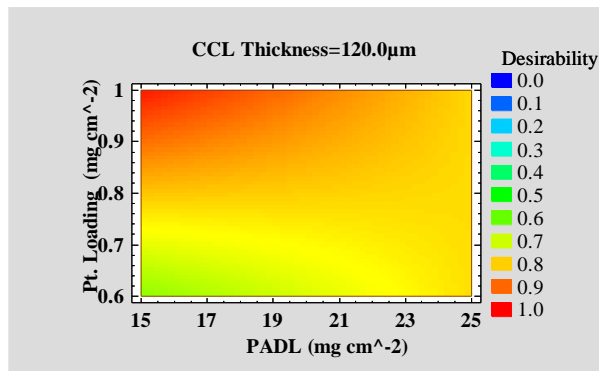


Figure 5.12: Contour plots of desirability for 600mA cm^{-2} and anode/cathode λ of 2/6, $T=160^\circ\text{C}$

The contour plots of desirability (Figure 5.12) now have a very small low desirability region, which continues to shrink from the previous current density (400mA cm^{-2}) result and similarly PADL tolerance zone for low CCL thickness has grown following the trend from the last current density upto 22mg cm^{-2} .

Discussion

It can be seen from the presented results that there are some trends to the variation of cell voltage which are summarized below;

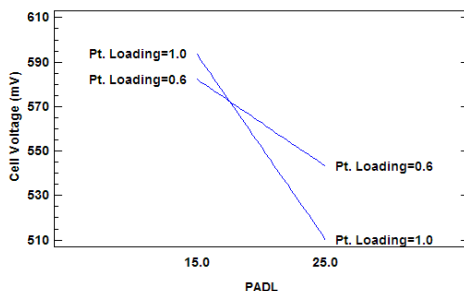
1. PADL has a highly negative effect on cell voltage in most cases. Only in the case of high stoichiometry (2/6) and low current density (200 and 400mA cm^{-2}) it is the second highest negative main effect after its interaction with Pt loading (AB). Its interaction with CCL thickness (AC) is positive and significant in all cases with higher magnitudes in the high

stoichiometry case (2/6). AB, the interaction of PADL with Pt loading, is negative in all cases but much more significant in the high stoichiometry case.

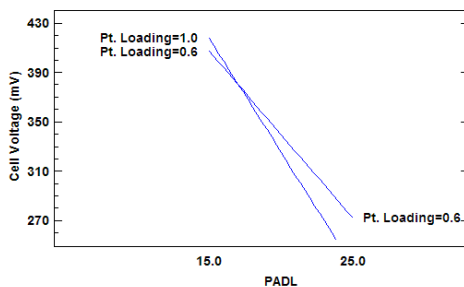
2. Pt loading itself does not have a significant effect on the cell voltage but its two factor interactions with CCL thickness and PADL are always significant. The former is always positive and higher in the high stoichiometry case than the low stoichiometry case. Whereas the latter is always negative and more significant in case of high stoichiometry.

3. CCL thickness main effect has always a positive value in all cases, signifying an increased cell performance with a higher CCL thickness. Also, its interactions with Pt loading and PADL are positive and significant in all cases.

It is evident from the above that all three factors interact with each other strongly and also have significant main effects with the exception of Pt loading. It makes sense to compare these interactions for the two cases one by one. This is done in Figure 5.13 through Figure 5.18. The discussion is presented below each figure.



(a) Current density of 200mA cm^{-2}

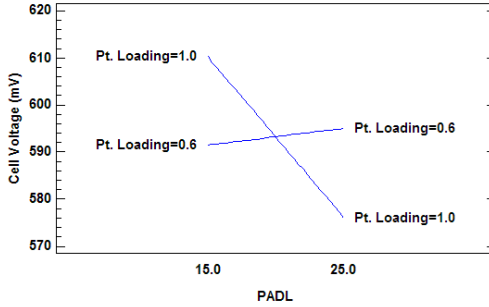


(b) Current density of 600mA cm^{-2}

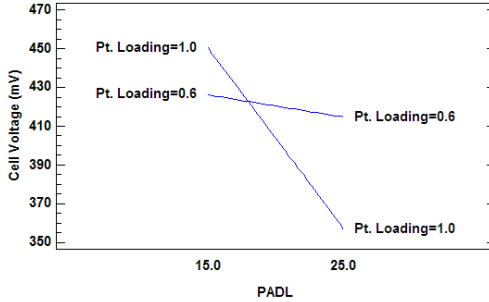
Figure 5.13: PADL and Pt loading interaction (AB) comparison for anode/cathode λ of 2/2

5.2. DoE study

The negative effect of PADL is slightly lower at the lower Pt loading (0.6) at both current densities. It is known that a high amount of PADL fills the CCL pores thus impeding diffusion of oxygen to the TPBs [151,153]. This is the chief cause of decreased cell performance as observed here.



(a) Current density of 200mA cm⁻²



(b) Current density of 600mA cm⁻²

Figure 5.14: PADL and Pt loading interaction (AB) comparison for anode/cathode λ of 2/6

The lower effect of PADL on lower loadings is more pronounced in the high stoichiometry case. In fact, there is a slight increase in cell voltage in Figure 5.14 (a) for the lower Pt loading at the higher PADL. This is consistent with the explanation provided in the last paragraph regarding lower oxygen diffusibility to the TPB in case of higher Pt loading for the same CCL thickness.

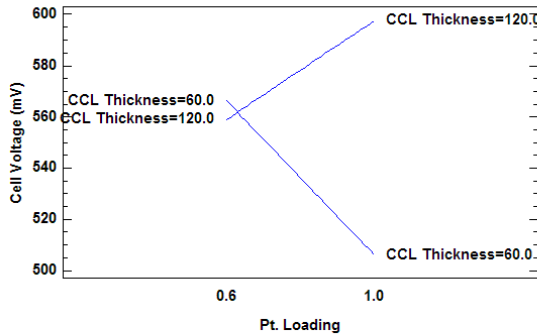
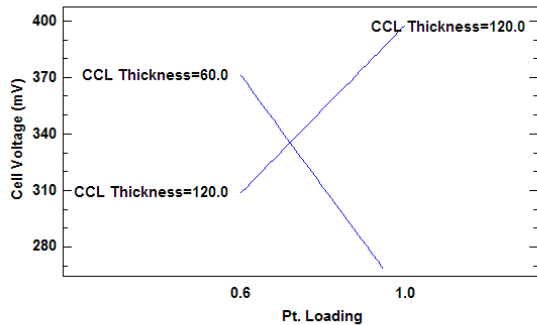
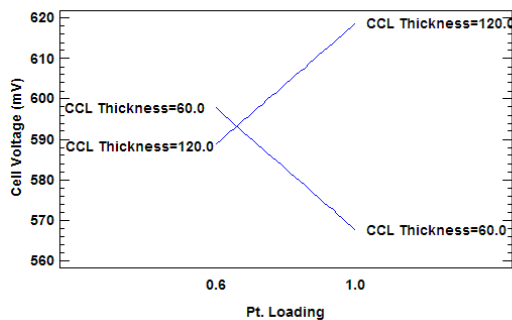
(a) Current density of 200mA cm⁻²(b) Current density of 600mA cm⁻²

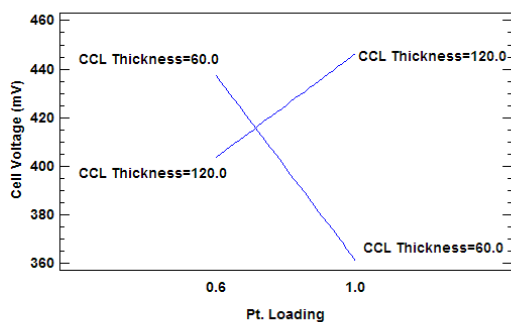
Figure 5.15: Pt loading and CCL thickness interaction (BC) comparison for anode/cathode λ of 2/2

Cell voltage increases by increasing the Pt loading in case of a thicker CCL where as it decreases in the case of thinner CCL. Again this is due to the better diffusion of oxygen in the thicker CCL than the thinner CCL as discussed previously. It also indicates that a strong interaction between two factors as here can actually completely change the behavior of the response. As in this case, the Pt loading has an opposite effect for cell voltage for different CCL thicknesses. This effect would be hard to discover by using the OFAT method.

5.2. DoE study



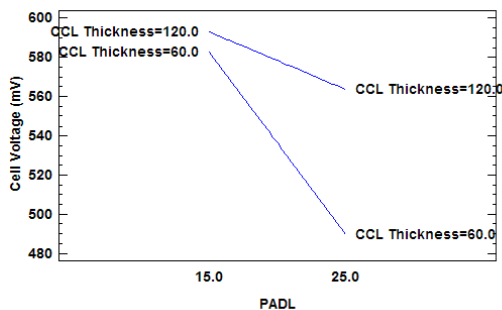
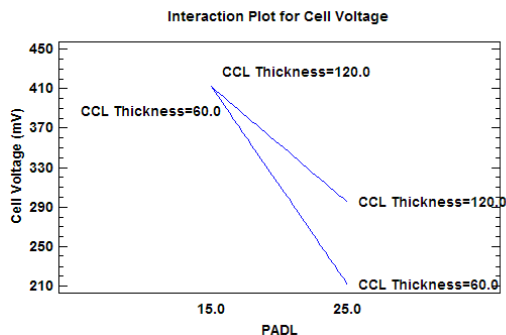
(a) Current density of 200mA cm^{-2}



(b) Current density of 600mA cm^{-2}

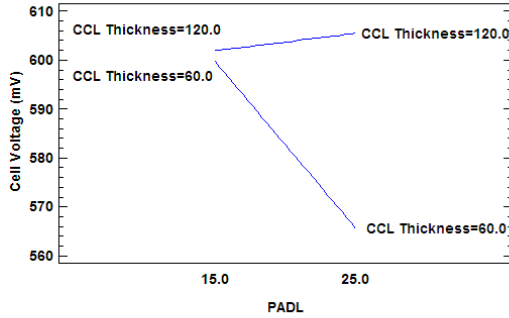
Figure 5.16: Pt loading and CCL thickness interaction (BC) comparison for anode/cathode λ of 2/6

The trends here are very similar to the low stoichiometry case.

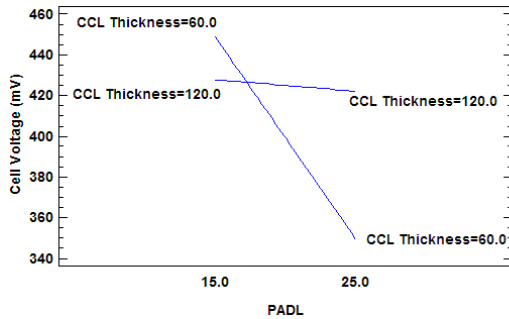
(a) Current density of 200 mA cm^{-2} (b) Current density of 600 mA cm^{-2} Figure 5.17: PADL and CCL thickness interaction (AC) comparison for anode/cathode λ of 2/2

Increasing the PADL affects the thinner CCL more severely. The physical reason for this is postulated as faster/more flooding of the thinner CCL pores in comparison to the thicker one. The PA is also known to adsorb on the Pt surface and thus affect the proton mobility in the CCL [154,155]. This would also be relevant in this case since the faster loss of cell voltage in the case of a thin CCL can be due to lower protonic conductivity in the CCL caused by the PA adsorption on Pt particle surfaces.

5.2. DoE study



(a) Current density of 200 mA cm^{-2}



(b) Current density of 600 mA cm^{-2}

Figure 5.18: PADL and CCL thickness interaction (AC) comparison for anode/cathode λ of 2/6

Increased PADL at higher cathode stoichiometry has very little effect on the thicker CCL (in fact, there is slight increase in cell performance for the 200 mA cm^{-2} case), but the thinner CCL cell still loses voltage as for the lower stoichiometry case, although the actual cell performance is better. The same reasoning as for the low stoichiometry case for the decreasing cell voltage with increasing PADL also applies here. As for the reduced voltage loss in case of the thicker CCL, this means that the higher stoichiometry improves cell performance. This is well known in the literature [32,35], but the improvement is much more pronounced for the thicker CCL because of lesser pore blockage and PA adsorption on the Pt particles, thus enhancing the TPB sites.

In the overall comparison of the desirability of the factors for the low stoichiometry case (see Figure 5.2, Figure 5.4 and Figure 5.6), it is obvious that the maximum desirability occurs for the

thicker CCL (120 μ m) with a PADL of 15mg cm⁻² and a Pt loading of 1mg cm⁻² for both current densities. Also, the PADL tolerance of the thicker CCL is much higher than its thinner counterpart. There is decrease in desirability by increasing the Pt loading for the thinner CCL and vice versa.

The desirability follows a similar pattern for the higher stoichiometry case (see Figure 5.8, Figure 5.10 and Figure 5.12) as for the lower stoichiometry case. There is still strong negative PADL effect for the thinner CCL, whereas the thicker CCL is more or less stable in this regard. The loss in desirability by increasing the Pt loading for the thinner CCL is much less pronounced but the increase in the thicker CCL is much more pronounced for a lower PADL while stable at the higher PADL. Since a higher PADL improves the protonic conductivity of the membrane and the CCL [156], the method of doping the membrane and the doping time can be improved to get better performing MEAs [52] as many high performing HT-PEFC MEAs have a high phosphoric acid content with specialized doping methods such as the sol-gel method of the Celtec® PW1100 BASF MEA.

The highest desirability is achieved for the factor settings of low PADL (15mg cm⁻²), high CCL thickness (120 μ m) and high Pt loading (1mg cm⁻²) for most cases. The corresponding MEA with these settings is MEA 7, which is therefore selected as the MEA with the most desirable factor settings, but still with further room for improvement, especially with regard to PA doping due to its high influence on cell performance.

5.3 EIS study

The EIS study is done as a supplement to the DoE study to verify the findings and also investigate the important electrochemical parameters of the cell to have a clearer picture of the dominant parameters affecting cell performance. This will help to pinpoint improvement areas and determine the methodology to implement those improvements to have better performing PBI based HT-PEFC MEAs in future.

5.3.1 Experimental

All the MEAs are subjected to EIS measurements immediately after the break-in procedure is finished and the UI curves have been taken. The aim is to characterize the CCL and determine its most important electrochemical parameters. This can be achieved by measuring the cell impedance at very low current densities (typically upto 100mA cm⁻²) and a high cathode stoichiometry (minimum 10) to ensure very high and constant oxygen concentration throughout the catalyst layer. This ensures almost no contribution to the mass transport losses from the lack of oxygen diffusion to the TPB at the membrane/CCL interface and instead all the resistance shown by the cell in the low frequency region of the Nyquist plot can be attributed exclusively to the CCL itself [123,151,157]. The relevant electrochemical parameters of the CCL can therefore be extracted by fitting a simple ECM to the impedance data [158,159].

Four current densities are selected for impedance measurements, 10, 20, 50 and 100mA cm⁻² respectively. The aim is to observe the variation in the electrochemical parameters of the cell

5.3. EIS study

with increasing current density in the low current density regime, since they are known to be a function of current density [160].

The actual flowrate of the gases on the anode and cathode side respectively is kept constant at the values of a 2/6 stoichiometry for a current density of 200mA cm^{-2} . This means that the actual stoichiometries for the impedance measurements are much higher as shown in Table 5.7.

Table 5.7: Stoichiometries of the anode and cathode sides for the impedance measurements

Current density (mA cm^{-2})	Anode/cathode stoichiometry (λ) for impedance measurements
10	40/120
20	20/60
50	8/24
100	4/12

The high values of the cathode λ (minimum value is 12 for the highest current density) ensure that the reference concentration of oxygen in the CCL can safely be assumed as constant.

The ECM for cell operation at low current density ($<100\text{mA cm}^{-2}$) and high cathode stoichiometry (> 10) is used for fitting the impedance data as given and explained in Figure 2.8. The inductive element models the cable noise and inductance, the first resistance R_0 models the ohmic resistance R_Ω of the cell (left intercept on the Nyquist plot), the porous electrode models the protonic resistance of the CCL R_p , the resistance R_1 models the activation resistance R_{act} of the ORR (taking place in the CCL) and the constant phase element (CPE) models the double layer capacitance C_{dl} of the membrane electrode interface.

The Nyquist plots for the selected current densities are fitted with the ECM presented above by using the THALES software and the corresponding resistances and double layer capacitances are then determined. The overall DC resistance R_{dc} (which is the right intercept of the Nyquist plot) is determined by summing up all the resistances.

5.3.2 Results

The UI curves taken immediately after the break-in procedure for each MEA are compared in Figure 5.19. It is seen that MEAs 3, 5, 6 and 7 seem to have better performance. All of these MEAs lie in the same range.

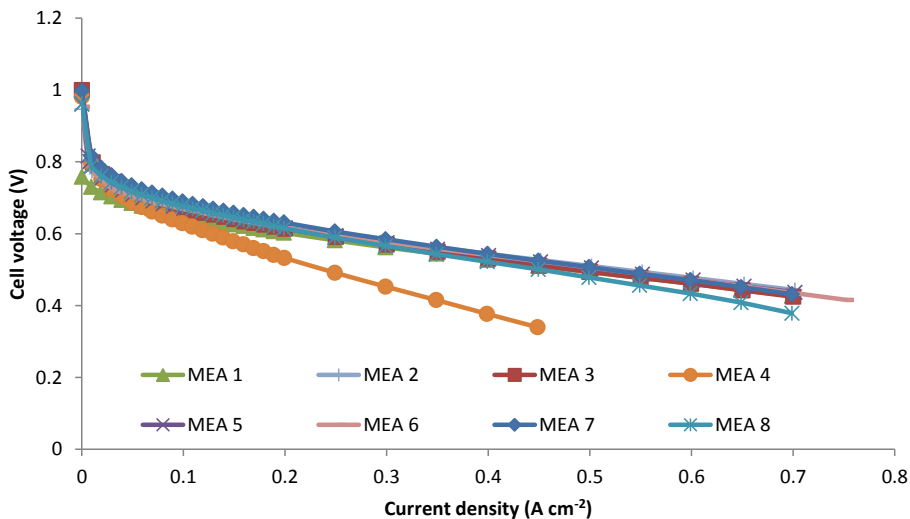


Figure 5.19: UI Curve comparison for all the MEAs immediately after the break-in procedure, operating conditions: λ (An (H_2)/Ca (Air)) = 2/6 for current densities higher than 200mA cm^{-2} (below 200mA cm^{-2} , the gas flowrate for $\lambda = 2/6$ at 200mA cm^{-2} is maintained) $T = 160^\circ\text{C}$ (See Table 5.2 for MEA specifications)

The Nyquist plots for all the MEAs are recorded for the four selected current densities of 10, 20, 50 and 100mA cm^{-2} . The Nyquist plot for MEA7 is shown in Figure 5.20 below as an example.

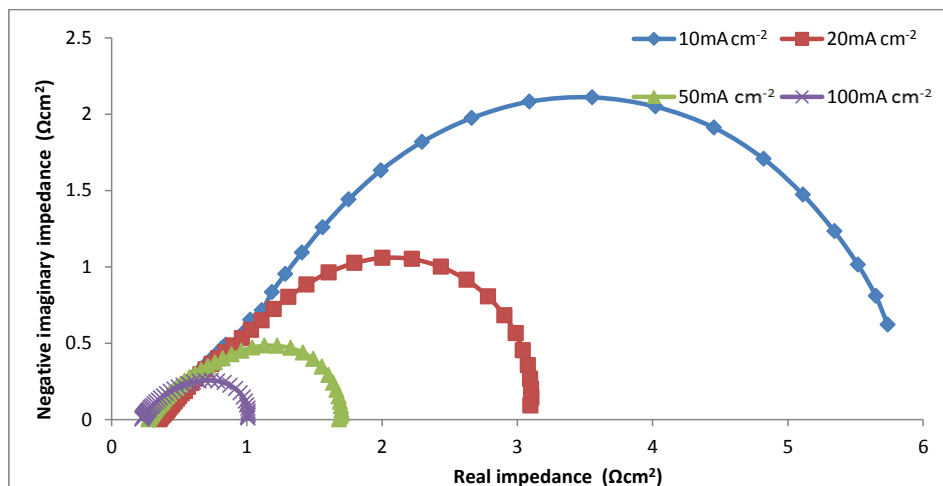


Figure 5.20: Nyquist plot of MEA7 for the selected current densities and stoichiometries as shown in Table 5.7.

5.3. EIS study

The ohmic resistance (R_{Ω}), protonic resistance (R_p), activation resistance (R_{act}) and double layer capacitance (C_{dl}) of all the eight MEAs are calculated by fitting the data of the Nyquist plots with the ECM mentioned above. A comparison of these values for all the MEAs is presented and discussed next.

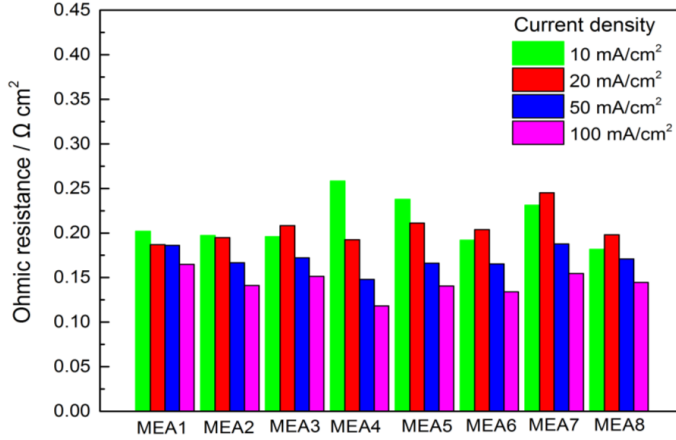


Figure 5.21: Ohmic resistance (R_{Ω}) values of all MEAs from ECM fitting of EIS data

The ohmic resistances for all the MEAs are presented in Figure 5.21. Since the ohmic resistance is dominated by the membrane resistance [161], we expect it to go down with current density due to production of more water at higher current densities and the conversion of less conductive pyrophosphoric acid to the more conductive orthophosphoric acid by hydration [159,162] in accordance with Eqn. (5.1);



The ohmic resistance does indeed follow this trend with the exception of the first step (from 10 to 20 mA cm⁻²) in some cases. This is due to the lack of sufficient water vapour accumulation in the membrane and the CCL at these very small current densities and very high cathode stoichiometries (see Table 5.7). The high cathode stoichiometry causes blowing out of the tiny amount of water vapour produced. The ohmic resistance decreases nevertheless for most MEAs and reaches values between 0.012 and 0.015 Ω cm², where it should stabilize as the transition from the activation region to the ohmic region is completed. Another point of interest is the fact that ohmic resistances for even numbered MEAs are comparable to those of odd numbered despite the fact that even numbered MEAs have additional PA content (25 vs 15 mg cm⁻² for odd numbered MEAs) showing that not much of the additional PA added onto the GDEs actually made its way to the membranes else the ohmic resistance should be notably lower. There doesn't seem to be a trend for high Pt loading MEAs (1, 2, 5, 6) vs. low Pt loading MEAs (3, 4, 7, 8).

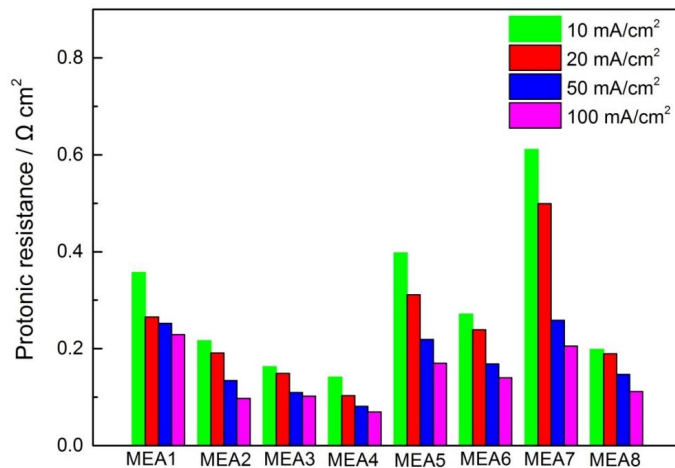


Figure 5.22: Protonic resistance (R_p) values of all MEAs from ECM fitting of EIS data

As discussed previously, R_p , the protonic resistance of the CCL shows the resistance to proton transport in the CCL and it has a decreasing trend for increasing current density in all the MEAs as shown in Figure 5.22. Since R_p depends mainly on the amount of PA in the CCL, even numbered MEAs do indeed have lower values than odd numbered MEAs. MEA 7 has the highest R_p values at most current densities, indicating room for improvement in this regard, since all other parameters for this MEA are very promising. There is a greater drop in MEAs 5-8 (thick MEAs) of R_p values as compared to MEAs 1-4 (thin MEAs). However, the final R_p values for 100 mA cm⁻² are comparable (around 0.1 Ω cm² with the exception of MEA 1 and 7 which are close to 0.2 Ω cm²). It has to do with water vapor production and blowing out of the vapor as described in the case of ohmic resistance since the thinner MEA is more susceptible to PA flooding and blowout. Again, there is no trend for high Pt loading MEAs (1, 2, 5, 6) vs. low Pt loading MEAs (3, 4, 7, 8).

5.3. EIS study

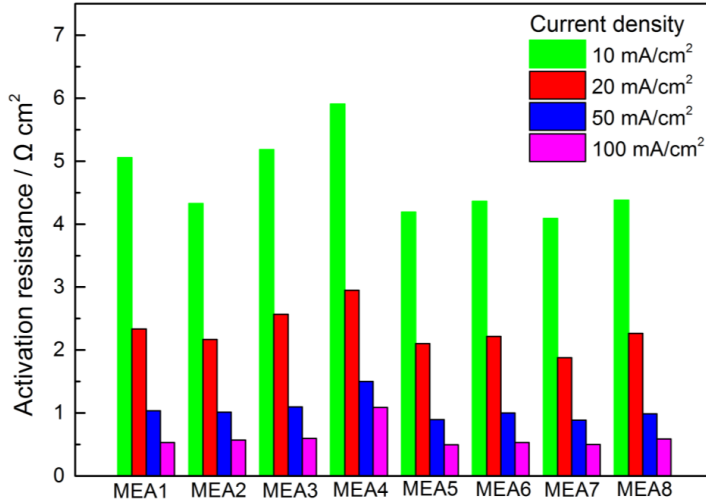


Figure 5.23: Activation resistance (R_{act}) values of all MEAs from ECM fitting of EIS data

The activation resistance dominates the fuel cell losses in the activation region as can be seen in Figure 5.23. The activation resistance decreases exponentially with current density as predicted by the Butler - Volmer relationship. The physical reason for this is the increased water vapor content at higher current densities increasing the oxygen solubility in the PA and water mixture, which in turn increase the oxygen concentration and the exchange current density. This reduces the activation resistance with increasing current density.

It should be noted that the R_{Ω} and R_p values are of the same order of magnitude but the dominant resistance at these conditions is the activation resistance which is at least an order of magnitude higher than both at all current densities. Therefore, this is the single most important parameter for deciding the best in the range of current density investigated. It can be seen that the high PADL MEAs (even numbered) have considerably larger activation resistances than the low PADL (odd numbered) with the exception of MEA1 at 10 mA cm^{-2} . Also the thinner MEAs (1-4) have much higher activation resistances than the thicker ones (5-8). MEA 7 has the lowest activation resistances for all current densities.

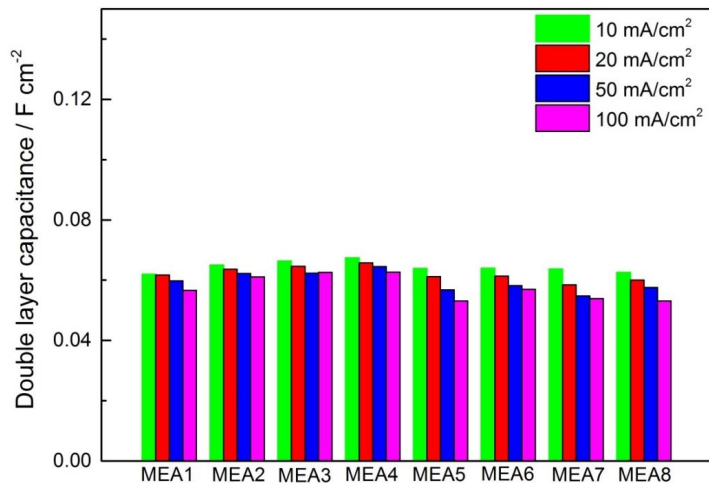


Figure 5.24: Double layer capacitance (C_{dl}) values of all MEAs from ECM fitting of EIS data

Figure 5.24 shows the double layer capacitance (C_{dl}) of all the MEAs. Larger C_{dl} values can be generally attributed to larger electrochemical surface area (ECSA) [163]. The slightly decreasing trend for all the MEAs is explained by the change of the wetting angle between PA and the Pt particles and the carbon support due to additional water production since it leads to change in the concentrations of the PA species present in the MEA. The wetting angle is affected by change in the concentration of PA as determined by Mack et al. [164]. The actual values for all the MEAs are in the same range from 0.06 F cm^{-2} for 10 mA cm^{-2} to around 0.055 F cm^{-2} for 100 mA cm^{-2} . The decrease in the thicker MEAs (5-8) is slightly more pronounced as compared to the thinner ones (MEA 1-4), arguably, due to different wetting angles between PA and the catalyst due to the difference in PA and water vapor distribution in the MEAs with different thicknesses. No other trends are observed.

5.4. Summary

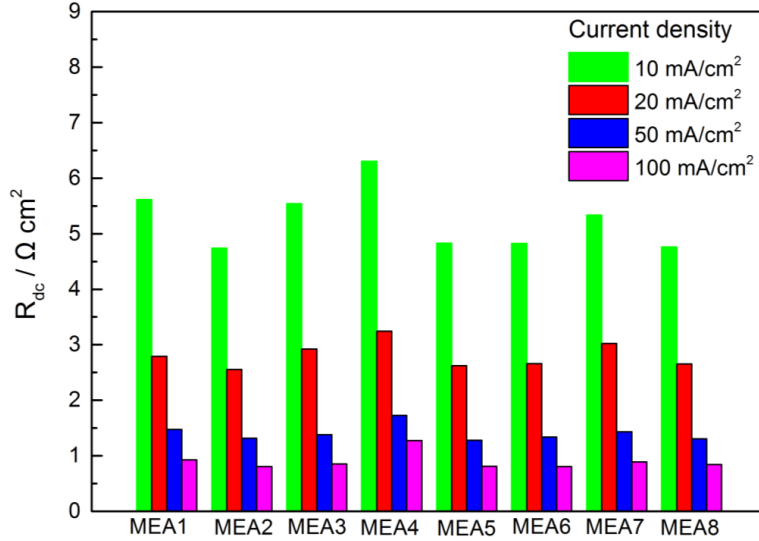


Figure 5.25: Total DC resistance (R_{dc}) values of all MEAs from ECM fitting of EIS data

The DC resistance is the sum of all characteristic resistances and the right intercept of the Nyquist plot. As seen in Figure 5.25, the thicker MEAs (5-8) have a much lower DC resistance than the thinner ones (1-4).

As seen from the UI curves (Figure 5.19), the activation resistance (Figure 5.23) and the DC resistance comparisons (Figure 5.25), the thicker MEAs generally have lower R_{dc} values. The magnitudes of ohmic and protonic resistances are comparable to each other but an order of magnitude lower than the activation resistance. The double layer capacitance comparison shows that the ECSA for all MEAs is comparable. The DoE study also showed that a lower PADL and higher CCL thickness and Pt loading are more desirable for best cell performance. MEA7 has the lowest activation resistances while other values are comparable. Therefore it is selected as the best performing MEA and MEA5 is a close second with potential for further testing and improvement.

5.4 Summary

A study of the in-house assembled MEAs is undertaken with the aim of studying the effects of PADL, CCL thickness and Pt loading on single cell performance. Eight different MEAs are assembled and tested with an experimental plan made by the DoE method. All the MEAs are also subjected to EIS testing in the low current density regime to characterize the CCL. Results from both studies indicate that a lower PADL and higher CCL thickness and Pt loading are best for cell performance.

6 Effects of Anode and Cathode Gas Concentration on Cell Impedance

The effects of changing the concentration of the anode and cathode side gases on the cell impedance are studied in a systematic manner in this chapter. This is done not only from a CCL characterization view point, but also in an effort to improve the CCL performance by pinpointing the problem areas indicated by the characteristic cell resistances determined from the cell impedance. The EIS data is analyzed with a conventional ECM and a literature based 1D analytical model for a comparison and discussion. An improved ECM is suggested for the operating conditions investigated to extract the value of mass transport resistance of the CCL based on the effective diffusion coefficient of oxygen in the CCL as a fitting parameter.

6.1 Experimental

An experimental plan is devised to vary the gas concentration on the anode and cathode sides separately; the gas concentration is fixed on the other side. It is done to extract in depth information of the effects on cell performance, particularly, the cell impedance. Table 6.1 lists the concentrations of the gases used on the anode and cathode sides. When varying the anode gas concentration, both air and pure oxygen is used for all anode gas concentrations. Pure hydrogen is used as the anode gas when varying the cathode gas concentration.

Table 6.1: Different gas concentrations used for the anode and cathode side

H₂ %age (by volume) in Anode Gas (Rest is N₂)	O₂ %age (by volume) in Cathode Gas (Rest is N₂)
5	5
20	21 (Air)
40	40
60	60
80	80
100	100

6.2. UI curves and Nyquist plots

MEA, break-in and operating conditions

The in house assembled MEA with a PADL of 15mg cm^{-2} , CCL thickness of $120\mu\text{m}$ and a Pt loading of 1mg cm^{-2} is used for assembling the single cells for all the experiments. This is the MEA7 from chapter 5, which was determined to be the best performing MEA.

The standard 17.64cm^2 cell is used for all the experiments and the standard break-in procedure (See section 3.1.1) is run on all cells before any testing is done. After the break-in, three UI curves are performed with an anode/cathode stoichiometry of 2/6 (gas flowrates are kept constant below 200mA cm^{-2} at the values of a stoichiometry of 2/6 for a current density of 200mA cm^{-2}) and an operating temperature of 160°C . Twenty points are measured in the activation region (below 200mA cm^{-2}) for each curve with a step size of 10mA cm^{-2} . Then two impedance measurements are taken for each combination of anode/cathode gas compositions with current densities of 50 and 100mA cm^{-2} and stoichiometries of 8/24 and 4/12 respectively (due to fixed gas flowrates below 200mA cm^{-2}). This ensures practically constant concentration of oxygen throughout the CCL and allows interpreting the impedance data collected to be mainly relevant to the CCL electrochemical parameters.

6.2 UI curves and Nyquist plots

The UI curves presented below reflect averaged values from three measurements. The Nyquist plots are single measurements for each current density.

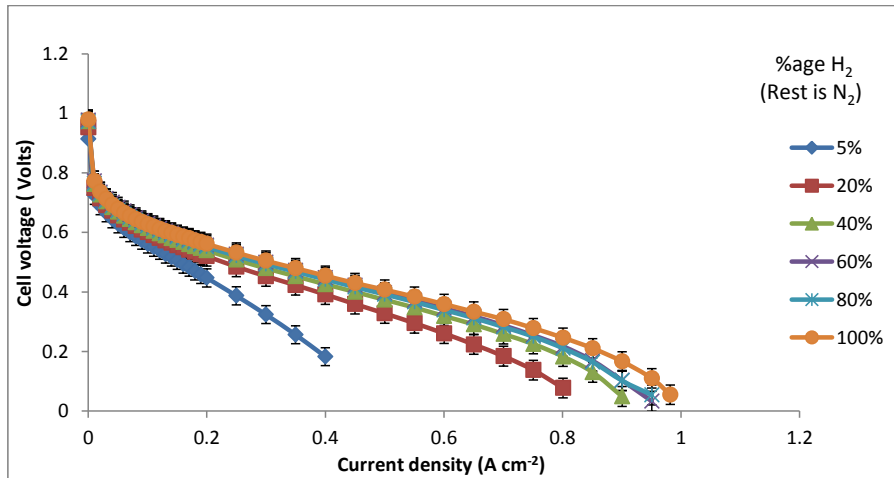


Figure 6.1: UI curves for single cell with varying hydrogen concentration on the anode side, cathode gas: air, anode/cathode $\lambda = 2/6$, $T = 160^\circ\text{C}$

6. Effects of Anode and Cathode Gas Concentration on Cell Impedance

It can be seen from Figure 6.1 that increasing hydrogen concentration in the fuel stream has a significantly positive effect on the fuel cell performance. This is very much pronounced for the cases of 5 and 20% H_2 , but also in the other four cases the cell performance increases steadily before reaching the peak values for 100% H_2 . This is explained by the fact that for a lower percentage of H_2 in the anode feed, there is a lower partial pressure of H_2 . Since the activity of a reactant is proportional to its partial pressure in case of an ideal gas [165], there is a decrease in the Nernst voltage of the fuel cell. Also, there is a strong gradient of the concentration of H_2 along the channels for lower concentrations of H_2 , whereas the reactant concentration is practically constant in the case of higher percentages of H_2 . It can be seen that for the cases of 5 and 20% H_2 there is a lower performance even in the activation region and the ranges of the UI curves are significantly shorter.

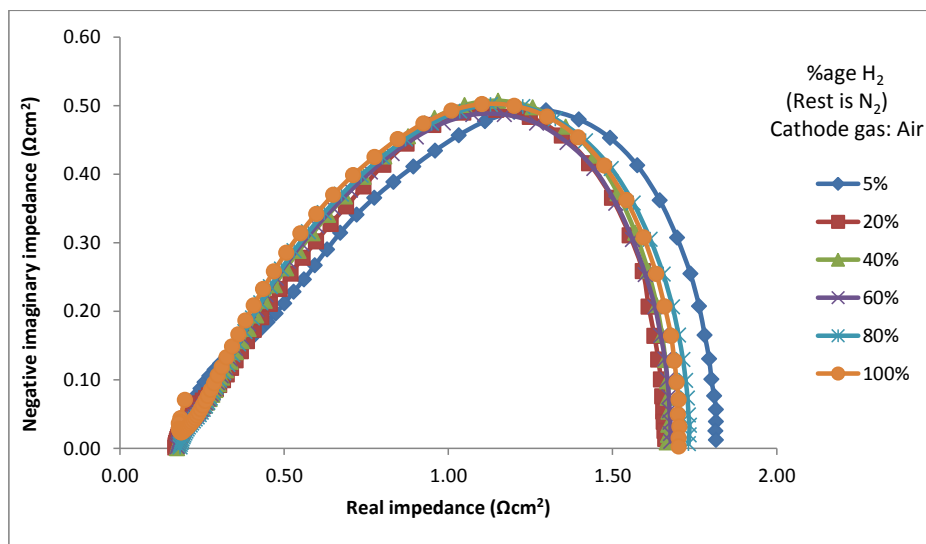


Figure 6.2: Nyquist plots for different anode gas concentrations for 50mA cm^{-2} anode/cathode $\lambda = 8/24$, $T = 160^\circ\text{C}$

6.2. UI curves and Nyquist plots

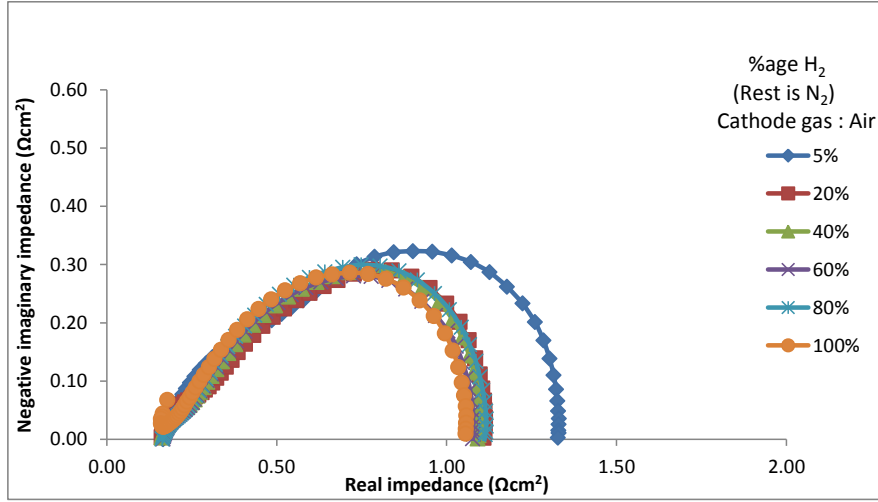


Figure 6.3: : Nyquist plots for different anode gas concentrations for 100mA cm⁻² anode/cathode $\lambda = 4/12$, $T = 160^\circ\text{C}$

The Nyquist plots presented in Figure 6.2 and Figure 6.3 for the cell impedance at 50 and 100mA cm⁻² respectively show that there is little effect on cell impedance of the changing H₂ concentration except for the case of 5% H₂. In the case of 50mA cm⁻², even that is not too high, but in the case of 100mA cm⁻², it is significant (about 0.3Ω cm² higher than the other curves). Since with pure hydrogen operation, the fuel cell impedance is mainly attributed to the cathode impedance [124], this result is expected. In the case of 5% H₂, the concentration gradient along the channel causes the higher impedance at higher current densities as mentioned before and observed here in the case of 100mA cm⁻². The cases with higher percentages of H₂, have almost identical impedance spectra.

6. Effects of Anode and Cathode Gas Concentration on Cell Impedance

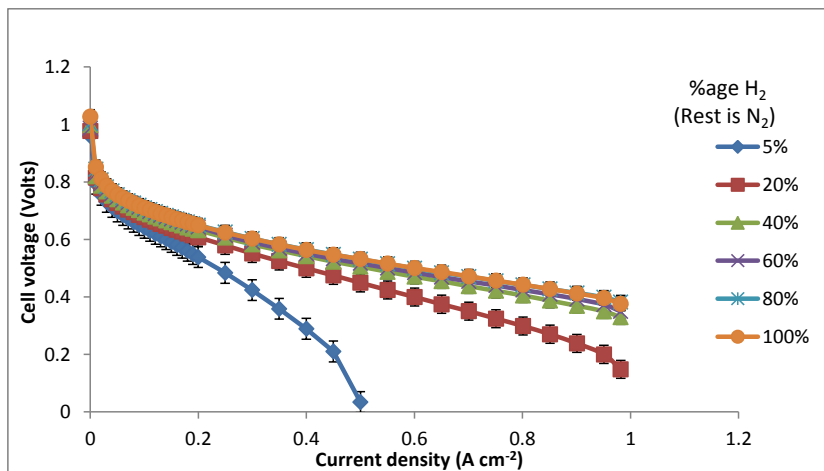


Figure 6.4: UI curves for single cell with varying hydrogen concentration on the anode side, cathode gas: oxygen, anode/cathode $\lambda = 2/6$, $T = 160^\circ\text{C}$

Figure 6.4 shows the UI curves for changing H_2 concentration, but with pure O_2 used as the cathode gas instead of air. The trend here is similar to the case with air, although the overall performance and range of the cell is much better when compared to the air case. The obvious cause is the higher O_2 concentration. It should be noted however, that even in this case the polarization curves for 5 and 20% H_2 are still the worse, although improved from the air case.

Figure 6.5 and Figure 6.6 show the Nyquist plots for the two selected current densities. It can be seen that the overall resistance (also called the DC resistance) which is the right intercept of the x-axis on the Nyquist plot is considerably lower from the case with air on the cathode side. There is still a considerable increase in the DC resistance for the case of 5% H_2 .

6.2. UI curves and Nyquist plots

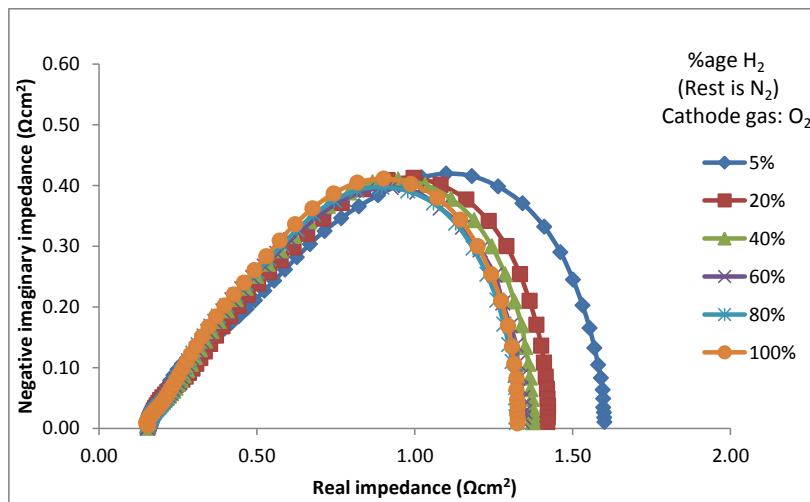


Figure 6.5: Nyquist plots for different anode gas concentrations for 50mA cm^{-2} anode/cathode $\lambda = 8/24$, $T = 160^\circ\text{C}$

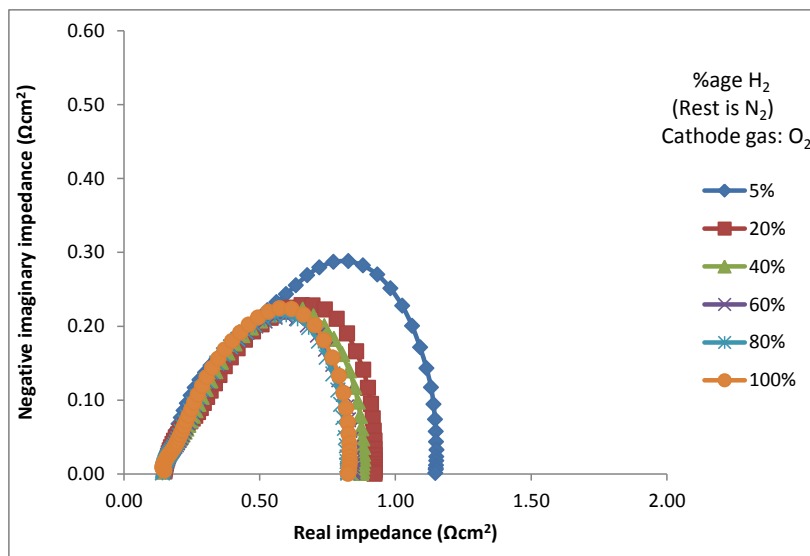


Figure 6.6: Nyquist plots for different anode gas concentrations for 100mA cm^{-2} anode/cathode $\lambda = 4/12$, $T = 160^\circ\text{C}$

6. Effects of Anode and Cathode Gas Concentration on Cell Impedance

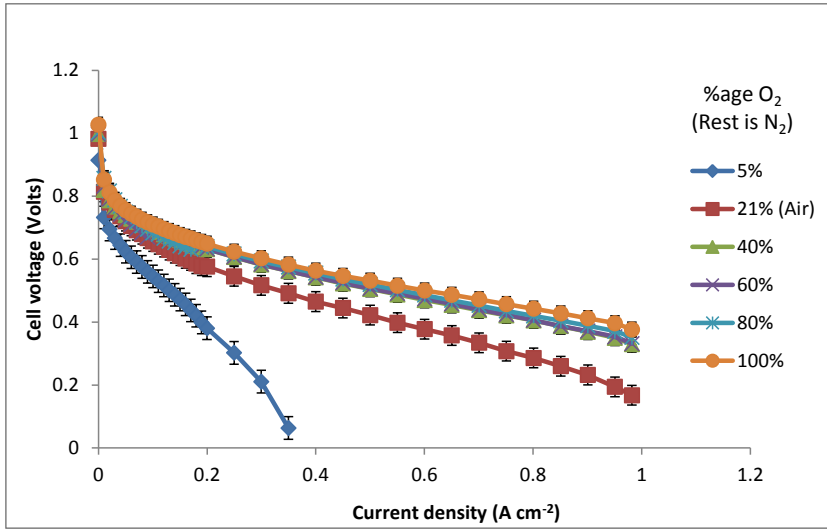


Figure 6.7: UI curves for single cell with varying oxygen concentration on the cathode side, Anode gas: hydrogen, anode/cathode $\lambda = 2/6$, $T = 160^\circ\text{C}$

Figure 6.7 gives the UI curves for different O_2 concentrations with the anode gas fixed as H_2 . It is evident that O_2 percentages of 5 and 20% are the worst for cell operation whereas there is much slower improvement in cell performance at higher O_2 percentages. The effect of gas concentration here is much higher than in the case of H_2 concentration change due to the fact that O_2 concentration affects the ORR, whose exchange current density is much smaller than that of the HOR [65]. The UI curve at 5% oxygen is especially interesting when compared to the curve with a H_2 concentration of 5%. The limiting current density seems to be reached much earlier in this case (about 0.5 A cm^{-2} in case of 5% H_2 but less than 0.4 A cm^{-2} here).

Figure 6.8 and Figure 6.9 show the Nyquist plots for changing O_2 concentration for the current densities of 50 and 100 mA cm^{-2} respectively. It is observed that the impedance in the case of the lower two O_2 concentrations (5 and 20%) is much higher than for the other four cases. This signifies the point that a lower O_2 concentration increases the cell impedance (thus reducing performance) even at very high cathode stoichiometries (12 and 24 in this case respectively). The Nernst equation and the O_2 concentration along the channel provide the theoretical explanations for this just as in the case of H_2 concentration change. A third reason here is the cathode side reaction kinetics, which is more sensitive to reactant molar concentration than the H_2 case due to a much lower exchange current density.

6.2. UI curves and Nyquist plots

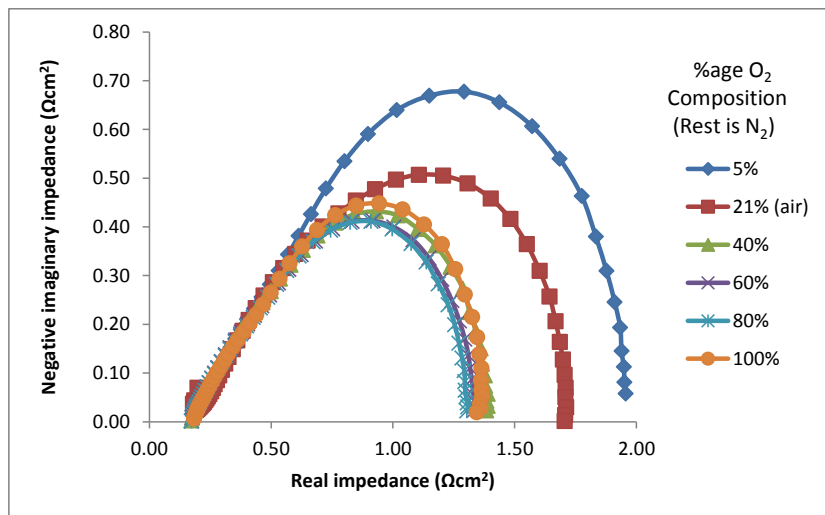


Figure 6.8: Nyquist plots for different cathode gas concentration for 50mA cm^{-2} anode/cathode $\lambda = 8/24$, $T = 160^\circ\text{C}$

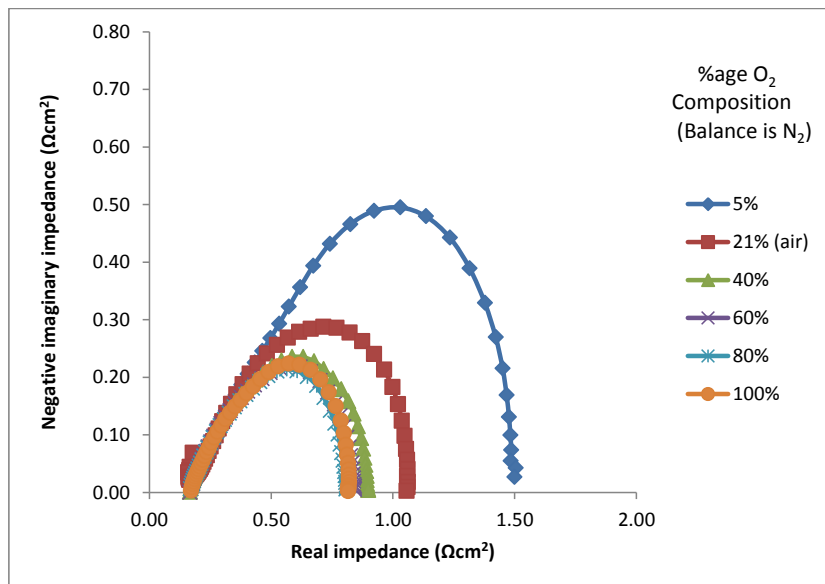


Figure 6.9: Nyquist plots for different cathode gas concentration for 100mA cm^{-2} anode/cathode $\lambda = 4/12$, $T = 160^\circ\text{C}$

6.3 Comparison of fitting results

The impedance data shown in the previous section for different gas concentrations in the form of Nyquist plots is analyzed with the classical ECM called the transmission line model for low current density and high cathode stoichiometry as well as the one dimensional analytical model valid for low current densities by Kulikovsky [83,166,167] (See section 2.2.3 for detailed description). The aim is to compare the ECM with the analytical model and determine the characteristic CCL resistivities for comparison.

There are three parameters that can be directly compared from both models; the protonic resistance (R_p), the activation resistance (R_{act}) and the volumetric double layer capacitance (C_{dl}). The ohmic resistance R_Ω is determined explicitly only by the ECM and the mass transport resistance of the CCL R_{exp} is determined only by the AM. The overall DC resistance (sum of all resistivities or the right intercept of the Nyquist plot) can also be compared. Below, we compare and discuss these parameters for the three different cases of gas concentrations. Firstly H_2 concentration change with air on the cathode side, then H_2 concentration change with pure O_2 on the cathode side and finally O_2 concentration change with pure H_2 on the anode side.

6.3.1 Hydrogen concentration change with air on the cathode side

Figure 6.10 through Figure 6.15 show the comparison of the calculated cell parameters for both investigated current densities. The discussion is presented one by one below each figure.

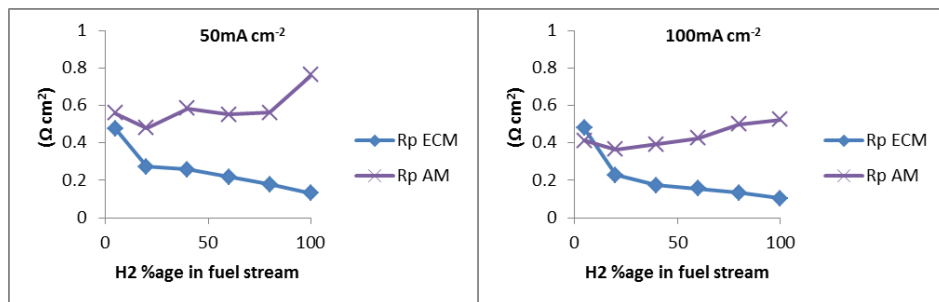


Figure 6.10: Comparison of R_p for increasing hydrogen content in the fuel stream, anode/cathode $\lambda = 8/24$ (left) and $4/12$ (right), $T = 160^\circ\text{C}$

The R_p values predicted by the ECM and the AM agree at the lowest H_2 percentage (5%) well, but then their paths diverge (Figure 6.10). The AM value has an increasing trend whereas the ECM value has a decreasing trend. Since the CCL protonic conductivity depends not only on the amount of PA in the CCL, but also on the solubility of O_2 in the PA and water vapor mixture [36] the overall effect is not that straight forward. In the case of increasing H_2 %age in the fuel stream, it can be argued that it should not affect the CCL protonic conductivity dramatically as H_2 concentration has no direct effect on this. This result is unexpected not only from a trend point of view (decreasing in the case of ECM,

6.3. Comparison of fitting results

whereas constant or increasing in case of AM) but also the great difference in magnitude of the calculated R_p , the value calculated by AM being many times higher than the ECM value. The only thing that can be said is that the ECM and AM R_p values differ quite significantly as the AM R_p values are higher than the ECM values by a factor of 2 or more for all H_2 percentages higher than 5%.

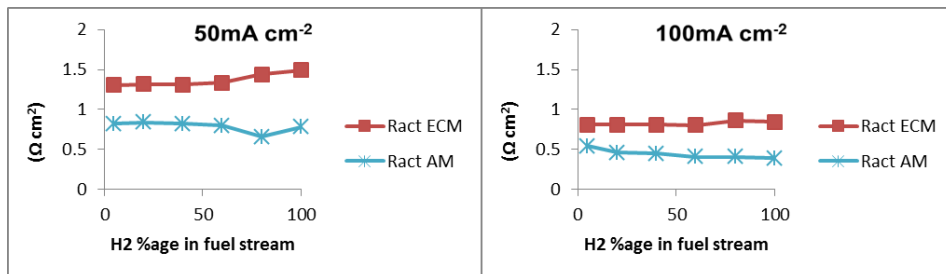


Figure 6.11: Comparison of R_{act} for increasing hydrogen content in the fuel stream, anode/cathode $\lambda = 8/24$ (left) and $4/12$ (right), $T = 160^\circ\text{C}$

The activation resistance trend is consistent and relatively independent of the H_2 %age in the fuel stream due (Figure 6.11) to dominant cathode side charge transfer overpotential [168] but the ECM value is consistently higher than the AM values for all H_2 percentages. The AM value uses actual physical parameters (Tafel slope b and current density j_0 as per Eqn. (2.7)). Whereas the ECM value is just a resistance value fit to the impedance data. The ECM value is higher by about $0.3\text{--}0.4 \Omega \text{ cm}^2$ for all data points than the respective AM values. The R_p values of the ECM are less by about the same amount from the AM values (Figure 6.10). It seems that the ECM mixes up the magnitudes of some of the resistances (R_p and R_{act} in this case) as the total DC resistance must add up to the same value for a good fit since the right intercept of the Nyquist plot is the same. A possibility to verify this is to use pure oxygen on the cathode side to isolate the effect of H_2 . This is done in section 6.3.2.

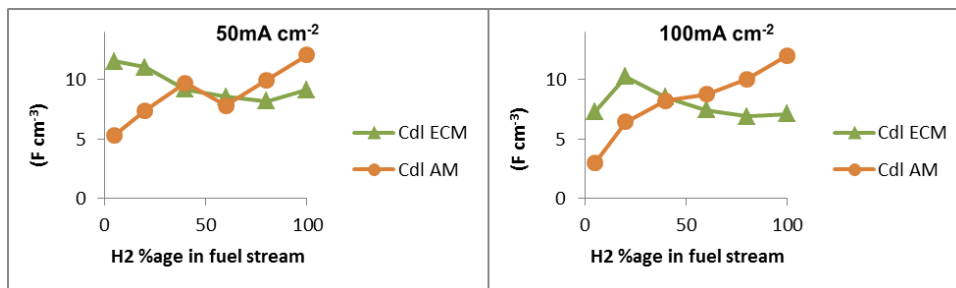


Figure 6.12: Comparison of C_{dl} for increasing hydrogen content in the fuel stream, anode/cathode $\lambda = 8/24$ (left) and $4/12$ (right), $T = 160^\circ\text{C}$

Although the C_{dl} values differ in magnitude by a factor of 2 for the lowest H_2 percentage, the values for 40 and 60% H_2 are much closer (Figure 6.12). The agreement in values of C_{dl} diverges

again for the higher H_2 %ages. The best agreement is obtained at the H_2 percentages of 40 and 60%. For 80 and 100% H_2 the AM values are higher than the ECM values and for 5 and 20% H_2 they are lower than the corresponding ECM values. A higher C_{dl} generally indicates a higher ECSA [158]. This implies constant or slightly increasing electrochemically active area with increasing H_2 percentage in the fuel stream for the AM values. The ECM values are higher at lower H_2 %ages (5 and 20) and lower at higher H_2 %ages (80 and 100). Higher H_2 percentage in the fuel stream enhances the charge accumulation along the porous double layer in the electrode and we expect the C_{dl} to change slightly with increasing current density due to subtle changes in the wetting angle between PA and the Pt catalyst particles and the carbon support caused by the addition of a dipole (water) to the PA [151,164]. This is what is seen in this case. However, since the ECM shows a decreasing trend for C_{dl} values and the AM shows an increasing trend, it is hard to conclude something concrete on the evidence available.

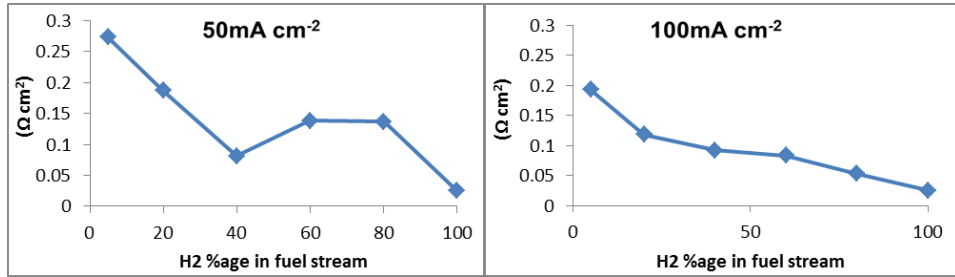


Figure 6.13: R_{oxp} (as calculated by AM) with increasing hydrogen content in the fuel stream, anode/cathode $\lambda = 8/24$ (left) and $4/12$ (right), $T = 160^\circ\text{C}$

R_{oxp} , the mass transport resistance of the CCL is a parameter that is only calculated by the AM. R_{oxp} is determined analytically by the AM only and the trends are shown in Figure 6.13. R_{oxp} depends on the diffusion coefficient of O_2 in the CCL which depends on the amount of water vapor and PA inside the CCL and the solubility of O_2 in it, among other factors [36]. It can be seen that it has a decreasing trend for both current densities. It means that H_2 %age in the fuel stream does have some indirect effect on this parameter perhaps due to the permeation of H_2 through the membrane for additional water formation at higher H_2 %ages, thus reducing the resistance to oxygen transport in the CCL.

6.3. Comparison of fitting results

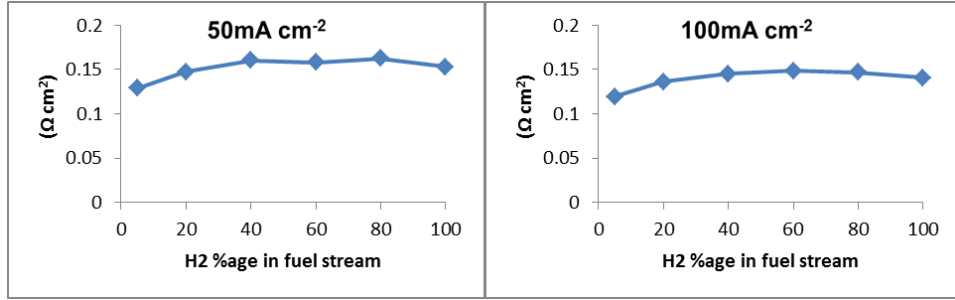


Figure 6.14: R_{Ω} as calculated by ECM with increasing hydrogen content in the fuel stream, anode/cathode $\lambda = 8/24$ (left) and $4/12$ (right), $T = 160^{\circ}\text{C}$

The ohmic resistance R_{Ω} is only calculated by the ECM but it is easy to determine as it is the left intercept of the Nyquist plot and as seen in Figure 6.14, it is relatively constant for all H_2 %ages. This is expected as the ohmic resistance is mainly due to the membrane resistance and the contact resistance [135,168] which are expected to remain more or less constant because the PADL is the same for all the membranes and the same cell materials are used. The value around $0.15 \Omega \text{ cm}^2$ is also typical for HT-PEFC single cells with PBI based membranes [169].

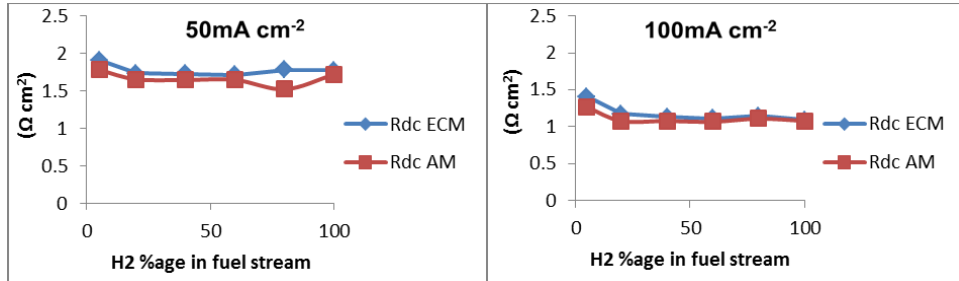


Figure 6.15: Comparison of R_{dc} for increasing hydrogen content in the fuel stream, anode/cathode $\lambda = 8/24$ (left) and $4/12$ (right), $T = 160^{\circ}\text{C}$

Finally, we compare the DC (total) resistances at the selected current densities. It is seen in Figure 6.15 that the DC resistances match very well, but more so at the current density of 100 mA cm^{-2} . This must be so as the same Nyquist plot is used by both models to calculate the parameters. The only differences are in the magnitudes of the resistances.

6.3.2 Hydrogen concentration change with oxygen on the cathode side

In this section, again the effect of H_2 on cell impedance is analyzed, but with a vital difference. O_2 is now used as the cathode gas instead of air, which should in theory clarify the effect of H_2 %age only in the fuel stream on cell impedance as the cathode side operating conditions are practically the best which can be achieved (i.e. high stoichiometry, pure oxygen and low current density). The results are shown in Figure 6.16 through Figure 6.21.

6. Effects of Anode and Cathode Gas Concentration on Cell Impedance

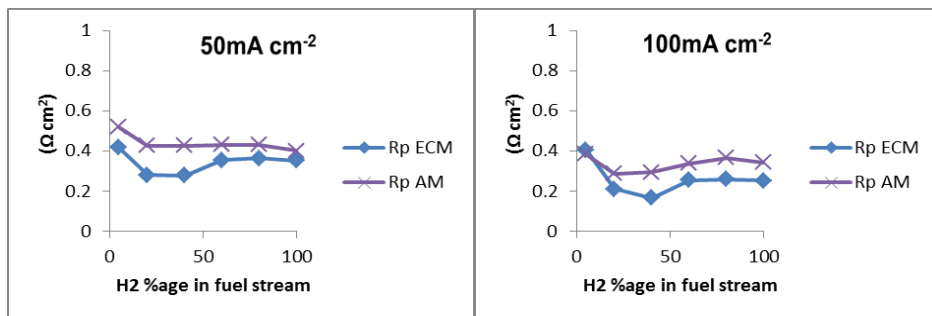


Figure 6.16: Comparison of R_p for increasing hydrogen content in the fuel stream (O_2 on cathode side), anode/cathode $\lambda = 8/24$ (left) and $4/12$ (right), $T = 160^\circ\text{C}$

Although there is still a small difference in the R_p values for the ECM and the AM, the trends are similar and the R_p value remains essentially constant for the H_2 %ages of 40 and more (Figure 6.16). This fits with the fact that R_p should not be affected too much by changing H_2 concentration in the fuel stream, since it represents the CCL protonic resistance. However, the AM values are still slightly higher than the ECM values as observed in Figure 6.10. This indicates that the porous electrode used for fitting the R_p value from the ECM is not the ideal choice since the AM uses fitted values of the protonic conductivity of the CCL which ranges between 0.007 ($5\% \text{ H}_2$) and 0.012 S cm^{-1} ($100\% \text{ H}_2$), which fits well with literature values [170].

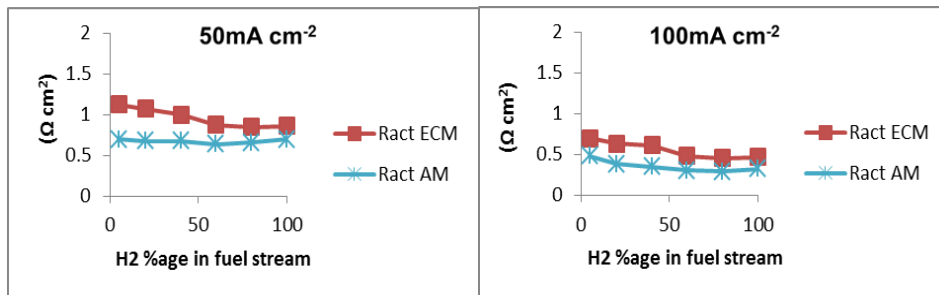


Figure 6.17: Comparison of R_{act} for increasing hydrogen content in the fuel stream (O_2 on cathode side), anode/cathode $\lambda = 8/24$ (left) and $4/12$ (right), $T = 160^\circ\text{C}$

The activation resistance does not show much dependence on the H_2 concentration as discussed before, but the ECM values are again slightly higher as in the case of air on the cathode side (Figure 6.17). This compensates for the lower R_p value calculated by the ECM since the DC resistance must always be the same (as the same Nyquist plot is fitted by both models)

6.3. Comparison of fitting results

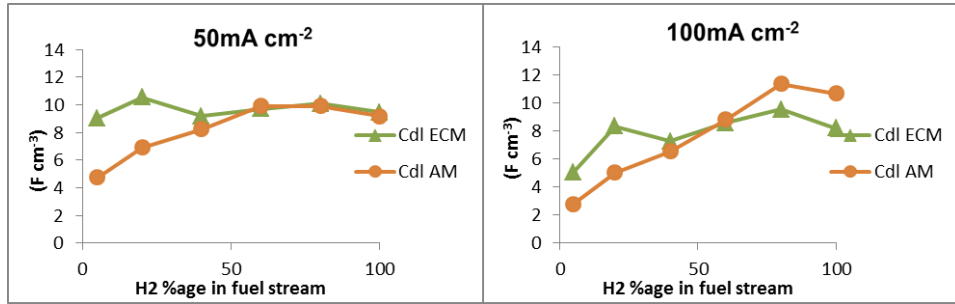


Figure 6.18: Comparison of C_{dl} for increasing hydrogen content in the fuel stream (O_2 on cathode side), anode/cathode $\lambda = 8/24$ (left) and $4/12$ (right), $T = 160^\circ\text{C}$

The double layer capacitance follows similar trends as in the case of air on the cathode side (see Figure 6.12), as depicted in Figure 6.18 above. The agreement between the ECM and AM values for the case of 50mA cm^{-2} is much better for H_2 %ages of 60, 80 and 100 respectively.

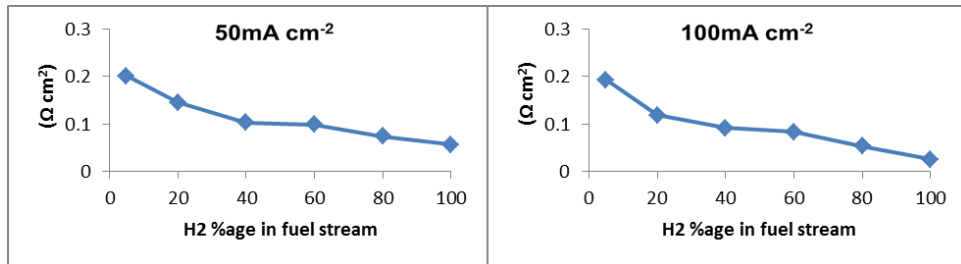


Figure 6.19: R_{oxp} (as calculated by AM) with increasing hydrogen content in the fuel stream (O_2 on cathode side), anode/cathode $\lambda = 8/24$ (left) and $4/12$ (right), $T = 160^\circ\text{C}$

The mass transport resistance to O_2 in the CCL is only calculated by the AM based on the calculated O_2 diffusion coefficient in the CCL and shows a clear decreasing trend (Figure 6.19) in the case of both current densities. This fits to our discussion of Figure 6.13.

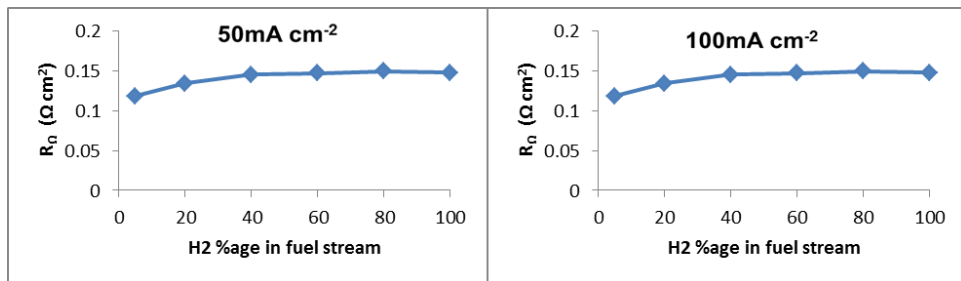


Figure 6.20: R_{Ω} (as calculated by ECM) with increasing hydrogen content in the fuel stream (O_2 on cathode side), anode/cathode $\lambda = 8/24$ (left) and $4/12$ (right), $T = 160^\circ\text{C}$

The ohmic resistance of the cell remains constant for all H_2 concentrations other than 5 %, where it is slightly lower as shown in Figure 6.20. This reasoning is similar to the discussion of the ohmic resistance in case of air on the cathode side (see Figure 6.14).

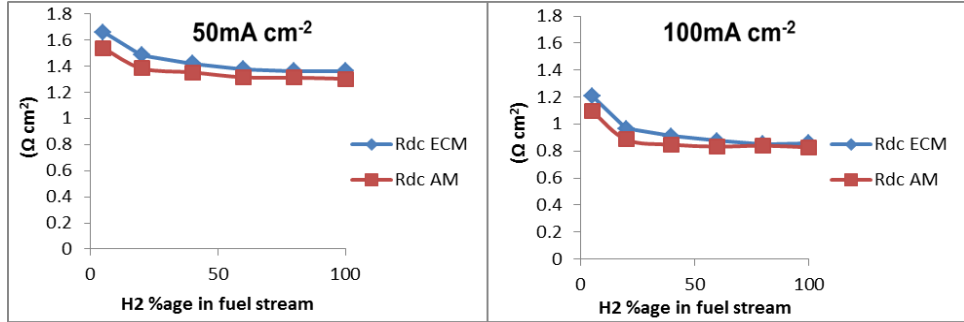


Figure 6.21: Comparison of R_{dc} for increasing hydrogen content in the fuel stream (O_2 on cathode side), anode/cathode $\lambda = 8/24$ (left) and $4/12$ (right), $T = 160^\circ\text{C}$

Finally, the DC resistance is compared in Figure 6.21 and is found to be in good agreement for both current densities. The DC resistance of the ECM is slightly higher for all H_2 percentages at 50 mA cm^{-2} and upto 60% H_2 for 100 mA cm^{-2} , indicating that the results from the ECM and the AM converge as the H_2 concentration approaches 100% (negligible anode contribution to cell impedance). The match of R_{dc} for 80 and 100% H_2 for 100 mA cm^{-2} is also quite good verifying the validity of the AM upto this current density.

6.3.3 Oxygen concentration change with hydrogen on the anode side

In this section the effect of O_2 concentration change in the cathode gas is shown while the anode gas is kept as 100% H_2 . The comparisons of the characteristic cell parameters are shown in Figure 6.22 through Figure 6.27.

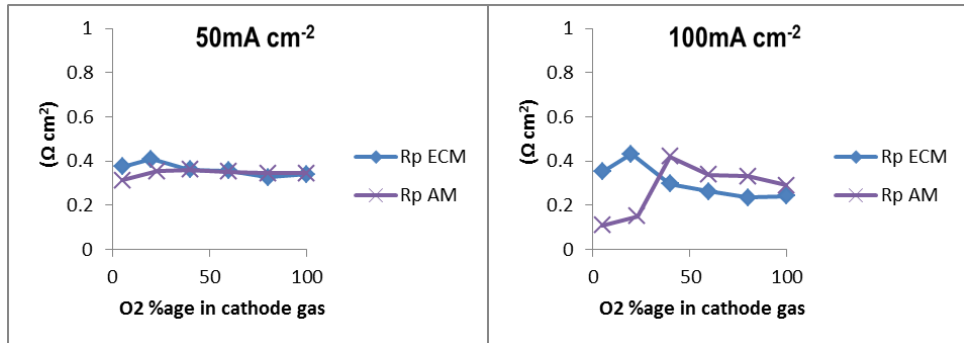


Figure 6.22: Comparison of R_p for increasing oxygen content in the cathode gas, anode/cathode $\lambda = 8/24$ (left) and $4/12$ (right), $T = 160^\circ\text{C}$

6.3. Comparison of fitting results

As can be seen in Figure 6.22, the R_p agreement for both models for 50mA cm^{-2} is particularly good. For 100mA cm^{-2} , the first two points are far apart but then again the AM values are slightly higher than the ECM values. The fitted values for O_2 concentrations of 5 and 20% are not the most reliable due to very high cathode flowrates to maintain the required stoichiometric ratios (24 for 50mA cm^{-2} and 12 for 100mA cm^{-2}). This would affect the performance in many ways including drying out of the CCL and membrane and removal/redistribution of PA.

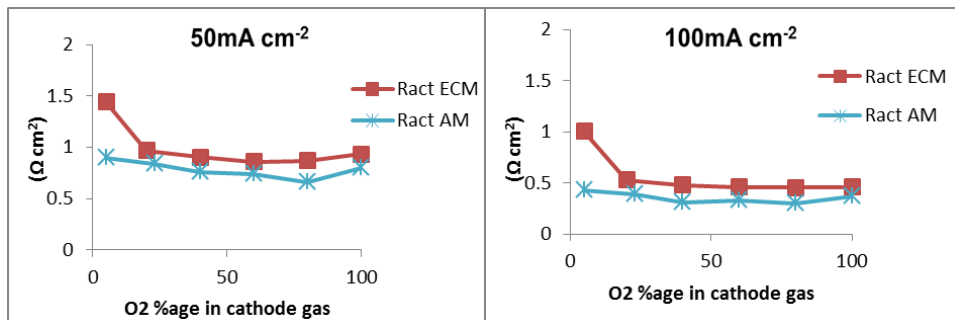


Figure 6.23: Comparison of R_{act} for increasing oxygen content in the cathode gas, anode/cathode $\lambda = 8/24$ (left) and $4/12$ (right), $T = 160^\circ\text{C}$

Figure 6.23 shows that the activation resistance remains constant for all O_2 concentrations except for 5%, where the ECM calculates a much higher value. The AM, however, calculates the same value as the calculated Tafel slope (b) does not change much. The takeaway here is that even going to 100% O_2 on the cathode side from 21% (air) does not reduce the R_{act} appreciably.

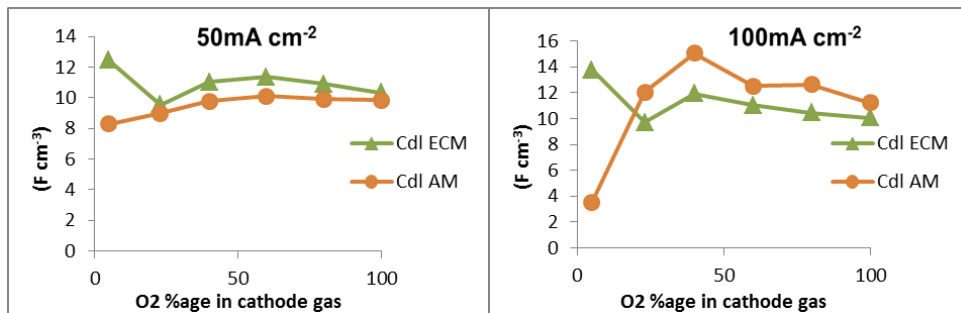


Figure 6.24: Comparison of C_{dl} for increasing oxygen content in the cathode gas, anode/cathode $\lambda = 8/24$ (left) and $4/12$ (right), $T = 160^\circ\text{C}$

It is visible in Figure 6.24 that the double layer capacitance is comparable and has similar trends for all O_2 %ages at both current densities (except for 5% O_2). The difference in values predicted by both models is still there, although much less pronounced.

6. Effects of Anode and Cathode Gas Concentration on Cell Impedance

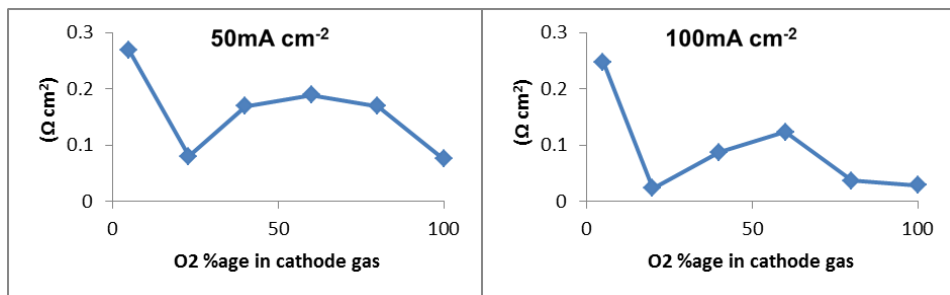


Figure 6.25: R_{oxp} (as calculated by AM) with increasing oxygen content in the cathode gas, anode/cathode $\lambda = 8/24$ (left) and $4/12$ (right), $T = 160^\circ\text{C}$

Figure 6.25 shows that the mass transport resistance of the CCL is high only for 5% O₂ (which is expected due to the very high cathode side gas flowrate as mentioned earlier) but it reduces suddenly for 21% O₂ and then increases slightly for 40 and 60 % O₂ and finally decreases again for 80 and 100% O₂. The trend is similar for both current densities and is explained by an initial drying out of the CCL due to the high gas flowrate and then an instable process of rehydration approaching equilibrium at the highest O₂ concentrations.

R_{oxp} is nevertheless an interesting and novel parameter which can only be calculated by the AM at low current densities. It would be interesting to be able to fit this parameter with a slightly modified ECM and be able to compare with the AM values.

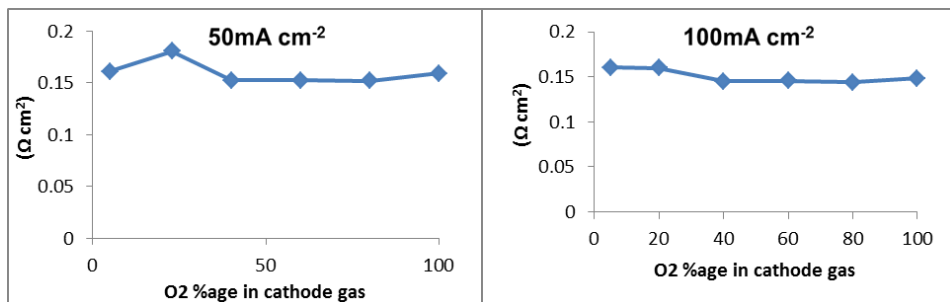


Figure 6.26: R_{Ω} (as calculated by ECM) with increasing oxygen content in the cathode gas, anode/cathode $\lambda = 8/24$ (left) and $4/12$ (right), $T = 160^\circ\text{C}$

The ohmic resistance remains constant other than the first two points (5 and 20% O₂) where it is slightly higher (Figure 6.26). The ohmic resistance of the cell is observed to be more or less stable at about $0.15 \Omega \text{ cm}^2$ throughout this study.

6.4. Summary

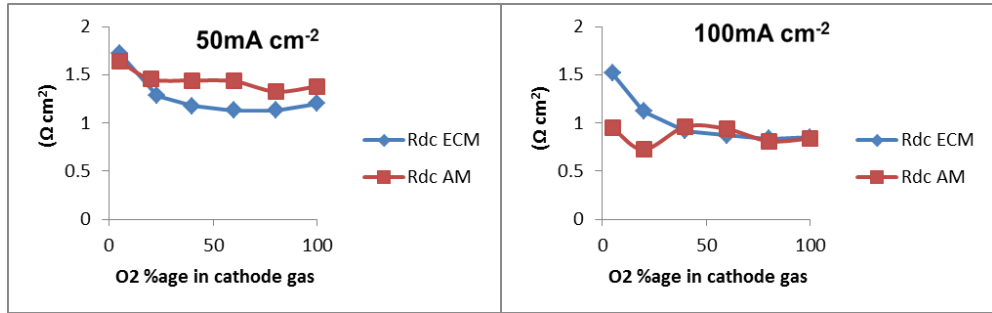


Figure 6.27: Comparison of R_{dc} for increasing oxygen content in the cathode gas, anode/cathode $\lambda = 8/24$ (left) and $4/12$ (right), $T = 160^\circ\text{C}$

The DC resistance of the AM is consistently higher than that of the ECM for a current density of 50mA cm^{-2} as shown in Figure 6.27. The first two points of the 100mA cm^{-2} comparison are not in agreement due to the much higher values of R_p and R_{act} of the ECM, but other values are in good agreement.

6.4 Summary

The summary regarding the effect of anode and cathode gas concentration on cell impedance are as follows:

1. The anode or cathode gas concentrations do not affect the ohmic resistance R_Ω significantly.
2. The H_2 concentration in the anode gas does not affect the R_p or R_{act} too much.
3. The H_2 concentration does affect the C_{dl} and R_{oxp} as calculated by the AM.
4. Impedance measurements at very low O_2 concentration (5% in the cathode gas) are not reliable for parameter calculation since the very high gas flowrates create temporary but significant artifacts in the cell performance and hence the impedance measurements.

The conclusions from this study regarding the ECM and AM used for fitting impedance data are listed below:

1. R_p values from the ECM and AM are in strong disagreement with the AM values being much higher than the ECM values in general. Since the AM calculates the values from actual physical parameters whereas the ECM just fits a resistance to the theoretical 45° line at the high frequency end of the Nyquist plot by using the porous electrode element of the Thales software, a better fitting element can be used.
2. The ECM always calculates a higher R_{act} than the AM. Again since the calculated value of the Tafel slope (b) by the AM is very realistic for the Tafel region (very low current density), the ECM overestimates the R_{act} . The possible reasons for this could be the underestimation of the protonic resistance as mentioned in the previous point, or the fact that

6. Effects of Anode and Cathode Gas Concentration on Cell Impedance

R_{oxp} is not calculated by the ECM and therefore the ECM overestimates the R_{act} since the total DC resistance must be the same.

3. The double layer capacitance trends are consistent for both models. The values differ quite a bit for low gas concentrations.

4. The mass transport resistance of the CCL (R_{oxp}) calculated by the AM is a novel parameter and agrees well with the diffusion coefficient of O_2 in PA found in the literature.

5. The DC resistance R_{dc} as determined by the ECM and AM are usually in agreement.

Since the mass transport resistance in the CCL (R_{oxp}) is a critical factor for CCL characterization, and present ECMs are unable to determine this factor, it is suggested to use the ECM in Figure 2.8 (for high current, low stoichiometry), but with a different interpretation of the second semi arc, which is related to the CCL mass transport at these operating conditions. Since mass transport is a slow process, it is usually seen at the low frequency end of the Nyquist plot. Furthermore, since the value of R_{oxp} is quite small, it is required to go to very low frequencies to properly capture this second semi arc. The present measurements are always done in the frequency range of 50mHz to 100kHz. The problem with going to even lower frequencies is that it needs considerably longer to take the impedance measurement. For example, going to 1mHz requires running the impedance device overnight for just one measurement. As for the R_p values, the porous electrode is currently the best modelling element available in the Thales software, but care should be taken in interpreting the results and the results should be verified when possible.

The comparison of R_{oxp} values fitted by the AM and the suggested ECM is presented in Figure 6.28 and Figure 6.29 below for the cases of changing hydrogen (with pure oxygen on the cathode side) and oxygen content on the anode and cathode sides respectively. It can be seen that the trends are similar, but the ECM values are higher. This issue can be resolved by going to lower frequencies for the EIS measurements as mentioned before.

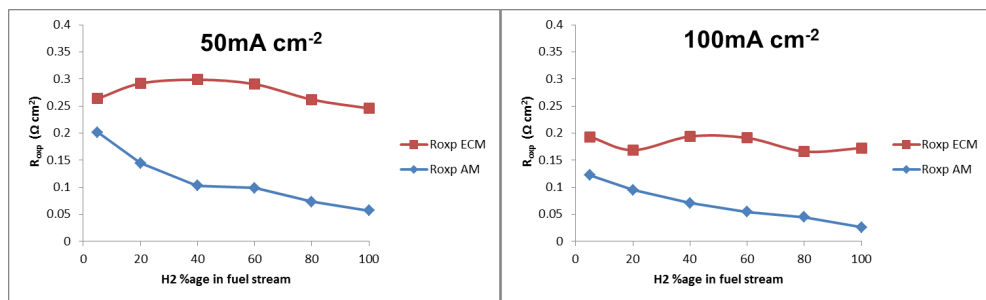


Figure 6.28: Comparison of the predicted values of R_{oxp} by the suggested ECM with AM values for increasing hydrogen content on the anode side with pure oxygen on the cathode side and anode/cathode λ of 8/24 (left) and 4/12 (right). $T = 160^\circ\text{C}$

6.4. Summary

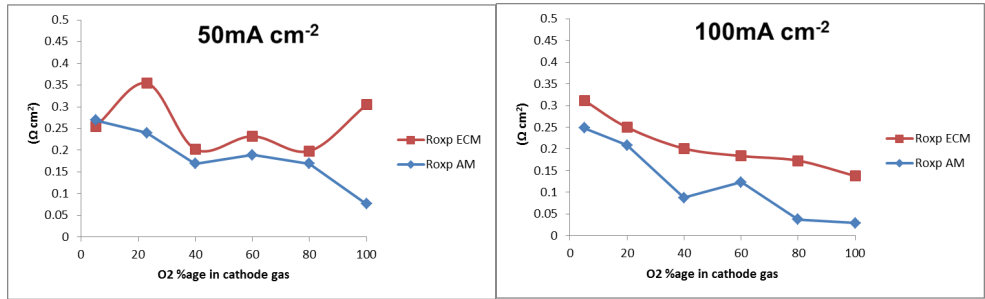


Figure 6.29: Comparison of the predicted values of R_{oxp} by the suggested ECM with AM values for increasing oxygen content on the cathode side with hydrogen on the anode side and anode/cathode λ of 8/24 (left) and 4/12 (right). $T = 160^{\circ}\text{C}$

7 Accelerated Degradation Study

Degradation of materials and components is a very important issue in PEFCs. It is especially so for the HT-PEFC as the higher operating temperature causes much faster degradation of cell components. Not many comprehensive publications on the degradation of the HT-PEFCs are found in the literature; for example, one such detailed work was published by Schmidt et al [171]. Standardization of accelerated stress tests (AST) and degradation protocols for HT-PEFCs is also an important task for better comparisons between different groups. It is hoped that this chapter will be a small but significant step in this direction.

7.1 Experimental

A degradation testing plan is devised for five stressors for accelerated degradation of the HT-PEFC MEAs. The standard 17.64cm^2 cell is used for testing all MEAs and the standard break-in procedure is run on the cells before any testing (see section 3.1). The BOL UI curves are taken immediately after the break-in procedure. Then BOL impedance and CV measurements are performed to obtain the BOL characteristic parameters and ECSA of the fuel cell. Then each cell is run for 100 hours of uninterrupted operation on a particular stressor. At the end of testing, the EOL UI curves are taken and also EOL Impedance and CV measurements are performed. When taking UI curves, always three curves are taken one after the other and averaged. Impedance and CV measurements are always performed with similar settings to maintain comparability. The impedance measurements are always taken with an anode/cathode stoichiometry of 2/2 at 200mA cm^{-2} . Stable conditions are ensured before taking the impedance measurements. The impedance data is analyzed with a standard ECM for fitting high current density impedance which has two parallel R/CPE combinations to model the two semi arcs expected in the data. The first semi arc represents the activation losses, whereas the second one represents the mass transfer losses of the fuel cell. Since with pure H_2 operation, the anode losses can be neglected, these losses are mainly affiliated with the cathode side.

Three commercially available HT-PEFC MEAs from Advent technologies[®] are used for this campaign. Advent technologies[®] recently acquired the patented materials and manufacturing processes of the Celtec[®] PW1100 HT-PEFC MEA from BASF. This MEA is now available under the product series APM of Advent. The MEAs used for this campaign along with relevant information are shown in Table 7.1.

7.1. Experimental

Table 7.1: List of commercial MEAs from Advent technologies[®] used for degradation testing

Serial #	Product MEA series name	Membrane type	GDE type
1	AAM	TPS	Advent GDE
2	ABM	TPS	BASF GDE
3	APM	PBI	BASF GDE

The TPS type membrane is a specialized membrane by Advent which consists of pyridine type structures around a stable polymer. The PBI type membrane is the one previously available under the name of Celtec[®] by BASF and now by Advent under the MEA series APM. This PBI membrane is doped with PA using the sol-gel technique previously patented by BASF and now by Advent. The PBI membrane has a high PA content ($34\text{mg cm}^{-2} \pm 4$) [172] and thus higher protonic conductivity than the TPS membrane ($0.1\Omega^{-1}\text{cm}^{-1}$ vs. $0.08\Omega^{-1}\text{cm}^{-1}$) [127], which is more robust for harsh operating conditions. The BASF carbon cloth GDE is also now used by Advent in the product series ABM and APM respectively. In effect, the AAM series is the same as the previously known Advent TPS MEA; the APM series is the same as the Celtec[®] PW1100 MEA from BASF previously, while the ABM series is a new mixture of both MEAs with the membrane of the former and the GDE of the latter [127].

7.1.1 Stressors and their implementation

Five different stressors are used to test the MEAs. The stressors and their respective ranges or values along with implementation mode and dominant degradation modes are given in Table 7.2.

Table 7.2: Used stressors, their ranges, implementation modes and dominant degradation modes

Stressor	Range/Value	Implementation mode	Dominant degradation mode(s)
OCV operation	$V > 0.7V$	$i = 0.0A\text{ cm}^{-2}$	Carbon corrosion [61]
Potential cycling	0.2-0.7V	$I = 0.2 - 0.6 - 0.2A\text{ cm}^{-2}$ Current step = $0.05A\text{ cm}^{-2}$ Time step = 5min	Pt particle growth and migration Carbon corrosion [173,174]
Thermal cycling	$140-180^{\circ}\text{C}$	$140-180-140^{\circ}\text{C}$ Temp. step = 10°C Time step = 1hr.	Mechanical and thermal degradation Pt sintering and dissolution [84]
High cathode stoich.	Cathode $\lambda > 10$	ca. $\lambda = 12$	Water vapor and PA removal [88,175]
High temperature operation	$180-200^{\circ}\text{C}$	$T = 180^{\circ}\text{C}$	Ionomer degradation Pt particle growth Pin hole formation [55,176]

Although it is impossible to perfectly isolate a single degradation mechanism, it is hoped to make the relevant mode of degradation the most dominant by operating the cell at a particular stressor.

7.1.2 Benchmarking with BOL UI and U_t curves for constant current density operation

UI curves are taken for each MEA after the break-in procedure and then it is run on a constant current density of $0.2A\text{ cm}^{-2}$ for 100 hours.

7.1. Experimental

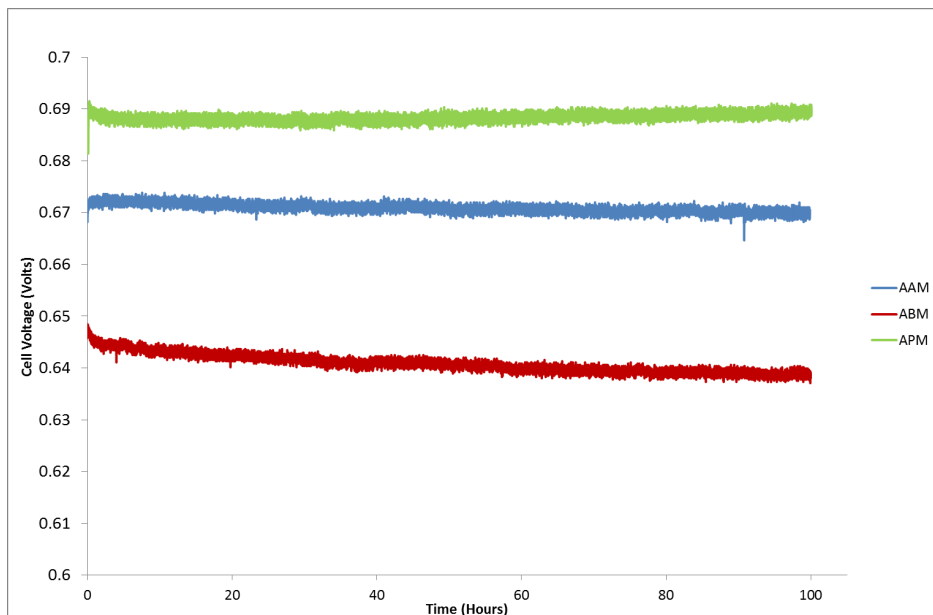


Figure 7.1: Ut curves for constant current density operation for 100 hours of the three Advent MEAs. Operating conditions: current density: 0.2A cm^{-2} , anode λ : 2 (gas: H_2), cathode λ : 2 (gas: air), $T=160^\circ\text{C}$.

The voltage vs. time (Ut) curves for a constant current density operation of the three commercial MEAs are shown in Figure 7.1. This is generally the best operating mode with the least degradation and therefore can be used as a benchmark for comparison with the harsh operating conditions of different stressors. It can be seen that the APM MEA has the best cell voltage throughout the 100 hour operation by a large margin (20mV higher than AAM MEA and about 45-50mV higher than the ABM MEA). The AAM MEA is clearly the second best MEA.

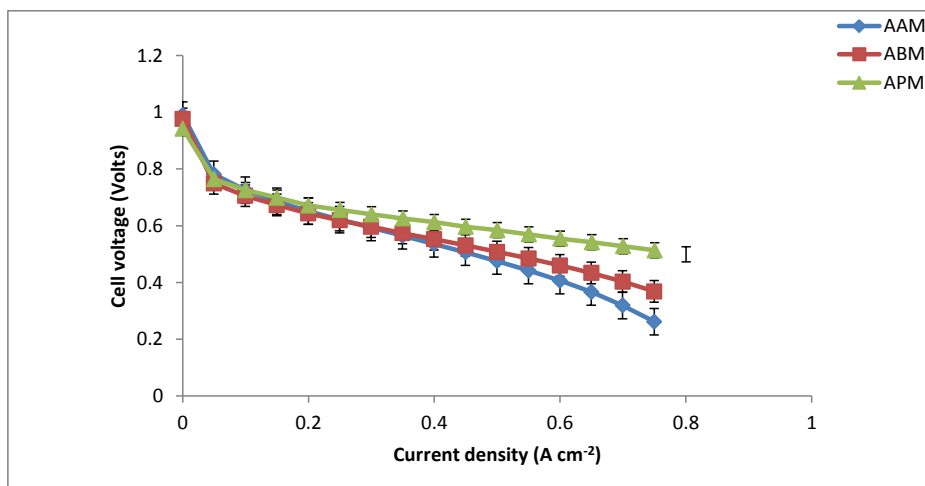


Figure 7.2: BOL averaged UI curves for the three MEAs, anode/cathode $\lambda = 2/2$, $T=160^{\circ}\text{C}$

The BOL comparison of the averaged UI curves for all three MEAs is presented in Figure 7.2. The APM MEA is again clearly the best. The comparison between the AAM and ABM MEAs is close with the AAM MEA better in the low to medium current density regime while ABM performing better in the high current density regime.

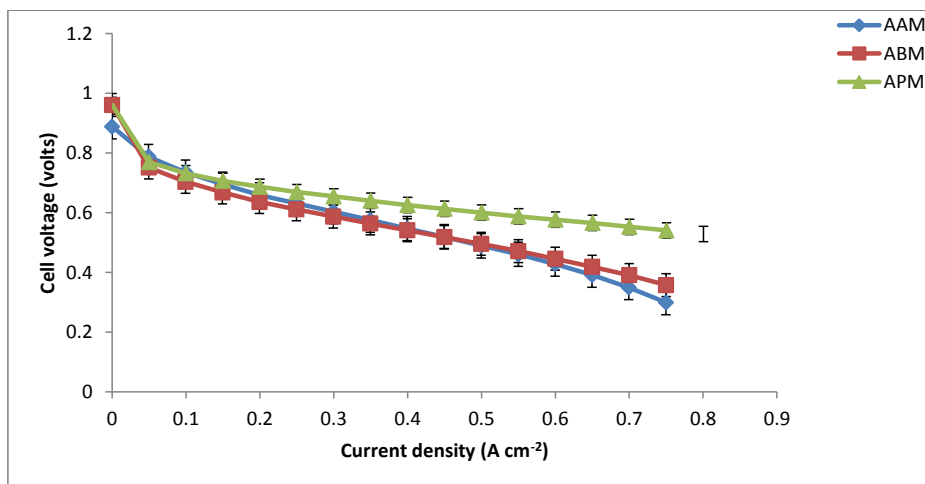


Figure 7.3: EOL averaged UI curves for the three MEAs, anode/cathode $\lambda = 2/2$, $T= 160^{\circ}\text{C}$

The EOL UI curve comparison is shown in Figure 7.3. It is observed that the APM MEA is still by far the best whereas the competition between the AAM and ABM MEAs has intensified with

7.2. Results

the AAM MEA not only improving a lot in the low current density regime, but also approaching the ABM MEA performance in the high current density regime.

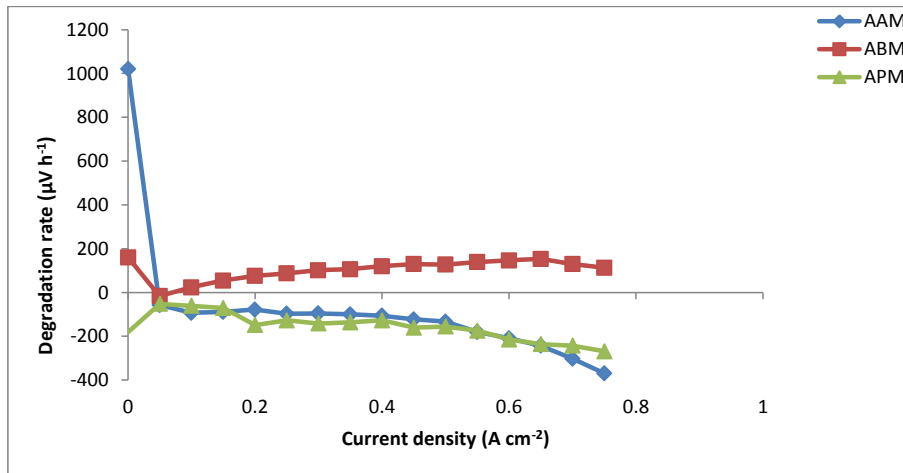


Figure 7.4: Degradation rates (voltage loss over time) of the three MEAs as a function of current density, anode/cathode $\lambda = 2/2$, $T=160^{\circ}\text{C}$

A cursory inspection of the degradation rates for the three MEAs in Figure 7.4 reveals that the AAM and APM MEAs have negative degradation rates (other than the OCV of the AAM MEA which shows a high degradation). Negative degradation rates imply improved cell performance after 100 hours of constant current density operation as observed by comparing the BOL and EOL UI curves as well. The ABM MEA however has a positive degradation rate for almost all current densities ranging upto $200\mu\text{V h}^{-1}$. Since we want to see the effect of stressors on cell performance, we therefore select the two MEAs which show the minimum degradation for constant current density operation for further testing with stressors. The AAM and APM MEAs are therefore selected for further testing while the ABM MEA is discarded from further testing due to its lower performance and higher rate of degradation at constant current density operation.

7.2 Results

The results for EOL cell performance of each of the AAM and APM MEAs for all the stressors are compared with the BOL and the constant current density results for evaluation of the effects of the stressors on cell performance and quantification of the degradation. A comparison of the BOL and EOL characteristic resistances and ECSA is also done to gain further insights into the effects of each stressor and determination of the degradation modes. It is hoped that isolation of these electrochemical characteristics will shed more light on the specific causes of each of these degradation modes and better mitigation strategies can thus be developed.

7.2.1 UI curves and degradation rate comparison (AAM MEA)

As discussed in section 7.1.1, the AAM MEA series from Advent technologies® has a TPS membrane, which has a lower protonic conductivity, but is considered to be more robust for harsh operating conditions.

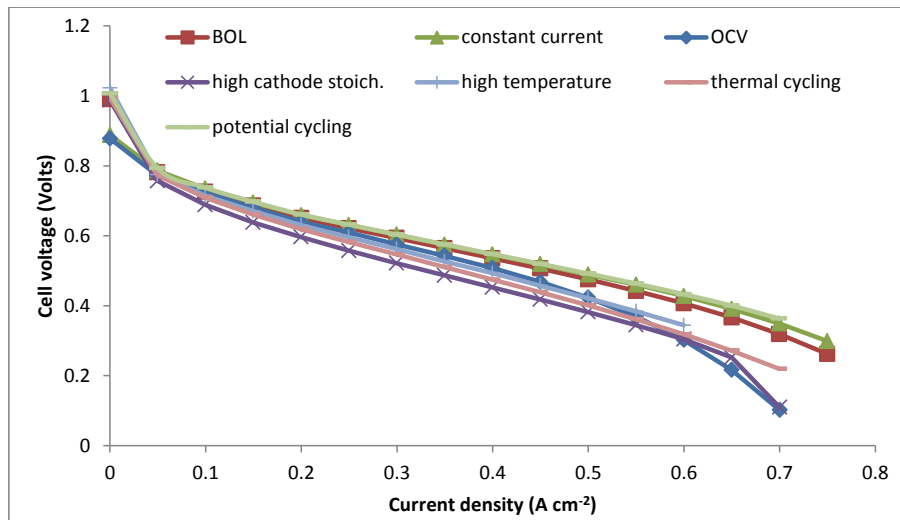


Figure 7.5: Comparison of EOL UI curves after different stress modes (AAM MEA, anode/cathode $\lambda = 2/2$ $T = 160^\circ\text{C}$)

The EOL UI curve comparison for this MEA with various stressors is presented in Figure 7.5. It is seen that not only constant current density operation improves cell performance after 100 hours as discussed in the previous section, but also potential cycling slightly improves the cell performance. This is an interesting result since potential (or load) cycling is meant to be a stressor which accelerates degradation, but has been reported in the literature recently [177]. The cell performance decreases considerably in case of all the other stressors and high cathode stoichiometry operation seems the worst stressor for the cell with consistently the highest voltage loss in the operating range due to removal of water vapor and PA from the TPB, thus reducing active sites for the ORR to take place. Also, the removal of water vapor reduces the concentration of the more conductive orthophosphoric acid [178], thus affecting the cell performance negatively. However, this has been reported as a reversible mode of degradation unless there is a PA loss of more than 40% [88]. The thermal cycling and high temperature operation are the next worst for the AAM MEA and then the OCV operation. There is a sharp decrease of cell voltage in case of high cathode stoichiometry and OCV operation after a current density of 0.65 A cm^{-2} , indicating increased concentration resistance and hence a lower limiting current density. The changes in characteristic resistances are discussed in detail in section 7.2.3.

7.2. Results

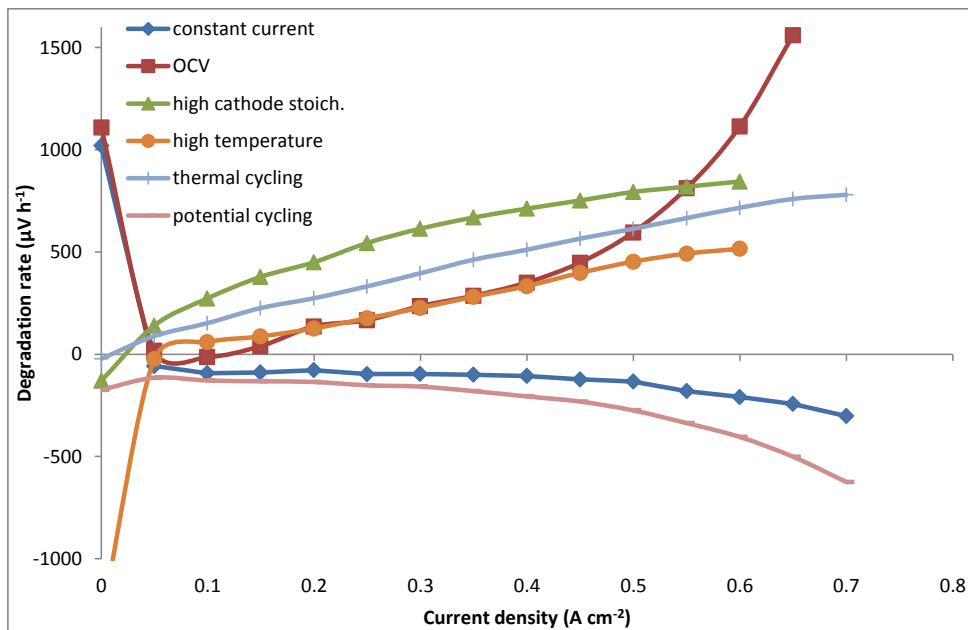


Figure 7.6: Comparison of EOL degradation rates for stressors (AAM MEA, anode/cathode $\lambda = 2/2$, $T = 160^\circ\text{C}$)

The degradation rates for each stressor are shown in Figure 7.6. The first thing to note is that the OCV of the fuel cell goes down a lot in the case of constant current density and OCV operation. The degradation rate is in excess of $1000\mu\text{V h}^{-1}$ in both cases which signifies considerably lower EOL OCV (loss of about 100mV in 100 hours). The opposite is true in the case of high temperature operation where the EOL OCV is much higher (in excess of 100mV). The OCV is more or less stable for the other stressors. The highest rate of degradation is observed in the case of OCV operation for higher current densities and for high cathode stoichiometry operation for lower current densities. Thermal cycling causes a higher degradation than constant high temperature operation in case of the AAM MEA; however there is no increase in OCV in the case of thermal cycling.

7.2.2 UI curves and degradation rate comparison (APM MEA)

The APM MEA differs from the AAM MEA in that it uses a PBI based membrane with a much higher PA content as described previously; therefore the degradation trends are different from the AAM MEA due to different degradation modes affecting the MEA performance.

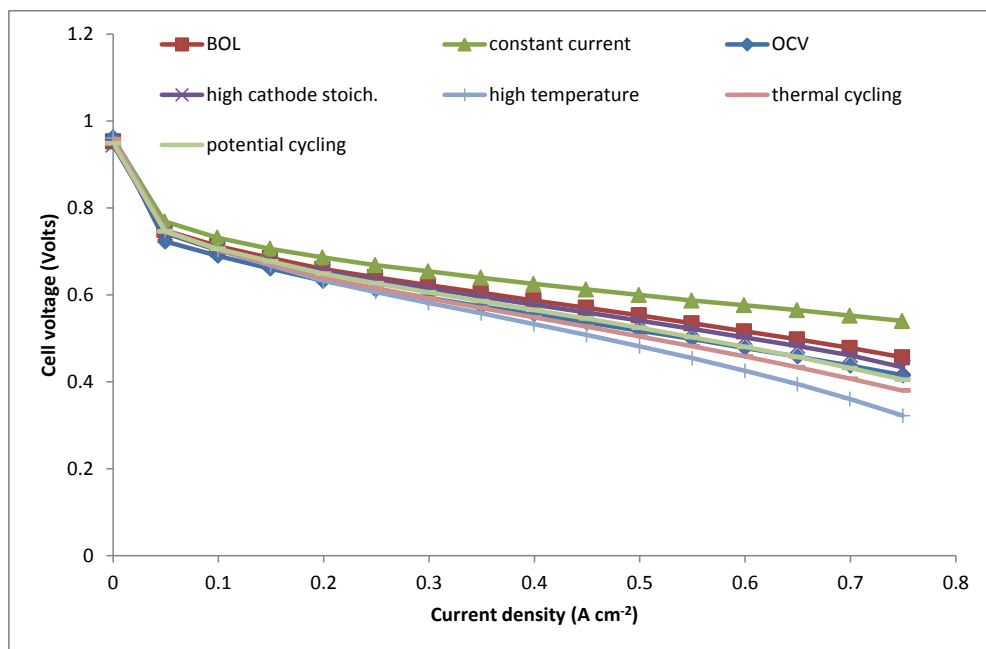


Figure 7.7: Comparison of EOL UI curves after different stress modes (APM MEA, anode/cathode $\lambda = 2/2$, $T = 160^\circ\text{C}$)

It can be seen in Figure 7.7 that the BOL performance is only surpassed by constant current density operation as discussed previously. There is some degradation for all the stressors, especially so in the high current density regime. High temperature operation and thermal cycling seem to cause the most degradation in this case. OCV operation is the next stressor which affects the cell performance and finally, potential cycling and high cathode stoichiometry operation are the least destructive stressors in this case. There is no performance improvement for this MEA in case of potential cycling as was the case for the AAM MEA. It should be noted that for most stressors, a significant difference from the BOL performance appears at a higher current density signifying an increased mass transport resistance. There is no indication of any cell approaching the limiting current density though, as in the case of the AAM MEA.

Figure 7.8 shows the degradation rates as a function of current density for all the stressors.

7.2. Results

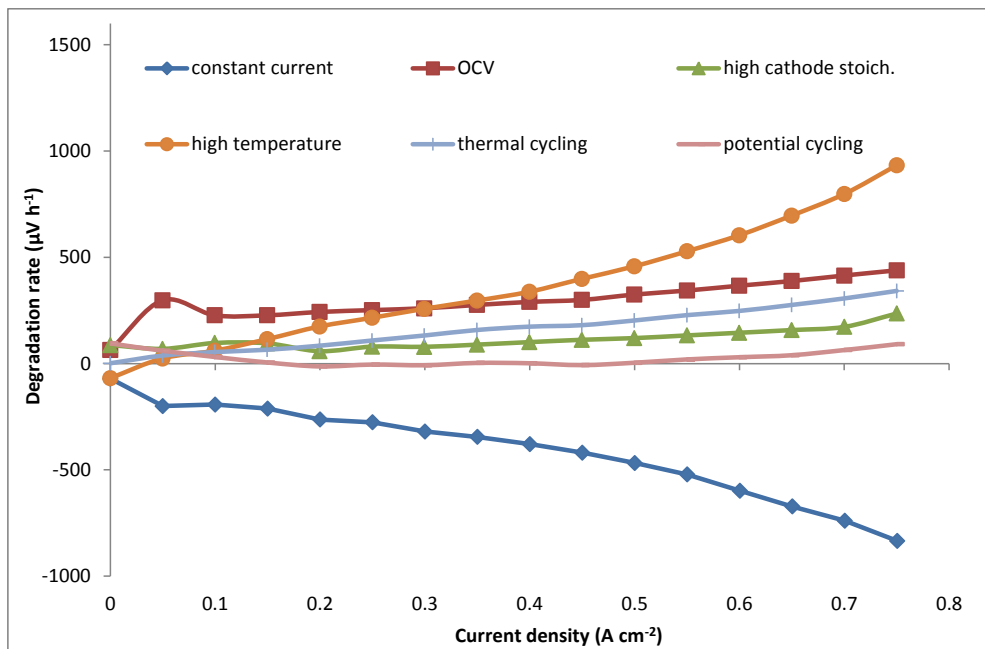


Figure 7.8: Comparison of EOL degradation rates for stressors (APM MEA, anode/cathode $\lambda = 2/2$, $T = 160^\circ\text{C}$)

It is observed firstly, that the OCV is stable for the APM MEA for all the stressors, unlike the AAM MEA, where different stressors caused large deviation in the OCV. The effect of most of the stressors is linear; i.e. increasing degradation rates with current density. The lowest degradation rate is for potential cycling. In case of the AAM MEA there was actually improved cell performance for potential cycling.

High cathode stoichiometry operation also does not cause very high degradation (maximum values of $100\mu\text{V h}^{-1}$) for the APM MEA as was the case for the AAM MEA with a peak degradation rate of $600\mu\text{V h}^{-1}$.

Thermal cycling and OCV operation both cause degradation in the range of 100 to $300\mu\text{V h}^{-1}$ for all current densities which are much lower values in comparison with the AAM MEA especially for higher current densities.

The constant high temperature operation causes the most degradation for the APM MEA at higher current densities ($i > 0.4\text{A cm}^{-2}$). There is a systematic quadratic increase in the degradation rate for this stressor as compared to the linear increase for the other stressors.

7.2.3 EIS and CV analysis

The impedance and CV data collected as described in section 7.1 is used for gaining further insights into the degradation mechanisms for each stressor. Each of these analyses is presented below.

EIS analysis

The characteristic electrochemical resistances are determined and analyzed by fitting the impedance data.

The impedance data is analyzed using the ECM for cell operation at high current density ($>100\text{mA cm}^{-2}$) and low cathode stoichiometry (<10) as presented in Figure 2.8. The model uses two parallel R/CPE combinations to model the two expected semi arcs in the Nyquist plot at a high current/low stoichiometry measurement. The first semi arc models the activation resistance and the double layer capacitance and the second semi arc models the mass transport resistance. Since pure H_2 is used as the anode gas, these resistances mainly represent the cathode side resistance of the fuel cell, as the anode resistance is negligible in this case [121]. Therefore, the calculated resistances and double layer capacitance can be attributed to the ORR taking place at the cathode side. The actual operating conditions used for measuring the Nyquist plots are a current density of 200mA cm^{-2} , anode/cathode stoichiometry of 2/2 and an operating temperature of 160°C (unless otherwise mentioned).

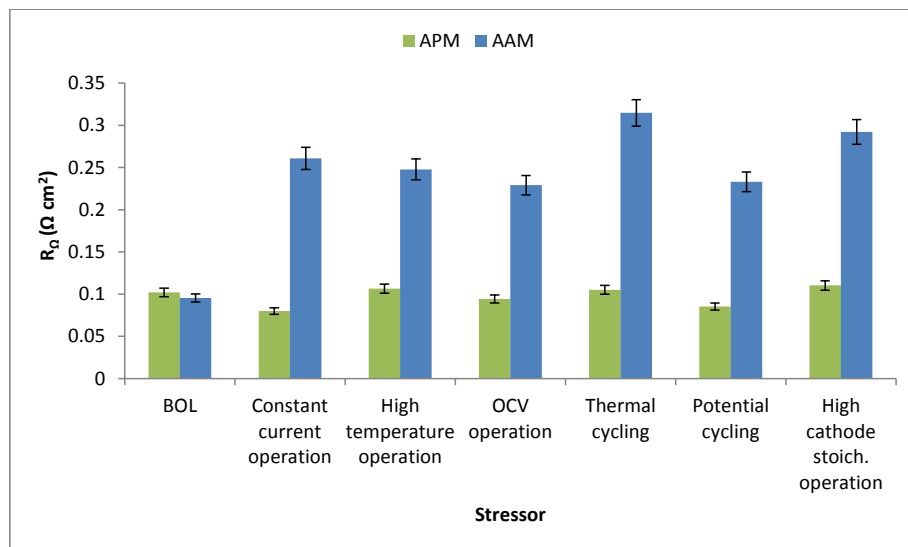


Figure 7.9: Comparison of the EOL ohmic resistance (R_Ω), current density = 200mA cm^{-2} , anode/cathode $\lambda = 2/2$

7.2. Results

All the fitting is done with the Thales software and the total error in the fit is always below 3%. The results are presented in the form of comparisons of the resistances and the double layer capacitance in Figure 7.9 to Figure 7.13.

It is seen in Figure 7.9 that the BOL ohmic resistances of both MEAs are very close to each other around $0.1\Omega\text{ cm}^2$. The R_Ω values for the APM MEA remain pretty close to the original value indicating minimal loss of PA from the membrane as the overall ohmic resistance is dominated by the membrane resistance [157]. The ohmic resistance of the AAM MEA however increases two to three times of its original value indicating either a significant loss of PA from the TPS membrane or a non-optimum redistribution or leaching of PA in the MEA during cell operation [51,179]. Further experiments would be necessary to come to concrete conclusions about the reasons of this but it is clear that there is significant room for improvement in the design and PA doping process of the AAM MEA as only 100 hour operation of all the stressors result in significant increase in the ohmic resistance of the MEA.

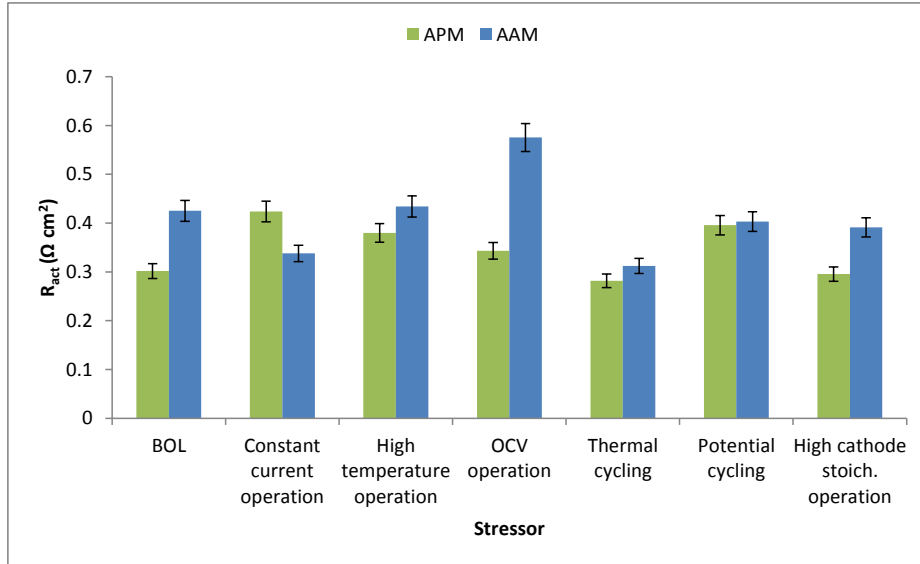


Figure 7.10: Comparison of the EOL activation resistance (R_{act}), current density = 200mA cm^{-2} , anode/cathode $\lambda = 2/2$

Figure 7.10 shows a comparison of the activation resistances of both MEAs after stressor operation. It is observed that the activation resistance increases for the APM MEA in case of constant current density by about $0.1\Omega\text{ cm}^2$. Infact, this is the highest increase in the activation resistance for this MEA. Potential cycling and high temperature operation also increase the activation resistance for the APM MEA but for other stressors it is relatively constant.

The activation resistance decreases by about $0.1\Omega\text{ cm}^2$ for the AAM MEA in case of constant current density operation. It also decreases in the case of thermal cycling by approximately the

same amount, whereas for other stressors it remains the same but an increase of more than $0.15\Omega\text{ cm}^2$ is observed in the case of OCV operation possibly due to corrosion of the carbon based catalyst support and Pt particle growth and dissolution [174].

Since the activation loss is one of the major factors for performance loss [168], any stressors causing a significant increase must be avoided. It can be seen here that OCV operation is detrimental for the AAM MEA, increasing its activation resistance by more than 30% and thus, must be avoided. The constant current density operation is not really a stressor and the slight increase in the activation resistance of the APM MEA cannot be avoided. Other stressors do not increase the activation resistance of either MEA significantly.

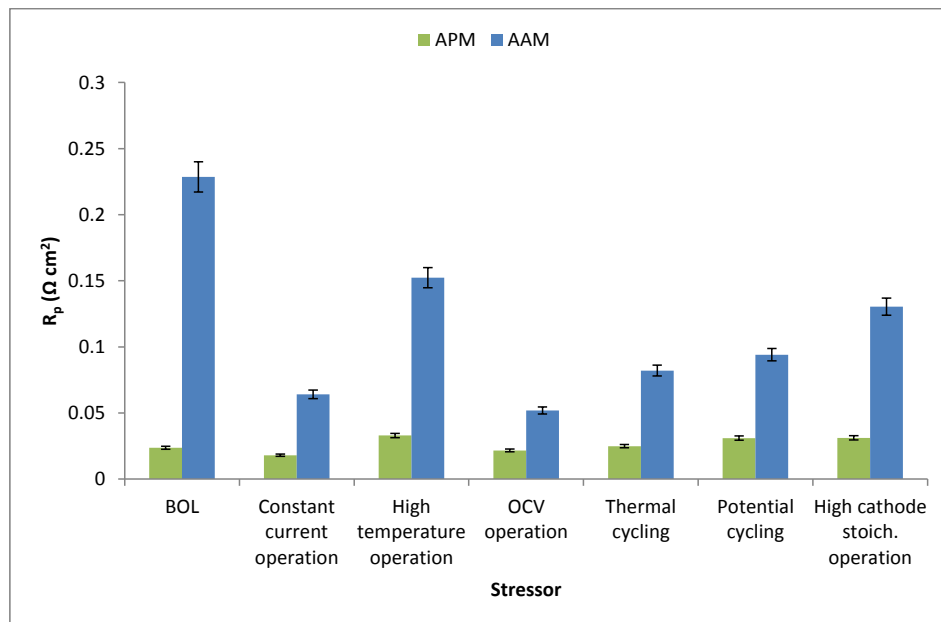


Figure 7.11: Comparison of the EOL protonic resistance (R_p), current density = 200mA cm^{-2} , anode/cathode $\lambda = 2/2$

The protonic resistance of the CCL is depicted in Figure 7.11. It gives a striking reminder of the fact that the APM MEA contains much more PA as compared to the AAM MEA by the comparison of the BOL R_p value (AAM has a multiple times higher value than APM). As the cells are operated though, the R_p value for the AAM MEA is reduced drastically indicating much improved PA distribution in the CCL after 100 hours of constant current density operation. In fact the R_p value for APM is more or less the same for all the stressors indicating that the protonic conductivity is not the problem in any of the cases, and it also improves by varying degrees from the BOL value for the AAM MEA as well, the largest improvement coming from constant current density operation as noted above.

7.2. Results

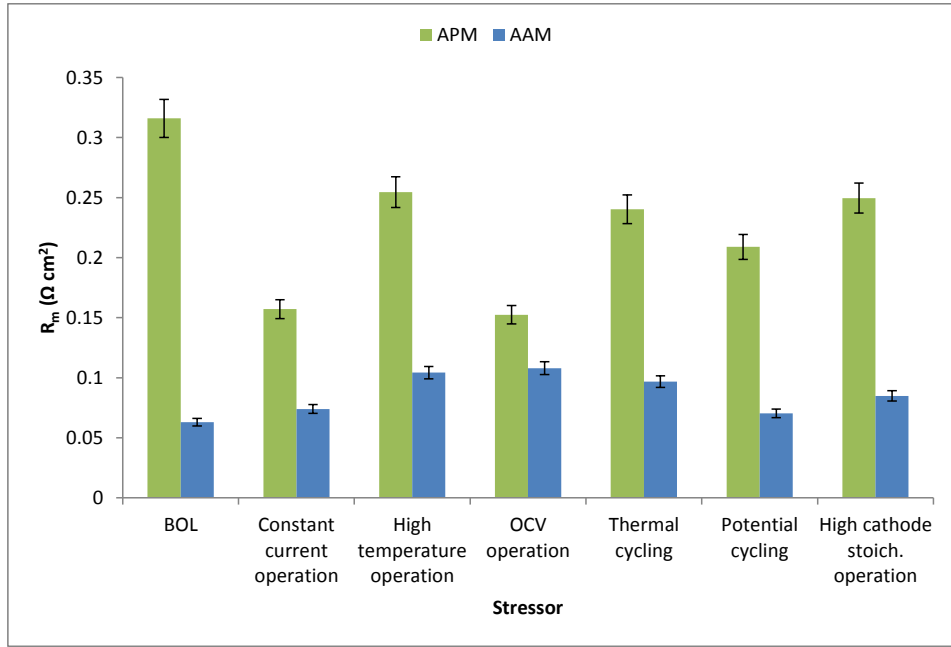


Figure 7.12: Comparison of the EOL mass transport resistance (R_m), current density = 200 mA cm^{-2} , anode/cathode $\lambda = 2/2$

Figure 7.12 depicts the mass transport resistances at the EOL for each stressor as well as BOL and constant current density operation values. Since the impedance measurements have been taken at a low stoichiometry (2/2) and higher current density (200 mA cm^{-2}), these values cannot just be attributed to the CCL, but instead also includes the GDL resistance [180].

It is observed that the BOL value of R_m for the APM MEA is more than six times higher than that of the AAM MEA. This is explained by the additional PA flooding the CCL and GDL pores at BOL. As the cells are operated for 100 hours at constant current density, the R_m value of the APM MEA comes down significantly but still is more than double the value of the AAM MEA. The AAM MEA shows almost double mass transport resistances in the case of high temperature operation and OCV operation and thus the reduction in the limiting current densities in these cases is verified. In the case of the APM MEA, OCV operation actually reduces the R_m considerably, possibly due to dehydration of the cell, but it remains high in the case of other stressors. This analysis indicates that the GDL and CCL for the APM MEA can be optimized to reduce the high R_m value for further improvement in its long term performance.

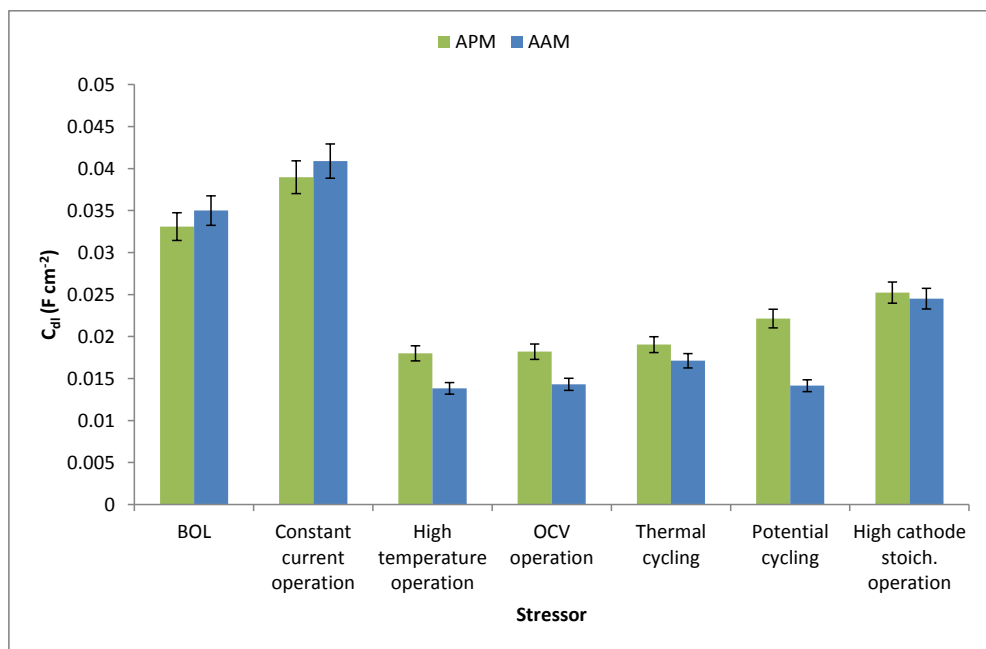


Figure 7.13: Comparison of the EOL double layer capacitance (C_{dl}), current density = 200mA cm^{-2} , anode/cathode $\lambda = 2/2$

Figure 7.13 presents the comparison of the double layer capacitance (C_{dl}) of the two MEAs for different stressors. The C_{dl} value is proportional to the ECSA and it is seen that it increases for both the MEAs from BOL to the constant current density operation whereas it decreases for all stressors for both MEAs. The most significant decrease in the C_{dl} is in the case of high temperature and OCV operation as well as thermal cycling.

CV analysis

The BOL and EOL ECSA for each cell is calculated according to the procedure described in section 3.3.2.

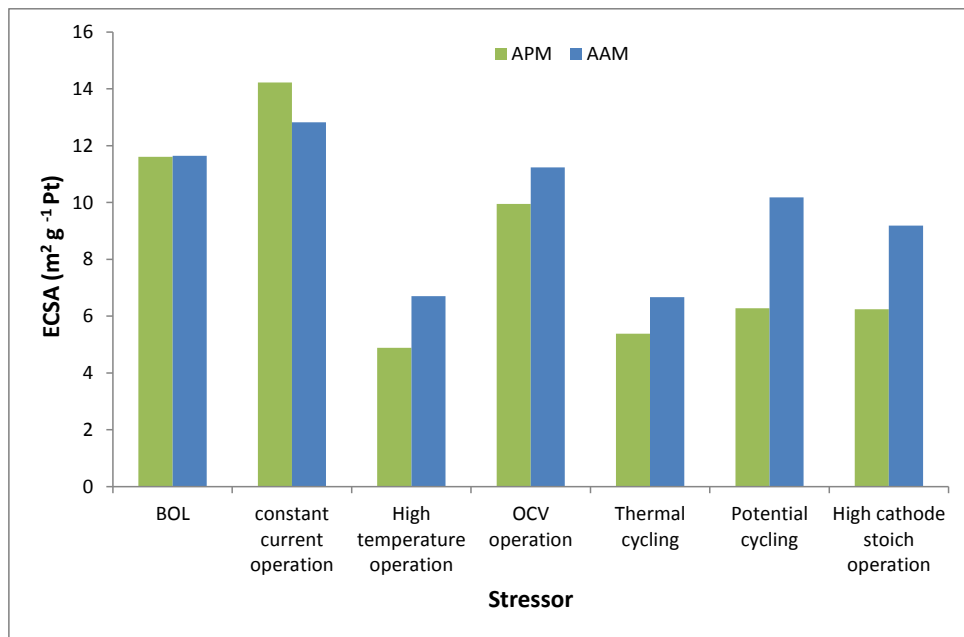


Figure 7.14: Comparison of the EOL electrochemical surface area (ECSA)

The EOL ECSA for both MEAs after 100 hour operation with each stressor is presented in Figure 7.14. It is observed that the ECSA increases in the case of constant current density operation as indicated by the increase in the C_{dl} value in Figure 7.13 and decreases for all the stressors. The largest decrease in ECSA for both MEAs is in the cases of high temperature operation and thermal cycling with a reduction of more than 50%. This is however, a partially recoverable change by reverting back to more normal operating conditions [181]. These results just indicate the immediate effects of the stressors on the ECSA.

7.3 Summary

The loss in OCV of the AAM MEA in the case of constant current density and OCV operation is significant and repeatedly measured. A loss in OCV loss can be attributed to the following causes:

- Partial pressures of the reactant gases according to the Nernst equation
- Partial pressure of water vapor produced according to the Nernst equation
- Gas crossover and leakage currents [182,183]
- Different solubility of gases in ortho and pyro PA [178]

Since the gases used are nearly constant in composition, the effect of the partial pressures of H_2 and O_2 respectively in accordance with the Nernst equation on the OCV can be neglected. The partial pressure of the water vapor produced on the cathode side is however, not constant in the

case of most stressors. This will not only have an influence in accordance to the Nernst equation, but also it affects the PA hydration/dehydration processes which lead to variation of the PA species concentration and PA distribution in the MEA and hence affects the fuel cell performance as mentioned above due to the different protonic conductivity and solubility of gases in the two PA species. Gas crossover and leakage currents can also affect the OCV and cell performance according to the literature [84,184]. The APM MEA shows a very stable OCV behavior for all the stressors with little change in the OCV.

Qi et al. [185] reported a mostly unrecoverable performance loss due to OCV operation of a HT-PEFC. They associated this loss of performance to loss of catalytic activity, increased mass transport resistance and increased Pt particle size by EIS and XRD measurements. In case of both AAM and APM MEAs, significant loss of performance for just 100 hours of cell operation is observed. The loss of ECSA in this case is not too large for either MEA, but the EOL mass transport resistance is large for both MEAs possibly due to increased Pt particle size and a resulting loss in catalytic activity as seen in the double layer capacitance comparison for OCV operation.

Yu et al. [186] reported significant loss of PA as a major cause for degradation of HT-PEFCs at higher temperatures (180°C or more). In the case of each MEA, high temperature operation and thermal cycling are indeed very effective stressors and cause significant degradation at higher current densities. This can be attributed to the loss of PA content. Since the AAM MEA has a lower PA content, the observed degradation rates for high temperature operation and thermal cycling for this MEA are much higher than for the APM MEA.

The effect of potential cycling on MEA performance is the least destructive in the case of both MEAs. An increased EOL performance is observed in the case of the AAM MEA, whereas very small degradation rates are observed for the APM MEA. There are contradicting reports in the literature regarding the effect of potential cycling and reports of performance loss [58] and also performance increase [177]. Further investigation is required to reach concrete conclusion about the effects of potential cycling on HT-PEFC MEAs.

The effect of high cathode stoichiometry is radically different for the investigated MEAs. It is the stressor with the most pronounced effect upto a current density of 550mA cm^{-2} (degradation rate of $820\mu\text{V h}^{-1}$) for the AAM MEA, whereas its effect is more than six times less for the APM MEA at the same current density (degradation rate $132\mu\text{V h}^{-1}$). This can be attributed to the loss of PA (APM has much higher PA) as discussed previously and is a major degradation mechanism for HT-PEFC operation [63].

This chapter has just scratched the surface of the degradation related issues for HT-PEFC. It is hoped that it will inspire in depth and detailed analysis of the effects of different stressors on the performance of the HT-PEFC and the associated degradation mechanisms which will ultimately lead to a standardized AST for the HT-PEFC.

7.3. Summary

8 Discussion and Conclusions

The experimental work of this thesis can be broadly divided into two parts. The first part concentrated on the determination of the best operating conditions and the degradation mechanisms and rates for different stressors of the HT-PEFC MEAs in single cell operation. Since material parameters and their effects on cell performance were not being directly investigated in this part, commercially available HT-PEFC MEAs were used for these campaigns. Chapters 4 and 7 covered this part. The second part concerned analyzing the material parameters of the in-house assembled HT-PEFC MEA and determining the underlying physical phenomena causing different cell performance. Possible improvements were also suggested by utilizing both the DoE and the EIS methods. Chapters 5 and 6 addressed this issue. The overall discussion of the results is presented in the next section.

8.1 Discussion

The DoE has been used in various research areas related to fuel cell technology and is gaining popularity due to its obvious advantages regarding resources, experimental planning and incorporation of factor interactions. Al-Hadeethi et al. [187] used the response surface methodology to determine the effect of temperature, gas flowrate and different flow configurations (co and counter-flow) on the performance of a LT-PEFC. This is interesting in the fact that a qualitative variable (flow configuration) is included in the analysis. Usually, inclusion of such a variable sways the planners towards OFAT, but the authors used the DoE successfully and determined a strong interaction between the temperature and flowrate of gases for the investigated range. They used the regression models to predict the cell performance very accurately. Other examples of successful DoE application in fuel cell research can be seen in [104–107, 188–190].

The impact of four important operating conditions (current density, operating temperature, and anode and cathode stoichiometries) on the performance of four commercial MEAs was investigated using a full factorial DoE in chapter 4. The main effects and interactions of the factors were determined to build statistical models for predicting cell voltages in the range of investigation of each factor. A comparison of the two sample sizes used (5 and 30) revealed the reliability of the statistical models based on a smaller sample size for a screening design. This indicates potential for significant savings in resources (costs, time and human resources) without compromising on the accuracy of results. It was determined that current density, operating temperature and their interaction were statistically significant for all the tested MEAs and hence featured in the corresponding statistical models. Taking UI curves at different factor setting allowed construction of reliable statistical models for different current densities while eliminating the current density explicitly from the models. These UI curves were named “DoE UI curves” and add a new dimension to MEA testing in single cells. It was also observed that the MEAs Celtec® PW1100 and DPS showed performance improvement and little or no degradation at the

8.1. Discussion

EOL whereas the other two MEAs tested showed some degradation. Although, the impact of the four investigated factors on HT-PEFC has been previously published in the literature [75,191–193], these are mostly stack based studies with different goals and therefore no direct comparisons of screening designs of HT-PEFC MEAs are available in the literature. However, it is hoped that the methodology presented in this thesis will become the norm for screening designs in the future.

The Celtec[®] PW1100 MEA (previously manufactured by BASF) materials and manufacturing processes have been recently acquired by Advent Technologies[®] and the same MEA is now available under the product series APM from Advent Technologies[®]. This MEA, along with another HT-PEFC MEA (AAM) with a TPS membrane and a carbon cloth based GDL material, also from Advent technologies[®] were selected for the degradation testing campaign (Chapter 7). The degradation testing showed a significant amount of degradation in both the MEAs with only 100 hour operation under the selected stressors. However, both MEAs showed performance improvement (in excess of $200\mu\text{V h}^{-1}$ at 600mA cm^{-2}) for 100 hours of constant current density (200mA cm^{-2}) operation. The trend for performance improvement is even higher for higher current densities implying reduced mass transport losses due to increased diffusion of the reactant gases to the TPB sites and improved PA distribution in the MEA. This would suggest considering increasing the currently standard break-in procedure time from 72 hours to 100 hours to maximize the constant current density operation at BOL of the cell, since it seems to optimize the PA redistribution in the MEA and improve the cell performance. Rabjerg [194] concluded the opposite for both sol-gel and post doped (doped after casting) HT-PEFC MEAs and suggested reducing the break-in duration for both types. This, however, contradicts our observations as discussed above.

The trends of the actual stressors on the MEA performance were much different for the AAM and APM MEAs. This has to do with the different membranes (PBI based for APM and TPS for AAM) as well as the different PA content (much higher in APM) and the doping procedures (sol-gel for APM and post doping for AAM MEA) of the MEAs. Also, both MEAs use carbon cloth as the porous material for the GDE, albeit, different carbon cloth materials [127] and the catalyst layers have similar Pt loadings. High cathode stoichiometry and thermal cycling caused the greatest degradation rates for the AAM MEA with a linear increase in the degradation rates with current density. The degradation rate caused by constant high temperature operation and OCV operation was also linear upto a current density of 450mA cm^{-2} , but the AAM MEA showed an exponential increase in the degradation rates at higher current densities signifying a much reduced limiting current density for the AAM MEA after 100 hour OCV operation, presumably due to loss of catalytic activity, increased concentration resistance and increased size of Pt particles. Since the measured ECSA shows less than 10% decrease from BOL, the exponential increase in the degradation rates at higher current densities can be attributed mainly to the increased concentration resistance and Pt particle sizes. The Pt particle sizes could not be examined in this case, since it is not allowed to do post mortem analysis of the commercial HT-PEFC MEAs due to non-disclosure agreements (NDA) with the MEA suppliers; however the

EOL concentration resistance as calculated by the EIS data indicated almost 100% increase from the BOL value, thus supporting the above argument. The increase in Pt particle size is also well documented in the literature with Qi et al. [185] reporting a Pt particle size increase of as much as 430% with OCV operation of 244.5 hours of a PBI based HT-PEFC MEA. De beer et al. [63] operated a HT-PEFC for 24 hours at OCV conditions without any flow of gases on either side and measured a substantially worse polarization curve and higher low frequency resistance in the Nyquist plot. They attributed these changes mainly to carbon corrosion of the catalyst support as well as in the GDL. The OCV operation in this study however, is different in that the flow of the gases was not completely shut off, but held constant for the values of anode/cathode stoichiometry of 2/2 at a current density of 200mA cm^{-2} . This resulted in a smaller decrease in the ECSA. Oono et al. [195] operated HT-PEFC single cells for about 18,000 hours at constant current density (200mA cm^{-2}) and attributed the steady decrease in cell performance during the first 14,000 hours to Pt agglomeration and the later more pronounced degradation to the membrane thinning and migration into the CL with the PA.

Load cycling for 100 hours actually improved cell performance for the AAM MEA and caused insignificant degradation in the case of the APM MEA. Due to the scarce and contradicting reports in the literature with regard to effect of load cycling on HT-PEFC performance, with some reporting a performance loss and some reporting an improvement, it was concluded that 100 hour operation is not enough to come to any concrete conclusions about the effects and causes of load cycling on the tested MEAs. The actual structure of the cycle used also has a profound effect. The cycle used in this study uses current density steps of 0.05A cm^{-2} with time steps of 5 minutes in the range of 0.2 to 0.6A cm^{-2} . This implementation mode seems to be favorable for both MEAs. Other cycles used in the literature usually have smaller time steps combined with larger current density steps resulting in different degradation rates. Thomas et al. [177] cycled four HT-PEFC single cells under load cycling between current densities of 200 and 800mA cm^{-2} and compared the degradation rates with a cell that was operated at a constant current density of 200mA cm^{-2} to find that load cycles which spent higher time at the lower current density actually had 1.5 times less degradation than the cell operated continuously at constant current density. They used rest times (operation time at the lower current density, the cells were operated at the higher current density for the rest of the time) from 15 seconds to 2 minutes and that the cell with the highest rest time showed the least degradation in a total operation time of about 2000 hours. Jeon et al. [196] found much more degradation of the cycled cells in comparison to the reference cell which was operated at a constant voltage of 0.6V. The cycles also used very small time steps (500 cycles in 35 hours) and different voltage ranges upto 1V. Rastedt et al. [197] used 6 minutes at 0.6A cm^{-2} and 14 minutes at 1A cm^{-2} as their load cycling protocol. They tested four different HT-PEFC MEAs with varied degradation. This discussion can be concluded by reasserting the need of a harmonized protocol for load cycling among the fuel cell industry to have more comparable results.

The degradation of the APM MEA had a different pattern altogether, with high temperature operation, OCV operation and thermal cycling causing the highest degradation rates. The

8.1. Discussion

degradation rates for constant high temperature operation for current densities higher than 500mA cm^{-2} were quadratic indicating an increased concentration resistance. This can be attributed to the considerable loss of PA, since the APM MEA has a high PA content and at high temperature operation ($T > 180^{\circ}\text{C}$), significant PA loss has been reported to be a dominant degradation mode for HT-PEFC MEAs [186]. The degradation rates for the AAM MEA were also very high for high temperature operation and thermal cycling, reinforcing this fact. High cathode stoichiometry, which causes drying out of the cell and a change in the PA species concentration in the MEA, did not cause a very high degradation for the APM MEA as for the AAM MEA, signifying the presence of additional PA for the APM MEA leading to a lesser dehydration effect. Søndergaard et al. [85] attributed the total amount of gas volume passed through a HT-PEFC during its lifetime, as well as other operating conditions such as current density and operating temperature to the rate of acid loss. They operated their cells in the range of 2 to 25 gas stoichiometries, 200 to 800mA cm^{-2} current density and 160 to 180°C operating temperatures. This study also used comparable conditions, although the high cathode stoichiometry used was 12. PA loss contributed significantly in most cases as discussed in section 7.3 to the observed degradation of the MEAs. Oono et al. [198] determined Pt agglomeration to be temperature dependent in early degradation, but found no effect of temperature on the depletion of PA rate, which caused a much higher degradation in the terminal stages of a long term test conducted on three HT-PEFC MEAs at cell temperatures of 150, 170 and 190°C respectively. They also found the least degradation in the cell operating at the lowest temperature.

The impedance analysis of both MEAs after 100 hour of stressor operation showed that R_{Ω} and R_p significantly increased for the AAM MEA while remaining more or less constant for the APM MEA. The R_m value was the limiting factor for the APM MEA, increasing significantly from the constant current density value for each stressor. The CV analysis showed a loss of ECSA for most of the stressors for both MEAs, but its recoverability was not quantified by reverting back to normal operating conditions for a substantial amount of time in this study. The main differences in the degradation behavior of the two investigated MEAs can also be attributed to the different materials (GDEs) and doping procedures (sol-gel vs. post doping after casting) to a certain extent [199], however, the separation and quantification of these effects was not a part of this study.

The second part of this experimental study concentrated on the improvement of the in-house assembled HT-PEFC MEA (Chapters 5 and 6). The idea was to characterize the performance of the CCL as it is the performance limiting part of the MEA (for pure hydrogen operation). Chapter 5 considered three major material parameters for the MEA and evaluated their combined effect on the single cell performance by using the DoE method for three different current densities (200, 400 and 600mA cm^{-2}). The considered factors were CCL thickness, PADL of the MEA and Pt loading of the CCL. Analysis of the results indicated significant interactions between the factors and the response surface indicated maximum cell performance with a CCL thickness of $120\mu\text{m}$, a PADL of 15mg cm^{-2} and a CCL Pt loading of 1mg cm^{-2} . A Pt loading of 0.6mg cm^{-2} also showed promising results, but the factor interactions favor the higher Pt loading value. An impedance analysis of the CCL electrochemical parameters indicated that the MEA with the suggested

material parameters of 120 μm CCL thickness, 15 mg cm^{-2} PADL and 1 mg cm^{-2} Pt loading had a much lower R_{act} in the low current and high stoichiometry regime than the other MEAs. Since R_{act} dominates the Tafel region, this MEA was determined to be the better one in comparison with the MEA with same CCL thickness and PADL, but a lower Pt loading of 0.6 mg cm^{-2} also showing promising performance. The improvement area for the selected MEA was the R_p , which was almost double than the other MEAs (0.175 $\Omega \text{ cm}^2$ compared to values close to 0.1 $\Omega \text{ cm}^2$ for the other MEAs) and must be improved for better cell performance at higher current densities. The PADL is a very important material parameter for HT-PEFC MEA performance. Oono et al. [200] investigated different doping levels for HT-PEFC single cells and concluded that a doping level of 10 mg cm^{-2} is optimum for a CL thickness of 20 μm and a Pt loading of 0.7 mg cm^{-2} . The present study would seem to contradict this result as the CCL thickness is 3 to 6 times higher (60 and 120 μm) and yet an increase in the doping level above 15 mg cm^{-2} causes a decrease in cell performance with the main effect of Pt loading being insignificant but a strong interaction between Pt loading and the CCL thickness. The PA doping process is also similar to the one used by Oono et al. (post doping after casting the membrane). They immersed the PBI membranes (no details provided) in 85% PA solution for a calculated amount of time (determined by an ex-situ survey) at 20, 40 and 60°C. The AM-55 membrane by FUMA-Tech was also doped by immersing it in 85% PA solution, but the temperature used was 110°C and the immersion time was 2 hours. The GDL material used was also different (TGP-H-090 Toray paper). Also, the catalyst ink recipe was different. Although, the two studies are not directly comparable, lessons can be learnt from this study, as a thinner CCL is highly desirable (reduced losses across the CCL) if it can withstand a higher PADL. The Pt loading of a HT-PEFC is generally in the range of 1 mg cm^{-2} or even higher for commercial MEAs [127,128,201,202]. This is much higher than the Pt loading of the LT-PEFC electrodes which are currently in the range of 0.1 to 0.4 mg cm^{-2} [203] with intense ongoing research for further reduction. The research in this regard in the field of HT-PEFC also needs to be increased. Liang et al. [126] achieved cathode loadings as low as 0.3 mg cm^{-2} by using the CCM method for manufacturing the HT-PEFC MEA and Su et al. [142] reported achieving a peak power density of 0.339 W cm^{-2} and peak cathode mass power of 0.967 W mg^{-1} Pt with a cathode loading of 0.350 mg cm^{-2} . Martin et al. [72] achieved a peak power density of 0.482 W cm^{-2} with oxygen and 0.321 W cm^{-2} with air on the cathode side with PBI based membranes using no binder material in the CCL and Pt loading of 0.1 mg cm^{-2} . They attributed this to the extended TPB in the CCL due to avoidance of the PA flooding of the CCL. These results are encouraging, but still laboratory based and a higher Pt loading remains the norm for HT-PEFC for now until long term stability and acceptable degradation rates can be achieved in addition to high performance. Unfortunately, not much experimental work has been done on optimizing the CCL thickness in HT-PEFC MEAs, and further research needs to be done in this area to determine the optimum balance between these three critical CCL material parameters.

Chapter 6 investigated the effect of varying anode and cathode gas composition on cell impedance in the high stoichiometry and low current density regime. The impedance data was analyzed with an ECM and also an analytical model by Kulikovsky valid for the low current density regime and the results were compared. An improved ECM was suggested on the basis of

8.2. Conclusions

the comparison, which would use two parallel RC combinations in the low current density regime, where the second RC combination can be used to calculate the oxygen transport limitation in the CCL. Although there are many reports of ECM based, numerical and analytical modelling of PEFC impedance in the literature [80–83,116,121–123,147,157,160,166,167,180,204–218], the novelty of the present work lies in the comparison with an ECM and extraction of means to determine relevant physical parameters to the CCL in the HT-PEFC MEA by improving the ECM.

The issues regarding HT-PEFC operation, performance and degradation investigated in this thesis represent some of the main obstacles to its commercialization. If addressed, the HT-PEFC has the potential to serve the energy sector, especially in transport and CHP applications, in the transition period to a completely hydrogen based sustainable economy.

8.2 Conclusions

This thesis concentrated on analyzing and quantifying the effects of different operating conditions and material parameters on the performance of the HT-PEFC MEA at the single cell level. The DoE methodology was used extensively to determine statistical models and response surfaces for the factors being considered. EIS was used for the quantification and comparison of the characteristic electrochemical parameters of the fuel cell and compare them to determine the most desirable conditions/parameters for MEA performance improvement. The main conclusions of this work are presented below.

- A small sample size ($n=5$) can be used for a full factorial DoE for screening MEA designs.
- PA loss, loss of Pt surface area by particle size growth, migration, agglomeration and dissolution, and carbon corrosion are three of the main degradation mechanisms responsible for performance loss in HT-PEFC operation with pure hydrogen.
- An in-house assembled MEA with a CCL thickness of 120 μm , PADL of 15 mg cm^{-2} and cathode Pt loading of 1 mg cm^{-2} is recommended as the most suitable from a performance viewpoint with further suggestions for improvement.
- A novel interpretation of a classical ECM is suggested in the low current density and high stoichiometry regime, for the approximation of mass transport resistance of the CCL from EIS data.

Nomenclature

Abbreviations

AFC	alkaline fuel cell
AM	analytical model
AST	accelerated stress test
BOL	beginning of life
CCL	cathode catalyst layer
CE	counter electrode
CL	catalyst layer
CPE	constant phase element
CV	cyclic voltammetry
DMFC	direct methanol fuel cell
DoE	design of experiments (method)
ECM	equivalent circuit model
ECSA	electro chemical surface area
EIS	electrochemical impedance spectroscopy
EOL	end of life
FRA	frequency response analyzer
GDE	gas diffusion electrode
GDL	gas diffusion layer
GHG	greenhouse gases
HHV	higher heating value
HOR	hydrogen oxidation reaction
HT-PEFC	high temperature polymer electrolyte fuel cell
ICE	internal combustion engine

Nomenclature

LHV	lower heating value
LT-PEFC	low temperature polymer electrolyte fuel cell
MCFC	molten carbonate fuel cell
MEA	membrane electrode assembly
MPL	micro porous layer
OCV	open circuit voltage
OFAT	one factor at a time (method)
ORR	oxygen reduction reaction
PA	phosphoric acid
PADL	phosphoric acid doping level
PAFC	phosphoric acid fuel cell
PBI	polybenzimidazole
PFA	perfluoroalkoxy
PEFC	polymer electrolyte fuel cell
PTFE	polytetrafluoroethylene
SOFC	solid oxide fuel cell
SS	stainless steel
STP	standard temperature pressure
TPB	triple phase boundary
WE	working electrode

Latin Symbols

b	mV per decade	Tafel slope
C	Farad	capacitance
C_{dl}	Farad cm^{-2}	double layer capacitance
C_{dl}	Farad cm^{-3}	volumetric double layer capacitance
C_{ref}	mol cm^{-3}	reference oxygen concentration
D_b	$\text{cm}^2 \text{s}^{-1}$	diffusion constant of oxygen in the GDL
D_{oxp}	$\text{cm}^2 \text{s}^{-1}$	diffusion constant of oxygen in the CCL
E	V	Nernst fuel cell potential
E_{cell}	V	fuel cell voltage
ECSA	$\text{m}^2 \text{g}^{-1}$	electrochemically active Pt surface area
E_o	V	theoretical fuel cell potential
f	Hz	frequency
f_i		individual frequency (of effects)
F	96485C mol^{-1}	Faraday's constant
i	A	current
j		imaginary number prefix
j_o	A cm^{-2}	current density
k		number of factor to be analyzed
L	Henry	Inductance
l_t	cm	CCL thickness
P	atm	pressure
P		probability of the occurrence of an event
P_{H_2}		normalized partial pressure of hydrogen
P_o	atm	atmospheric pressure

Nomenclature

P_{O_2}		normalized partial pressure of oxygen
P_{H_2O}		normalized partial pressure of water vapor
Q	$C\text{ cm}^{-2}$	charge per unit area/ pre-factor of a CPE
n		exponent of a CPE
n		number of samples
n		number of experiments required
n		total number of effects
n		number of electrons per molecule of hydrogen
R	Ω	resistance
R_{act}	$\Omega\text{ cm}^2$	activation resistance
R_{dc}	$\Omega\text{ cm}^2$	DC resistance
R_{Ω}	$\Omega\text{ cm}^2$	ohmic resistance
R_p	$\Omega\text{ cm}^2$	protonic resistance
R_m	$\Omega\text{ cm}^2$	mass transport resistance
R_{oxp}	$\Omega\text{ cm}^2$	mass transport resistance of the CCL
T	K	absolute temperature
V	V	voltage
Z	$\Omega\text{ cm}^2$	impedance
Z_i	$\Omega\text{ cm}^2$	Z score of the ith effect
Z_{CPE}	$\Omega\text{ cm}^2$	impedance of the CPE

Greek Symbols

ΔG	kJ mol^{-1}	change in Gibbs free energy of the reaction
ΔH	kJ mol^{-1}	enthalpy change of the reaction
ΔS	$\text{kJ mol}^{-1}\text{K}^{-1}$	entropy change of the reaction
η_{act}	V	activation overpotential

η_{conc}	V	concentration overpotential
η_{max}		maximum efficiency
η_{ohm}	V	ohmic overpotential
λ		stoichiometric ratio
Φ	degrees	phase angle
σ_{p}	S cm^{-1}	protonic conductivity
ε		experimental error
ω	rad s^{-1}	angular frequency

Bibliography

- [1] Marbán G, Valdés-Solís T. Towards the hydrogen economy? *International Journal of Hydrogen Energy* 2007;32:1625–37. doi:10.1016/j.ijhydene.2006.12.017.
- [2] Graves PE. Implications of global warming: Two eras. *World Development Perspectives* 2017;7–8:9–14. doi:10.1016/j.wdp.2017.10.002.
- [3] Shukla JB, Verma M, Misra AK. Effect of global warming on sea level rise: A modeling study. *Ecological Complexity* 2017;32:99–110. doi:10.1016/j.ecocom.2017.10.007.
- [4] Bong CPC, Lim LY, Ho WS, Lim JS, Klemeš JJ, Towprayoon S, et al. A review on the global warming potential of cleaner composting and mitigation strategies. *Journal of Cleaner Production* 2017;146:149–57. doi:10.1016/j.jclepro.2016.07.066.
- [5] Jain IP. Hydrogen the fuel for 21st century. *International Journal of Hydrogen Energy* 2009;34:7368–78. doi:10.1016/j.ijhydene.2009.05.093.
- [6] Barreto L, Makihiro A, Riahi K. The hydrogen economy in the 21st century: A sustainable development scenario. *International Journal of Hydrogen Energy* 2003;28:267–84. doi:10.1016/S0360-3199(02)00074-5.
- [7] Crabtree GW, Dresselhaus MS, Buchanan M V. The Hydrogen Economy. *Physics Today* 2004;39–45. doi:10.1063/1.1878333.
- [8] Barbir F. Introduction. *PEM Fuel Cells*, Elsevier; 2013, p. 1–16. doi:10.1016/B978-0-12-387710-9.00001-1.
- [9] Wang Y, Chen KS, Mishler J, Cho SC, Adroher XC. A review of polymer electrolyte membrane fuel cells: Technology, applications, and needs on fundamental research. *Applied Energy* 2011;88:981–1007. doi:10.1016/j.apenergy.2010.09.030.
- [10] Donitz W. Fuel cells for mobile applications, status, requirements and future application potential. *International Journal of Hydrogen Energy* 1998;23:611–5. doi:10.1016/S0360-3199(97)00075-X.
- [11] P.Corbo, Migliardini.F, Veneri.O. *Hydrogen Fuel Cells for Road Vehicles*. Springer; 2011. doi:10.1007/978-0-85729-136-3.
- [12] Chalk SG, Miller JF, Wagner FW. Challenges for fuel cells in transport applications. *Journal of Power Sources* 2000;86:40–51. doi:10.1016/S0378-7753(99)00481-4.
- [13] Barbir F. Fuel Cell Electrochemistry. *PEM Fuel Cells*, Elsevier; 2013, p. 33–72. doi:10.1016/B978-0-12-387710-9.00003-5.
- [14] O'hayre R, Cha S-W, Colella WG, Prinz FB. *Fuel Cell Technology. Fuel Cell Fundamentals*. 3rd ed., Wiley; 2016.
- [15] Park S, Lee J-W, Popov BN. A review of gas diffusion layer in PEM fuel cells: Materials and designs. *International Journal of Hydrogen Energy* 2012;37:5850–65. doi:10.1016/j.ijhydene.2011.12.148.

- [16] Park J, Oh H, Ha T, Lee Y II, Min K. A review of the gas diffusion layer in proton exchange membrane fuel cells: Durability and degradation. *Applied Energy* 2015;155:866–80. doi:10.1016/j.apenergy.2015.06.068.
- [17] Ye DH, Zhan ZG. A review on the sealing structures of membrane electrode assembly of proton exchange membrane fuel cells. *Journal of Power Sources* 2013;231:285–92. doi:10.1016/j.jpowsour.2013.01.009.
- [18] Song J, De castro S, Yu S. *BASF Stack Handbook*. 2011.
- [19] Middelma E, Kout W, Vogelaar B, Lenssen J, de Waal E. Bipolar plates for PEM fuel cells. *Journal of Power Sources* 2003;118:44–6. doi:10.1016/S0378-7753(03)00070-3.
- [20] Jung S-P, Lee C-I, Chen C-C, Chang W-S, Yang C-C. Development of novel proton exchange membrane fuel cells using stamped metallic bipolar plates. *Journal of Power Sources* 2015;283:429–42. doi:10.1016/j.jpowsour.2015.02.145.
- [21] Wang Y, Northwood DO. An investigation into polypyrrole-coated 316L stainless steel as a bipolar plate material for PEM fuel cells. *Journal of Power Sources* 2006;163:500–8. doi:10.1016/j.jpowsour.2006.09.048.
- [22] Zaidi SMJ, Matsuura T. *Polymer Membranes for Fuel Cells*. springer; 2009. doi:10.1007/978-0-387-73532-0.
- [23] Kulikovskiy A, Eikerling M. *Basic Concepts. Polymer Electrolyte Fuel Cells :Physical principles of materials and operation*, CRC Press Taylor & Francis Group; 2015, p. 1–28.
- [24] Kandlikar SG, Lu Z. Thermal management issues in a PEMFC stack – A brief review of current status. *Applied Thermal Engineering* 2009;29:1276–80. doi:10.1016/j.applthermaleng.2008.05.009.
- [25] Li H, Tang Y, Wang Z, Shi Z, Wu S, Song D, et al. A review of water flooding issues in the proton exchange membrane fuel cell. *Journal of Power Sources* 2008;178:103–17. doi:10.1016/j.jpowsour.2007.12.068.
- [26] Dai W, Wang H, Yuan X-Z, Martin JJ, Yang D, Qiao J, et al. A review on water balance in the membrane electrode assembly of proton exchange membrane fuel cells. *International Journal of Hydrogen Energy* 2009;34:9461–78. doi:10.1016/j.ijhydene.2009.09.017.
- [27] Ji M, Wei Z. A review of water management in polymer electrolyte membrane fuel cells. *Energies* 2009;2:1057–106.
- [28] Sui S, Wang X, Zhou X, Su Y, Riffat S, Liu C. A comprehensive review of Pt electrocatalysts for the oxygen reduction reaction: Nanostructure, activity, mechanism and carbon support in PEM fuel cells. *J Mater Chem A* 2017;5:1808–25. doi:10.1039/C6TA08580F.
- [29] Shao M, Chang Q, Dodelet J-P, Chenitz R. Recent Advances in Electrocatalysts for Oxygen Reduction Reaction. *Chemical Reviews* 2016;116:3594–657. doi:10.1021/acs.chemrev.5b00462.
- [30] Stacy J, Regmi YN, Leonard B, Fan M. The recent progress and future of oxygen

- reduction reaction catalysis: A review. *Renewable and Sustainable Energy Reviews* 2017;69:401–14. doi:10.1016/j.rser.2016.09.135.
- [31] Changlin Zhang, Yanbo Pan, Zhenmeng Peng XS. A review of Pt-based electrocatalysts for oxygen reduction reaction. *Frontiers in Energy* n.d.;11:268–85.
- [32] Araya SS, Zhou F, Liso V, Sahlin SL, Vang JR, Thomas S, et al. A comprehensive review of PBI-based high temperature PEM fuel cells. *International Journal of Hydrogen Energy* 2016;41:21310–44. doi:10.1016/j.ijhydene.2016.09.024.
- [33] Rosli RE, Sulong AB, Daud WR, Zulkifley MA, Husaini T, Rosli MI, et al. A review of high-temperature proton exchange membrane fuel cell (HT-PEMFC) system. *International Journal of Hydrogen Energy* 2017;42:9293–314. doi:10.1016/j.ijhydene.2016.06.211.
- [34] Authayanun S, Im-orb K, Arpornwichanop A. A review of the development of high temperature proton exchange membrane fuel cells. *Chinese Journal of Catalysis* 2015;36:473–83. doi:10.1016/S1872-2067(14)60272-2.
- [35] Chandan A, Hattenberger M, El-kharouf A, Du S, Dhir A, Self V, et al. High temperature (HT) polymer electrolyte membrane fuel cells (PEMFC) – A review. *Journal of Power Sources* 2013;231:264–78. doi:10.1016/j.jpowsour.2012.11.126.
- [36] Li Q, Jensen JO, Savinell RF, Bjerrum NJ. High temperature proton exchange membranes based on polybenzimidazoles for fuel cells. *Progress in Polymer Science* 2009;34:449–77. doi:10.1016/j.progpolymsci.2008.12.003.
- [37] Haque MA, Sulong ABB, Loh KSS, Majlan EH, Husaini T, Rosli RE. Acid doped polybenzimidazoles based membrane electrode assembly for high temperature proton exchange membrane fuel cell: A review. *International Journal of Hydrogen Energy* 2016;42:9156–79. doi:10.1016/j.ijhydene.2016.03.086.
- [38] Cheng X, Shi Z, Glass N, Zhang L, Zhang J, Song D, et al. A review of PEM hydrogen fuel cell contamination: Impacts, mechanisms, and mitigation. *Journal of Power Sources* 2007;165:739–56. doi:10.1016/j.jpowsour.2006.12.012.
- [39] G. Qian and B. C. Benicewicz. Fuel Impurity Effects on High Temperature PBI Based Fuel Cell Membranes. *Transactions, E C S Society, The Electrochemical* 2011;41:1441–8.
- [40] Das SK, Reis A, Berry KJ. Experimental evaluation of CO poisoning on the performance of a high temperature proton exchange membrane fuel cell. *Journal of Power Sources* 2009;193:691–8. doi:10.1016/j.jpowsour.2009.04.021.
- [41] Zhang C, Zhou W, Ehteshami MM, Wang Y, Chan SH. Determination of the optimal operating temperature range for high temperature PEM fuel cell considering its performance, CO tolerance and degradation. *Energy Conversion and Management* 2015;105:433–41. doi:10.1016/j.enconman.2015.08.011.
- [42] Krishnan P, Park J-S, Kim C-S. Performance of a poly(2,5-benzimidazole) membrane based high temperature PEM fuel cell in the presence of carbon monoxide. *Journal of Power Sources* 2006;159:817–23. doi:10.1016/j.jpowsour.2005.11.071.

- [43] Samsun RC, Pasel J, Janßen H, Lehnert W, Peters R, Stolten D. Design and test of a 5kWe high-temperature polymer electrolyte fuel cell system operated with diesel and kerosene. *Applied Energy* 2014;114:238–49. doi:10.1016/j.apenergy.2013.09.054.
- [44] Pan C, He R, Li Q, Jensen JO, Bjerrum NJ, Hjulmand HA, et al. Integration of high temperature PEM fuel cells with a methanol reformer. *Journal of Power Sources* 2005;145:392–8. doi:10.1016/j.jpowsour.2005.02.056.
- [45] Farrell CG, Gardner CL, Ternan M. Experimental and modelling studies of CO poisoning in PEM fuel cells. *Journal of Power Sources* 2007;171:282–93. doi:10.1016/j.jpowsour.2007.07.006.
- [46] Liu Y, Lehnert W, Janßen H, Samsun RC, Stolten D. A review of high-temperature polymer electrolyte membrane fuel-cell (HT-PEMFC)-based auxiliary power units for diesel-powered road vehicles. *Journal of Power Sources* 2016;311:91–102. doi:10.1016/j.jpowsour.2016.02.033.
- [47] Zhu Y, Zhu WH, Tatarchuk BJ. Performance comparison between high temperature and traditional proton exchange membrane fuel cell stacks using electrochemical impedance spectroscopy. *Journal of Power Sources* 2014;256:250–7. doi:10.1016/j.jpowsour.2014.01.049.
- [48] Authayanun S, Mamlouk M, Scott K, Arpornwichanop A. Comparison of high-temperature and low-temperature polymer electrolyte membrane fuel cell systems with glycerol reforming process for stationary applications. *Applied Energy* 2013;109:192–201. doi:10.1016/j.apenergy.2013.04.009.
- [49] Maximini M, Engelhardt P, Brenner M, Beckmann F, Moritz O. Fast start-up of a diesel fuel processor for PEM fuel cells. *International Journal of Hydrogen Energy* 2014;39:18154–63. doi:10.1016/j.ijhydene.2014.02.168.
- [50] Wang Y, Sauer DU, Koehne S, Ersoez A. Dynamic modeling of high temperature PEM fuel cell start-up process. *International Journal of Hydrogen Energy* 2014;39:19067–78. doi:10.1016/j.ijhydene.2014.09.095.
- [51] Jeong YH, Oh K, Ahn S, Kim NY, Byeon A, Park HY, et al. Investigation of electrolyte leaching in the performance degradation of phosphoric acid-doped polybenzimidazole membrane-based high temperature fuel cells. *Journal of Power Sources* 2017;363:365–74. doi:10.1016/j.jpowsour.2017.07.109.
- [52] Mack F, Heissler S, Laukenmann R, Zeis R. Phosphoric acid distribution and its impact on the performance of polybenzimidazole membranes. *Journal of Power Sources* 2014;270:627–33. doi:10.1016/j.jpowsour.2014.06.171.
- [53] Reimer U, Ehlert J, Janßen H, Lehnert W. Water distribution in high temperature polymer electrolyte fuel cells. *International Journal of Hydrogen Energy* 2016;41:1837–45. doi:10.1016/j.ijhydene.2015.11.106.
- [54] Bevilacqua N, George MG, Galbiati S, Bazylak A, Zeis R. Phosphoric Acid Invasion in High Temperature PEM Fuel Cell Gas Diffusion Layers. *Electrochimica Acta* 2017;257:89–98. doi:10.1016/j.electacta.2017.10.054.

Bibliography

- [55] Modestov AD, Tarasevich MR, Filimonov VY, Zagudaeva NM. Degradation of high temperature MEA with PBI-H₃PO₄membrane in a life test. *Electrochimica Acta* 2009;54:7121–7. doi:10.1016/j.electacta.2009.07.031.
- [56] Mamlouk M, Scott K. Analysis of high temperature polymer electrolyte membrane fuel cell electrodes using electrochemical impedance spectroscopy. *Electrochimica Acta* 2011;56:5493–512. doi:10.1016/j.electacta.2011.03.056.
- [57] Dhanushkodi SR, Kundu S, Fowler MW, Pritzker MD. Study of the effect of temperature on Pt dissolution in polymer electrolyte membrane fuel cells via accelerated stress tests. *Journal of Power Sources* 2014;245:1035–45. doi:10.1016/j.jpowsour.2013.07.016.
- [58] Yasuda K, Taniguchi A, Akita T, Ioroi T, Siroma Z. Platinum dissolution and deposition in the polymer electrolyte membrane of a PEM fuel cell as studied by potential cycling. *Phys Chem Chem Phys* 2006;8:746–52. doi:10.1039/B514342J.
- [59] Mitsuda K, Murahashi T, Matsumoto M, Usami K. Estimation of corrosion conditions of a phosphoric acid fuel cell. *Journal of Applied Electrochemistry* 1993;23:19–25. doi:10.1007/BF00241570.
- [60] Mitsuda K, Murahashi T. Air and fuel starvation of phosphoric acid fuel cells: A study using a single cell with multi-reference electrodes. *Journal of Applied Electrochemistry* 1991;21:524–30. doi:10.1007/BF01018605.
- [61] Reimer U, Schumacher B, Lehnert W. Accelerated Degradation of High-Temperature Polymer Electrolyte Fuel Cells: Discussion and Empirical Modeling. *Journal of the Electrochemical Society* 2014;162:F153–64. doi:10.1149/2.0961501jes.
- [62] Schmittinger W, Vahidi A. A review of the main parameters influencing long-term performance and durability of PEM fuel cells. *Journal of Power Sources* 2008;180:1–14. doi:10.1016/j.jpowsour.2008.01.070.
- [63] de Beer C, Barendse P, Pillay P, Bullecks B, Rengaswamy R. Classification of High Temperature PEM Fuel Cell Degradation Mechanisms Using Equivalent Circuits. *IEEE Transactions on Industrial Electronics* 2015;62. doi:10.1109/TIE.2015.2393292.
- [64] Liu G, Zhang H, Hu J, Zhai Y, Xu D, Shao Z gang. Studies of performance degradation of a high temperature PEMFC based on H₃PO₄-doped PBI. *Journal of Power Sources* 2006;162:547–52. doi:10.1016/j.jpowsour.2006.07.008.
- [65] Zhang J, Xie Z, Zhang J, Tang Y, Song C, Navessin T, et al. High temperature PEM fuel cells. *Journal of Power Sources* 2006;160:872–91. doi:10.1016/j.jpowsour.2006.05.034.
- [66] Luan Y, Zhang Y. Membrane Degradation. In: Wang H, editor. *PEM Fuel Cell Failure Mode Analysis*, CRC Press Taylor & Francis Group; 2012, p. 73–102.
- [67] Lehnert W, Wannek C, Zeis R. High Temperature Polymer Electrolyte Fuel Cells. In: Steinberger-Wilckens R, Lehnert W, editors. *Innovations in Fuel Cell Technologies*, Cambridge: Royal Society of Chemistry; 2010. doi:10.1039/9781849732109.
- [68] He Q, Yang X, Chen W, Mukerjee S, Koel B, Chen S. Influence of phosphate anion

- adsorption on the kinetics of oxygen electroreduction on low index Pt(hkl) single crystals. *Physical Chemistry Chemical Physics* 2010;12:12544. doi:10.1039/c0cp00433b.
- [69] He Q, Shyam B, Nishijima M, Ramaker D, Mukerjee S. Mitigating phosphate anion poisoning of cathodic Pt/C catalysts in phosphoric acid fuel cells. *Journal of Physical Chemistry C* 2013;117:4877–87. doi:10.1021/jp309282n.
- [70] Özdemir Y, Üregen N, Devrim Y. Polybenzimidazole based nanocomposite membranes with enhanced proton conductivity for high temperature PEM fuel cells. *International Journal of Hydrogen Energy* 2016. doi:10.1016/j.ijhydene.2016.04.132.
- [71] Mazúr P, Soukup J, Paidar M, Bouzek K. Gas diffusion electrodes for high temperature PEM-type fuel cells: role of a polymer binder and method of the catalyst layer deposition. *Journal of Applied Electrochemistry* 2011;41:1013–9. doi:10.1007/s10800-011-0325-9.
- [72] Martin S, Li Q, Jensen JO. Lowering the platinum loading of high temperature polymer electrolyte membrane fuel cells with acid doped polybenzimidazole membranes. *Journal of Power Sources* 2015;293:51–6. doi:10.1016/j.jpowsour.2015.05.031.
- [73] Zamora H, Plaza J, Cañizares P, Lobato J, Rodrigo MA. Improved Electrodes for High Temperature Proton Exchange Membrane Fuel Cells using Carbon Nanospheres. *ChemSusChem* 2016;9:1187–93. doi:10.1002/cssc.201600050.
- [74] Yan Q, Toghiani H, Causey H. Steady state and dynamic performance of proton exchange membrane fuel cells (PEMFCs) under various operating conditions and load changes. *Journal of Power Sources* 2006;161:492–502. doi:10.1016/j.jpowsour.2006.03.077.
- [75] Zhang C, Liu Z, Zhou W, Chan SH, Wang Y. Dynamic performance of a high-temperature PEM fuel cell - An experimental study. *Energy* 2015;90:1949–55. doi:10.1016/j.energy.2015.07.026.
- [76] Rastedt M, Pinar FJ, Wagner P. Impact of Contact Pressure Cycling on Non-Woven GDLs of HT-PEM Fuel Cells. *ECS Transactions* 2014;64:509–18. doi:10.1149/06403.0509ecst.
- [77] Andreasen SJ, Vang JR, Kaer SK. High temperature PEM fuel cell performance characterisation with CO and CO₂ using electrochemical impedance spectroscopy. *International Journal of Hydrogen Energy* 2011;36:9815–30. doi:10.1016/j.ijhydene.2011.04.076.
- [78] Taccani R, Zuliani N. Effect of flow field design on performances of high temperature PEM fuel cells: Experimental analysis. *International Journal of Hydrogen Energy* 2011;36:10282–7. doi:10.1016/j.ijhydene.2010.10.026.
- [79] Korsgaard AR, Refsgaard R, Nielsen MP, Bang M, K^{??} SK, Kær SK. Experimental characterization and modeling of commercial polybenzimidazole-based MEA performance. *Journal of Power Sources* 2006;162:239–45. doi:10.1016/j.jpowsour.2006.06.099.
- [80] Springer E, Zawodzinski A, Wilson MS, Golfesfeld S. Characterization of Polymer Electrolyte Fuel Cells Using AC Impedance Spectroscopy. *Journal of the Electrochemical Society* 1996;143:587–99. doi:10.1149/1.1836485.

Bibliography

- [81] Makharia R, Mathias MF, Baker DR. Measurement of Catalyst Layer Electrolyte Resistance in PEFCs Using Electrochemical Impedance Spectroscopy. *Journal of The Electrochemical Society* 2005;152:A970–7. doi:10.1149/1.1888367.
- [82] Yi JS, Song T -w. Performance Characterization of PEM Fuel Cells Using AC Impedance Spectroscopy: I. Model-Based Analysis. *Journal of the Electrochemical Society* 2012;160:F141–52. doi:10.1149/2.053302jes.
- [83] Kulikovskiy AA. One-Dimensional Impedance of the Cathode Side of a PEM Fuel Cell: Exact Analytical Solution. *Journal of the Electrochemical Society* 2014;162:F217–22. doi:10.1149/2.0151503jes.
- [84] Galbiati S, Baricci A, Casalegno A, Marchesi R. Degradation in phosphoric acid doped polymer fuel cells: A 6000 h parametric investigation. *International Journal of Hydrogen Energy* 2013;38:6469–80. doi:10.1016/j.ijhydene.2013.03.012.
- [85] Søndergaard T, Cleemann LN, Becker H, Steenberg T, Hjuler HA, Seerup L, et al. Long-Term Durability of PBI-Based HT-PEM Fuel Cells - Effect of Operating Parameters. Submitted to *Journal of The Electrochemical Society* 2017;165. doi:10.1149/2.0081806jes.
- [86] Ossianer T, Perchthaler M, Heinzl C, Schönberger F, Völk P, Welsch M, et al. Influence of membrane type and molecular weight distribution on the degradation of PBI-based HTPEM fuel cells. *Journal of Membrane Science* 2016;509:27–35. doi:10.1016/j.memsci.2016.02.037.
- [87] Tang H, Qi Z, Ramani M, Elter JF. PEM fuel cell cathode carbon corrosion due to the formation of air/fuel boundary at the anode. *Journal of Power Sources* 2006;158:1306–12. doi:10.1016/j.jpowsour.2005.10.059.
- [88] Eberhardt SH, Lochner T, Büchi FN, Schmidt TJ. Correlating Electrolyte Inventory and Lifetime of HT-PEFC by Accelerated Stress Testing. *Journal of The Electrochemical Society* 2015;162:F1367–72. doi:10.1149/2.0591512jes.
- [89] Zhou F, Andreasen SJ, Kær SK, Yu D, Juhl S, Knudsen S. Analysis of accelerated degradation of a HT-PEM fuel cell caused by cell reversal in fuel starvation condition. *International Journal of Hydrogen Energy* 2015;0:3–9. doi:10.1016/j.ijhydene.2014.12.082.
- [90] Park J, Wang L, Advani SG, Prasad AK. Mechanical Stability of H₃PO₄-Doped PBI/Hydrophilic-Pretreated PTFE Membranes for High Temperature PEMFCs. *Electrochimica Acta* 2014;120:30–8. doi:10.1016/j.electacta.2013.12.030.
- [91] Box EPG, Hunter JS, Hunter JW. *Statistics for Experimenters*. 2nd ed. Wiley Series in Probability and Statistics; 2005. doi:10.1080/00401706.1979.10489788.
- [92] Montgomery, C D. *Design and Analysis of Experiments*. 5th ed. John Wiley and Sons; 2001. doi:10.1002/qre.458.
- [93] Montgomery DC, Runger GC, Hubele NF, Runger C. George, Hubele NF. *Engineering Statistics*. 5th ed. Wiley; 2011. doi:10.1007/s13398-014-0173-7.2.

- [94] Czitrom V. One-Factor-at-a-Time Versus Designed Experiments. American Statistical Association 1999;53:6. doi:10.2307/2685731.
- [95] Rüttimann BG, Wegener K. The power of DOE : How to increase experimental design success and avoid pitfalls. Journal of Service Science and Management 2015;8:250–8.
- [96] Lye LM. Tools and Toys for Teaching Design of Experiments. General Conference of the Canadian Society for Civil Engineering, 2005, p. 1–9.
- [97] de Mast J. A methodological comparison of three strategies for quality improvement. International Journal of Quality & Reliability Management 2004;21:198–213. doi:10.1108/02656710410516989.
- [98] Tanco M, Viles E, Pozueta L. Comparing Different Approaches for Design of Experiments (DoE). Advances in Electrical Engineering and Computational Science SE - 52, vol. 39, 2009, p. 611–21. doi:10.1007/978-90-481-2311-7_52.
- [99] Box GEP, Wilson KB. On the Experimental Attainment of Optimum Conditions. Journal of the Royal Statistical Society 1951;B.
- [100] Klaus H, Oscar K. Design and Analysis of Experiments. 2nd ed. Wiley-Interscience; 2008.
- [101] Ronald WE, Raymond MH, Sharon ML, Keying Y. Probability and Statistics for Engineers & Scientists. 9th ed. Prentice Hall (Pearson); 2012.
- [102] Jiju A. Design of Experiments for Engineers and Scientists. Elsevier; 2003. doi:10.1007/s13398-014-0173-7.2.
- [103] Wahdame B, Candusso D, Francois X, Harel F, Kauffmann J, Coquery G. Design of experiment techniques for fuel cell characterisation and development. International Journal of Hydrogen Energy 2009;34:967–80. doi:10.1016/j.ijhydene.2008.10.066.
- [104] Flick S, Schwager M, McCarthy E, Mérida W. Designed experiments to characterize PEMFC material properties and performance. Applied Energy 2014;129:135–46. doi:10.1016/j.apenergy.2014.05.009.
- [105] Kahveci EE, Taymaz I. Experimental investigation on water and heat management in a PEM fuel cell using response surface methodology. International Journal of Hydrogen Energy 2014;39:10655–63. doi:10.1016/j.ijhydene.2014.04.195.
- [106] Schulze Lohoff A, Kimiaie N, Blum L. The application of design of experiments and response surface methodology to the characterization of a direct methanol fuel cell stack. International Journal of Hydrogen Energy 2016. doi:10.1016/j.ijhydene.2016.05.248.
- [107] Barari F, Morgan R, Barnard P, Tsikonis L V herle J and FD, G VL and P, N Y, et al. A Design of Experiments (DOE) approach to optimise temperature measurement accuracy in Solid Oxide Fuel Cell (SOFC). Journal of Physics: Conference Series 2014;547:012004. doi:10.1088/1742-6596/547/1/012004.
- [108] Yuan X-Z , Song C, Wang H, Zhang J. Electrochemical Impedance Spectroscopy in PEM Fuel Cells. Springer; 2010. doi:10.1007/978-1-84882-846-9.

Bibliography

- [109] Macdonald JK, Barsoukov E. Impedance Spectroscopy Theory, Experiments and Application. Wiley-Interscience; 2005. doi:10.1002/0471716243.
- [110] Lasia Andrzej. Electrochemical Impedance Spectroscopy and its Applications. Springer; 2014.
- [111] Rezaei Niya SM, Hoorfar M. On a possible physical origin of the constant phase element. *Electrochimica Acta* 2016;188:98–102. doi:10.1016/j.electacta.2015.11.142.
- [112] Jorcin JB, Orazem ME, Pébère N, Tribollet B. CPE analysis by local electrochemical impedance spectroscopy. *Electrochimica Acta* 2006;51:1473–9. doi:10.1016/j.electacta.2005.02.128.
- [113] Shoar Abouzari MR, Berkemeier F, Schmitz G, Wilmer D. On the physical interpretation of constant phase elements. *Solid State Ionics* 2009;180:922–7. doi:10.1016/j.ssi.2009.04.002.
- [114] Boudalia M, Guenbour A, Bellaouchou A, Fernandez-Domene RM, Garcia-Anton J. Corrosion behaviour of a highly alloyed austenitic alloy UB6 in contaminated phosphoric acid. *International Journal of Corrosion* 2013;2013. doi:10.1155/2013/363826.
- [115] Shoar Abouzari MR. Ion-Conductivity of Thin-Film Li-Borate Glasses. Universität Münster, 2007.
- [116] Gabriella C. Identification of electrochemical processes by frequency response analysis (Solartron analytical technical report number 004/83). 1998.
- [117] Cimenti M, Bessarabov D, Tam M, Stumper J. Investigation of Proton Transport in the Catalyst Layer of PEM Fuel Cells by Electrochemical Impedance Spectroscopy. *Economic Modelling* 2010;28.
- [118] Cruz-Manzo S, Chen R. A generic electrical circuit for performance analysis of the fuel cell cathode catalyst layer through electrochemical impedance spectroscopy. *Journal of Electroanalytical Chemistry* 2013;694:45–55. doi:10.1016/j.jelechem.2013.01.037.
- [119] Baricci A, Zago M, Casalegno A. Modelling analysis of heterogeneity of ageing in high temperature polymer electrolyte fuel cells: insight into the evolution of electrochemical impedance spectra. *Electrochimica Acta* 2016;222:596–607. doi:10.1016/j.electacta.2016.11.014.
- [120] Schneider IA, Bayer MH, von Dahlen S. Locally Resolved Electrochemical Impedance Spectroscopy in Channel and Land Areas of a Differential Polymer Electrolyte Fuel Cell. *Journal of The Electrochemical Society* 2011;158:B343. doi:10.1149/1.3536498.
- [121] Eikerling M, Kornyshev A. Electrochemical impedance of the cathode catalyst layer in polymer electrolyte fuel cells. *Journal of Electroanalytical Chemistry* 1999;475:107–23. doi:10.1016/S0022-0728(99)00335-6.
- [122] Kulikovskiy AA, Eikerling M. Analytical solutions for impedance of the cathode catalyst layer in PEM fuel cell: Layer parameters from impedance spectrum without fitting. *Journal of Electroanalytical Chemistry* 2013;691:13–7. doi:10.1016/j.jelechem.2012.12.002.

- [123] Kulikovskiy AA. Exact low-current analytical solution for impedance of the cathode catalyst layer in a PEM fuel cell. *Electrochimica Acta* 2014;147:773–7. doi:10.1016/j.electacta.2014.09.145.
- [124] Yuan X, Wang H, Colinsun J, Zhang J. AC impedance technique in PEM fuel cell diagnosis—A review. *International Journal of Hydrogen Energy* 2007;32:4365–80. doi:10.1016/j.ijhydene.2007.05.036.
- [125] Ciucci F, Chen C. Analysis of Electrochemical Impedance Spectroscopy Data Using the Distribution of Relaxation Times: A Bayesian and Hierarchical Bayesian Approach. *Electrochimica Acta* 2015;167:439–54. doi:10.1016/j.electacta.2015.03.123.
- [126] Liang H, Su H, Pollet BG, Linkov V, Pasupathi S. Membrane electrode assembly with enhanced platinum utilization for high temperature proton exchange membrane fuel cell prepared by catalyst coating membrane method. *Journal of Power Sources* 2014;266:107–13. doi:10.1016/j.jpowsour.2014.05.014.
- [127] Advent technologies n.d. www.advent-energy.com (accessed March 25, 2018).
- [128] Danish power systems n.d. <http://www.dapossy.com> (accessed March 25, 2018).
- [129] Robert M, Richard GF, James HL. *Statistical Design and Analysis of Experiments*. 2nd ed. Wiley Series in Probability and Statistics; 2003. doi:10.1007/s13398-014-0173-7.2.
- [130] Theodore AT. *Introduction to Engineering Statistics and Six Sigma*. Springer; 2006. doi:10.1198/tech.2007.s489.
- [131] Statistics How To 2018. <http://www.statisticshowto.com/normal-probability-plot/>.
- [132] Rahim Y, Janßen H, Lehnert W. Characterizing membrane electrode assemblies for high temperature polymer electrolyte membrane fuel cells using design of experiments. *International Journal of Hydrogen Energy* 2017;42:1189–202. doi:10.1016/j.ijhydene.2016.10.040.
- [133] Moore BM, Anderson R, Kay P. *Optimizing Processes with Design of Experiments*. 2013.
- [134] Mäkelä M. Experimental design and response surface methodology in energy applications: A tutorial review. *Energy Conversion and Management* 2017;151:630–40. doi:10.1016/j.enconman.2017.09.021.
- [135] Jespersen JL, Schaltz E, Kær SK. Electrochemical characterization of a polybenzimidazole-based high temperature proton exchange membrane unit cell. *Journal of Power Sources* 2009;191:289–96. doi:10.1016/j.jpowsour.2009.02.025.
- [136] fuelcellsetc 2018. <http://fuelcellsetc.com/2013/03/comparing-gas-diffusion-layers-gdl/> (accessed April 25, 2018).
- [137] Park S, Popov BN. Effect of cathode GDL characteristics on mass transport in PEM fuel cells. *Fuel* 2009;88:2068–73. doi:10.1016/j.fuel.2009.06.020.
- [138] Jiao K, Li X. Water transport in polymer electrolyte membrane fuel cells. *Progress in Energy and Combustion Science* 2011;37:221–91. doi:10.1016/j.peccs.2010.06.002.

Bibliography

- [139] Liu X, Peng F, Lou G, Wen Z. Liquid water transport characteristics of porous diffusion media in polymer electrolyte membrane fuel cells: A review. *Journal of Power Sources* 2015;299:85–96. doi:10.1016/j.jpowsour.2015.08.092.
- [140] Zamel N, Li X. Effective transport properties for polymer electrolyte membrane fuel cells - With a focus on the gas diffusion layer. *Progress in Energy and Combustion Science* 2013;39:111–46. doi:10.1016/j.pecs.2012.07.002.
- [141] Kim J, Kim M, Kang T, Sohn Y-JJ, Song T, Choi KH. Degradation modeling and operational optimization for improving the lifetime of high-temperature PEM (proton exchange membrane) fuel cells. *Energy* 2014;66:41–9. doi:10.1016/j.energy.2013.08.053.
- [142] Su H, Jao T-C, Barron O, Pollet BG, Pasupathi S. Low platinum loading for high temperature proton exchange membrane fuel cell developed by ultrasonic spray coating technique. *Journal of Power Sources* 2014;267:155–9. doi:10.1016/j.jpowsour.2014.05.086.
- [143] Darab M, Barnett AO, Lindbergh G, Thomassen MS, Sunde S. The Influence of Catalyst Layer Thickness on the Performance and Degradation of PEM Fuel Cell Cathodes with Constant Catalyst Loading. *Electrochimica Acta* 2017;232:505–16. doi:10.1016/j.electacta.2017.02.101.
- [144] Malko D, Lopes T, Ticianelli EA, Kucernak A. A catalyst layer optimisation approach using electrochemical impedance spectroscopy for PEM fuel cells operated with pyrolysed transition metal-N-C catalysts. *Journal of Power Sources* 2016;323:189–200. doi:10.1016/j.jpowsour.2016.05.035.
- [145] Maier W, Arlt T, Wannek C, Manke I, Riesemeier H, Krüger P, et al. In-situ synchrotron X-ray radiography on high temperature polymer electrolyte fuel cells. *Electrochemistry Communications* 2010;12:1436–8. doi:10.1016/j.elecom.2010.08.002.
- [146] Liu F, Mohajeri S, Di Y, Wippermann K, Lehnert W. Influence of the Interaction between Phosphoric Acid and Catalyst Layers on the Properties of HT-PEFCs. *Fuel Cells* 2014;14:750–7. doi:10.1002/fuce.201300272.
- [147] Kulikovskiy AA. How important is oxygen transport in agglomerates in a PEM fuel cell catalyst layer? *Electrochimica Acta* 2014;130:826–9. doi:10.1016/j.electacta.2014.03.131.
- [148] Seland F, Berning T, Børresen B, Tunold R. Improving the performance of high-temperature PEM fuel cells based on PBI electrolyte. *Journal of Power Sources* 2006;160:27–36. doi:10.1016/j.jpowsour.2006.01.047.
- [149] Sousa T, Mamlouk M, Scott K, Rangel CM. Three Dimensional Model of a High Temperature PEMFC. Study of the Flow Field Effect on Performance. *Fuel Cells* 2012;12:566–76. doi:10.1002/fuce.201100197.
- [150] Xu C, Scott K, Li Q, Yang J, Wu X. A Quaternary Polybenzimidazole Membrane for Intermediate Temperature Polymer Electrolyte Membrane Fuel Cells. *Fuel Cells* 2013;13:118–25. doi:10.1002/fuce.201200149.
- [151] Liu S, Rahim Y, Janßen H, Lehnert W. Study of Cathode Catalyst Layer Parameters for

- HT-PEMFC using Electrochemical Impedance Spectroscopy. *ECS Transactions*, vol. 80, 2017, p. 27–36.
- [152] Thomas RP, Acworth G. *Modern Experimental Design*. Wiley; 2007. doi:10.1198/tech.2007.s695.
- [153] Lobato J, Cañizares P, Rodrigo MA, Linares JJ, Pinar FJ. Study of the influence of the amount of PBI–H₃PO₄ in the catalytic layer of a high temperature PEMFC. *International Journal of Hydrogen Energy* 2010;35:1347–55. doi:10.1016/j.ijhydene.2009.11.091.
- [154] Khanef M, Holderer O, Ivanova O, Lüke W, Kentzinger E, Appavou MS, et al. Structure and Proton Dynamics in Catalytic Layer of HT-PEFC. *Fuel Cells* 2016. doi:10.1002/fuce.201500167.
- [155] Sebastian Kaserer, Keegan M. Caldwell, David E. Ramaker CR. Analyzing the influence of H₃PO₄ as Catalyst Poison in High Temperature PEM Fuel Cells Using in-operando X-ray Absorbption Spectroscopy. *J Phys Chem* 2013;117, 6210–6217. <http://pubs.acs.org/doi/pdf/10.1021/jp311924q> (accessed May 16, 2016).
- [156] Vilčiauskas L, Tuckerman ME, Bester G, Paddison SJ, Kreuer K-D. The mechanism of proton conduction in phosphoric acid. *Nature Chemistry* 2012;4:461–6. doi:10.1038/nchem.1329.
- [157] Kulikovskiy AA. The effect of stoichiometric ratio λ on the performance of a polymer electrolyte fuel cell. *Electrochimica Acta* 2004;49:617–25. doi:10.1016/j.electacta.2003.09.016.
- [158] Kim JR, Yi JS, Song TW. Investigation of degradation mechanisms of a high-temperature polymer-electrolyte-membrane fuel cell stack by electrochemical impedance spectroscopy. *Journal of Power Sources* 2012;220:54–64. doi:10.1016/j.jpowsour.2012.07.129.
- [159] Maier W, Arlt T, Wippermann K, Wannek C, Manke I, Lehnert W, et al. Correlation of Synchrotron X-ray Radiography and Electrochemical Impedance Spectroscopy for the Investigation of HT-PEFCs. *Journal of the Electrochemical Society* 2012;159:F398–404. doi:10.1149/2.024208jes.
- [160] Kulikovskiy AA. A physical model for catalyst layer impedance. *Journal of Electroanalytical Chemistry* 2012;669:28–34. doi:10.1016/j.jelechem.2012.01.018.
- [161] Zhang J, Zhang H, Wu J, Zhang J. *Techniques for PEM Fuel Cell Testing and Diagnosis. Pem Fuel Cell Testing and Diagnosis*, Elsevier; 2013, p. 81–119. doi:10.1016/B978-0-444-53688-4.00003-6.
- [162] Schonvogel D, Rastedt M, Wagner P, Wark M, Dyck A. Impact of Accelerated Stress Tests on High Temperature PEMFC Degradation. *Fuel Cells* 2016;16:480–9. doi:10.1002/fuce.201500160.
- [163] Wippermann K, Wannek C, Oetjen HF, Mergel J, Lehnert W. Cell resistances of poly(2,5-benzimidazole)-based high temperature polymer membrane fuel cell membrane electrode assemblies: Time dependence and influence of operating parameters. *Journal of Power Sources* 2010;195:2806–9. doi:10.1016/j.jpowsour.2009.10.100.

Bibliography

- [164] Mack F, Galbiati S, Gogel V, J  rissen L, Zeis R. Evaluation of Electrolyte Additives for High-Temperature Polymer Electrolyte Fuel Cells. *ChemElectroChem* 2016;3:770–3. doi:10.1002/celc.201500561.
- [165] Larminie. James. *Fuel Cell Systems Explained*. Wiley; 2003.
- [166] Kulikovskiy AA. Analytical Solutions for Polarization Curve and Impedance of the Cathode Catalyst Layer with Fast Oxygen Transport in a PEM Fuel Cell. *Journal of the Electrochemical Society* 2014;161:E3171–9. doi:10.1149/2.020408jes.
- [167] Kulikovskiy AA. A simple equation for in situ measurement of the catalyst layer oxygen diffusivity in PEM fuel cell. *Journal of Electroanalytical Chemistry* 2014;720–721:47–51. doi:10.1016/j.jelechem.2014.03.005.
- [168] Zhou F, Simon Araya S, Florentina Grigoras I, Juhl Andreasen S, Knudsen K  r S. Performance Degradation Tests of Phosphoric Acid Doped Polybenzimidazole Membrane Based High Temperature Polymer Electrolyte Membrane Fuel Cells. *Journal of Fuel Cell Science and Technology* 2015;12:21002. doi:10.1115/1.4029081.
- [169] Kondratenko MS, Gallyamov MO, Khokhlov AR. Performance of high temperature fuel cells with different types of PBI membranes as analysed by impedance spectroscopy. *International Journal of Hydrogen Energy* 2012;37:2596–602. doi:10.1016/j.ijhydene.2011.10.087.
- [170] Asensio JA, S  nchez EM, G  mez-Romero P. Proton-conducting membranes based on benzimidazole polymers for high-temperature PEM fuel cells. A chemical quest. *Chemical Society Reviews* 2010;39:3210. doi:10.1039/b922650h.
- [171] Schmidt TJ. High-Temperature Polymer Electrolyte Fuel Cells: Durability Insights. In: B  chi FN, Inaba M, Schmidt TJ, editors. *Polymer Electrolyte Fuel Cell Durability*, New York, NY: Springer New York; 2009, p. 199–221. doi:10.1007/978-0-387-85536-3_9.
- [172] Celtec MEAs: Membrane Electrode Assemblies for High Temperature PEM Fuel Cells. 2010.
- [173] Kannan A, Kaczerowski J, Kabza A, Scholta J. Operation Strategies Based on Carbon Corrosion and Lifetime Investigations for High Temperature Polymer Electrolyte Membrane Fuel Cell Stacks. *Fuel Cells* 2018;1–12. doi:10.1002/fuce.201700096.
- [174] Engl T, Gubler L, Schmidt TJ. Think different! Carbon corrosion mitigation strategy in high temperature PEFC: A rapid aging study. *Journal of the Electrochemical Society* 2015;162:F291–7. doi:10.1149/2.0681503jes.
- [175] de Beer C, Barendse P, Pillay P, Bullecks B, Rengaswamy R. Degradation of high temperature PEM fuel cells and the impact on electrical performance. 2013 IEEE International Conference on Industrial Technology (ICIT) 2013:690–4. doi:10.1109/ICIT.2013.6505755.
- [176]   beda D, Ca  nizares P, Rodrigo MA, Pinar FJ, Lobato J. Durability study of HTPeMFC through current distribution measurements and the application of a model. *International Journal of Hydrogen Energy* 2014;39:21678–87. doi:10.1016/j.ijhydene.2014.06.045.

- [177] Thomas S, Jeppesen C, Steenberg T, Araya SS, Vang JR, Kær SK. New load cycling strategy for enhanced durability of high temperature proton exchange membrane fuel cell. *International Journal of Hydrogen Energy* 2017;42:27230–40. doi:10.1016/j.ijhydene.2017.09.018.
- [178] Maier W, Arlt T, Wippermann K, Wannek C, Manke I, Lehnert W, et al. Correlation of Synchrotron X-ray Radiography and Electrochemical Impedance Spectroscopy for the Investigation of HT-PEFCs. *Journal of the Electrochemical Society* 2012;159:F398–404. doi:10.1149/2.024208jes.
- [179] Conti F, Majerus A, Di Noto V, Korte C, Lehnert W, Stolten D. Raman study of the polybenzimidazole–phosphoric acid interactions in membranes for fuel cells. *Physical Chemistry Chemical Physics* 2012;14:10022. doi:10.1039/c2cp40553a.
- [180] Paasch G, Micka K, Gersdore P. Theory of the Electrochemical Impedance of anomalous diffusion. *Journal of Electroanalytical Chemistry* 2001;499:112–20.
- [181] Zhang Y, Chen S, Wang Y, Ding W, Wu R, Li L, et al. Study of the degradation mechanisms of carbon-supported platinum fuel cells catalyst via different accelerated stress test. *Journal of Power Sources* 2015;273:62–9. doi:10.1016/j.jpowsour.2014.09.012.
- [182] Gasteiger H, Mathias M. Fundamental research and development challenges in polymer electrolyte fuel cell technology. General Motors Corporation – Fuel Cell Activities, 2002.
- [183] Weber AZ. Gas-Crossover and Membrane-Pinhole Effects in Polymer-Electrolyte Fuel Cells. *Journal of The Electrochemical Society* 2008;155:B521. doi:10.1149/1.2898130.
- [184] Lin HL, Yu TL, Chang WK, Cheng CP, Hu CR, Jung G Bin. Preparation of a low proton resistance PBI/PTFE composite membrane. *Journal of Power Sources* 2007;164:481–7. doi:10.1016/j.jpowsour.2006.11.036.
- [185] Qi Z, Buelte S. Effect of open circuit voltage on performance and degradation of high temperature PBI-H₃PO₄ fuel cells. *Journal of Power Sources* 2006;161:1126–32. doi:10.1016/j.jpowsour.2006.06.020.
- [186] Yu S, Xiao L, Benicewicz BC. Durability Studies of PBI-based High Temperature PEMFCs. *Fuel Cells* 2008;8:165–74. doi:10.1002/fuce.200800024.
- [187] Al-Hadeethi F, Al-Nimr M, Al-Safadi M. Using the multiple regression analysis with respect to ANOVA and 3D mapping to model the actual performance of PEM (proton exchange membrane) fuel cell at various operating conditions. *Energy* 2015. doi:10.1016/j.energy.2015.07.074.
- [188] Guvelioglu GH, Stenger HG. Main and interaction effects of PEM fuel cell design parameters. *Journal of Power Sources* 2006;156:424–33. doi:10.1016/j.jpowsour.2005.06.009.
- [189] DANTE R, ESCAMILLA J, MADRIGAL V, THEUSS T, DEDIOSCALDERON J, SOLORZA O, et al. Fractional factorial design of experiments for PEM fuel cell performances improvement. *International Journal of Hydrogen Energy* 2003;28:343–8. doi:10.1016/S0360-3199(02)00069-1.

Bibliography

- [190] Carton JG, Olabi AG. Design of experiment study of the parameters that affect performance of three flow plate configurations of a proton exchange membrane fuel cell. *Energy* 2010;35:2796–806. doi:10.1016/j.energy.2010.02.044.
- [191] Lüke L, Janßen H, Kvesić M, Lehnert W, Stolten D. Performance analysis of HT-PEFC stacks. *International Journal of Hydrogen Energy* 2012;37:9171–81. doi:10.1016/j.ijhydene.2012.02.190.
- [192] Janßen H, Supra J, Lüke L, Lehnert W, Stolten D. Development of HT-PEFC stacks in the kW range. *International Journal of Hydrogen Energy* 2013;38:4705–13. doi:10.1016/j.ijhydene.2013.01.127.
- [193] Lebak J, Ali ST, Møller P, Mathiasen C, Nielsen LP, Kær SK. Quantification of in situ temperature measurements on a PBI-based high temperature PEMFC unit cell. *International Journal of Hydrogen Energy* 2010;35:9943–53. doi:10.1016/j.ijhydene.2009.10.002.
- [194] Rabjerg J. HTPeM fuel cell impedance. Aalborg University, 2014.
- [195] Oono Y, Sounai A, Hori M. Long-term cell degradation mechanism in high-temperature proton exchange membrane fuel cells. *Journal of Power Sources* 2012;210:366–73. doi:10.1016/j.jpowsour.2012.02.098.
- [196] Jeon Y, Juon S me, Hwang H, Park J, Shul Y. Accelerated Life-time Tests including Different Load Cycling Protocols for High Temperature Polymer Electrolyte Membrane Fuel Cells. *Electrochimica Acta* 2014;148:15–25. doi:10.1016/j.electacta.2014.10.025.
- [197] Rastedt M, Tullius V, Büsselmann J, Schonvogel D, Wagner P, Dy. Evaluation of HT-PEM Fuel Cells via Load Cycling at High Current Densities. *ECS Transactions* 2017;80:3–17.
- [198] Oono Y, Fukuda T, Sounai A, Hori M. Influence of operating temperature on cell performance and endurance of high temperature proton exchange membrane fuel cells. *Journal of Power Sources* 2010;195:1007–14. doi:10.1016/j.jpowsour.2009.08.097.
- [199] Zeis R. Materials and characterization techniques for high-temperature polymer electrolyte membrane fuel cells. *Beilstein Journal of Nanotechnology* 2015;6:68–83. doi:10.3762/bjnano.6.8.
- [200] Oono Y, Sounai A, Hori M. Influence of the phosphoric acid-doping level in a polybenzimidazole membrane on the cell performance of high-temperature proton exchange membrane fuel cells. *Journal of Power Sources* 2009;189:943–9. doi:10.1016/j.jpowsour.2008.12.115.
- [201] BASF 2018. https://www.basf.com/documents/de/about-us/Companies/new-business-gmbh/publications/e-power-management/Celtec_Membrane.pdf.
- [202] Elcore n.d. www.elcore.de (accessed May 31, 2016).
- [203] Breitwieser M, Klingele M, Britton B, Holdcroft S, Zengerle R, Thiele S. Improved Pt-utilization efficiency of low Pt-loading PEM fuel cell electrodes using direct membrane

- deposition. *Electrochemistry Communications* 2015;60:168–71.
doi:10.1016/j.elecom.2015.09.006.
- [204] Kulikovskiy A. Why impedance of the gas diffusion layer in a PEM fuel cell differs from the Warburg finite-length impedance? *Electrochemistry Communications* 2017;84:28–31.
doi:10.1016/j.elecom.2017.09.014.
- [205] Kulikovskiy A. Impedance of a PEM fuel cell cathode with nonuniform ionomer loading: Analytical and numerical study. *Journal of Electroanalytical Chemistry* 2017;789:174–80.
doi:10.1016/j.jelechem.2017.02.029.
- [206] Kulikovskiy AA. Analytical physics-based impedance of the cathode catalyst layer in a PEM fuel cell at typical working currents. *Electrochimica Acta* 2017;225:559–65.
doi:10.1016/j.electacta.2016.11.129.
- [207] Reshetenko T, Kulikovskiy A. Impedance Spectroscopy Characterization of Oxygen Transport in Low- and High-Pt Loaded PEM Fuel Cells. *Journal of The Electrochemical Society* 2017;164:F1633–40. doi:10.1149/2.1131714jes.
- [208] Fouquet N, Doulet C, Nouillant C, Dauphin-Tanguy G, Ould-Bouamama B. Model based PEM fuel cell state-of-health monitoring via ac impedance measurements. *Journal of Power Sources* 2006;159:905–13. doi:10.1016/j.jpowsour.2005.11.035.
- [209] Giner-Sanz JJ, Ortega EM, Perez Herranz V. Optimization of the electrochemical impedance spectroscopy measurement parameters for PEM fuel cell spectrum determination. *Electrochimica Acta* 2015;174:1290–8.
doi:10.1016/j.electacta.2015.06.106.
- [210] Chandresris M, Robin C, Gerard M, Bultel Y. Investigation of the difference between the low frequency limit of the impedance spectrum and the slope of the polarization curve. *Electrochimica Acta* 2015;180:581–90. doi:10.1016/j.electacta.2015.08.089.
- [211] Siegel C, Buder I, Heinzel A. Sectional electrochemical impedance analysis of a high temperature polymer electrolyte membrane fuel cell with three types of flow-fields. *Electrochimica Acta* 2013;112:342–55. doi:10.1016/j.electacta.2013.08.142.
- [212] Kulikovskiy AA. PEM Fuel Cell Impedance at Open Circuit. *Journal of The Electrochemical Society* 2016;163:F319–26. doi:10.1149/2.0111605jes.
- [213] Shamardina O, Kulikovskiy AA, Chertovich A V., Khokhlov AR. A Model for High-Temperature PEM Fuel Cell: The Role of Transport in the Cathode Catalyst Layer. *Fuel Cells* 2012;12:577–82. doi:10.1002/fuce.201100144.
- [214] Kulikovskiy AA. Polarization curve of a PEM fuel cell with the account of a finite rate of oxygen adsorption on Pt surface. *International Journal of Hydrogen Energy* 2014;39:19018–23. doi:10.1016/j.ijhydene.2014.08.108.
- [215] Kulikovskiy AA. A simple physics-based equation for low-current impedance of a PEM fuel cell cathode. *Electrochimica Acta* 2016. doi:10.1016/j.electacta.2016.02.150.
- [216] Kulikovskiy AA. A simple and accurate fitting equation for half of the faradaic impedance

Bibliography

- arc of a PEM fuel cell. *Journal of Electroanalytical Chemistry* 2015;738:108–12.
doi:10.1016/j.jelechem.2014.11.010.
- [217] Kulikovskiy AA. The regimes of catalyst layer operation in a fuel cell. *Electrochimica Acta* 2010;55:6391–401. doi:10.1016/j.electacta.2010.06.053.
- [218] Reshetenko T, Kulikovskiy A. PEM Fuel Cell Characterization by Means of the Physical Model for Impedance Spectra. *Journal of the Electrochemical Society* 2015;162:F627–33. doi:10.1149/2.1141506jes.

List of Figures

Figure 1.1: Working principle of a PEFC	3
Figure 1.2: A typical polarization curve for a PEFC with regions of each dominant loss indicated	6
Figure 1.3: Exploded view of a PEFC single cell at IEK-3	7
Figure 2.1: OFAT and DoE; comparison of experimental effort	14
Figure 2.2: Typical steps for conducting a classical DoE procedure	16
Figure 2.3: Design points for a 2 level 2 factor full factorial DoE.....	17
Figure 2.4: Comparison of an insignificant (left) and significant (right) interaction of pressure and temperature.....	19
Figure 2.5: Measurement principle of fuel cell impedance.....	21
Figure 2.6: a) series connection of impedances b) parallel connection of impedances	22
Figure 2.7: Representation of impedance data in the form of Nyquist (a) and Bode (b) plots	23
Figure 2.8: Schematic of EIS data analysis with ECM and the physical domains modelled in the low cathode λ , high current density (bottom) and the high cathode λ , low current density (top) regimes with pure H_2 on the anode side for both cases.....	24
Figure 2.9: Schematic depicting the variations in the O_2 and protonic concentrations and the local activation loss in the CCL for high cathode λ and low current density operation redrawn from [123].	26
Figure 3.1: a) A stainless steel endplate, graphitic flowplate, PFA gasket and commercial MEA for the single cells b) In-house assembled single cell	29
Figure 3.2: a) Left: Freudenberg H2315C2 GDL Right: PBI based membrane (AM-55) from FUMA-Tech, Germany b) An in-house assembled MEA with PFA gasket.....	30
Figure 3.3: Exploded view of a single cell at IEK-3.....	31
Figure 3.4: Break-in procedure and typical testing of a single cell.....	32
Figure 3.5: UI curve procedure for a single cell.....	33
Figure 3.6: The test station for single cell testing	34
Figure 3.7: Simplified flow diagram of the single cell test station used for the experiments	35
Figure 3.8: Single cell installed in the test station for testing, co-flow configuration	36
Figure 4.1: Normal probability plot for main effects and factor interactions for Daposity MEA (n=5) (Redrawn from [132])	46
Figure 4.2: Normal probability plot of residuals for Daposity MEA (Redrawn from [132]).....	48
Figure 4.3: Comparison of intercepts (Redrawn from [132])	49
Figure 4.4: Comparison of current density coefficient (I) (Redrawn from [132])	50
Figure 4.5: Comparison of cathode λ coefficient (C) (Redrawn from [132])	50
Figure 4.6: Comparison of temperature coefficient (T) (Redrawn from [132]).....	51
Figure 4.7: Comparison of current density and temperature interaction (I *T) (Redrawn from [132]).....	51
Figure 4.8: BOL and EOL UI curve comparison for MEA A at 160°C with anode/cathode λ of 2/2.....	52

List of Figures

Figure 4.9: BOL and EOL UI curve comparison for MEA B at 160°C with anode/cathode λ of 2/2	53
Figure 4.10: BOL and EOL UI curve comparison for MEA C at 160°C with anode/cathode λ of 2/2	53
Figure 4.11: BOL and EOL UI curve comparison for MEA D at 160°C with anode/cathode λ of 2/2	54
Figure 5.1: Pareto chart for 200mA cm ⁻² and anode/cathode λ of 2/2, T= 160°C	62
Figure 5.2: Contour plots of desirability for 200mA cm ⁻² and anode/cathode λ of 2/2, T= 160°C	64
Figure 5.3: Pareto chart for 400mA cm ⁻² and anode/cathode λ of 2/2, T= 160°C	65
Figure 5.4: Contour plots of desirability for 400mA cm ⁻² and anode/cathode λ of 2/2, T= 160°C	66
Figure 5.5: Pareto chart for 600mA cm ⁻² and anode/cathode λ of 2/2, T= 160°C	67
Figure 5.6: Contour plots of desirability for 600mA cm ⁻² and anode/cathode λ of 2/2, T= 160°C	68
Figure 5.7: Pareto chart for 200mA cm ⁻² and anode/cathode λ of 2/6, T= 160°C	69
Figure 5.8: Contour plots of desirability for 200mA cm ⁻² and anode/cathode λ of 2/6, T= 160°C	70
Figure 5.9: Pareto chart for 400mA cm ⁻² and anode/cathode λ of 2/6, T= 160°C	71
Figure 5.10: Contour plots of desirability for 400mA cm ⁻² and anode/cathode λ of 2/6, T= 160°C	72
Figure 5.11: Pareto chart for 600mA cm ⁻² and anode/cathode λ of 2/6, T= 160°C	73
Figure 5.12: Contour plots of desirability for 600mA cm ⁻² and anode/cathode λ of 2/6, T= 160°C	74
Figure 5.13: PADL and Pt loading interaction (AB) comparison for anode/cathode λ of 2/2	75
Figure 5.14: PADL and Pt loading interaction (AB) comparison for anode/cathode λ of 2/6	76
Figure 5.15: Pt loading and CCL thickness interaction (BC) comparison for anode/cathode λ of 2/2	77
Figure 5.16: Pt loading and CCL thickness interaction (BC) comparison for anode/cathode λ of 2/6	78
Figure 5.17: PADL and CCL thickness interaction (AC) comparison for anode/cathode λ of 2/2	79
Figure 5.18: PADL and CCL thickness interaction (AC) comparison for anode/cathode λ of 2/6	80
Figure 5.19: UI Curve comparison for all the MEAs immediately after the break-in procedure, operating conditions: λ (An (H ₂)/Ca (Air)) = 2/6 for current densities higher than 200mA cm ⁻² (below 200mA cm ⁻² , the gas flowrate for λ = 2/6 at 200mA cm ⁻² is maintained) T = 160°C (See Table 5.2 for MEA specifications)	83
Figure 5.20: Nyquist plot of MEA7 for the selected current densities and stoichiometries as shown in Table 5.7.	83
Figure 5.21: Ohmic resistance (R_{Ω}) values of all MEAs from ECM fitting of EIS data	84
Figure 5.22: Protonic resistance (R_p) values of all MEAs from ECM fitting of EIS data	85
Figure 5.23: Activation resistance (R_{act}) values of all MEAs from ECM fitting of EIS data	86
Figure 5.24: Double layer capacitance (C_{dl}) values of all MEAs from ECM fitting of EIS data	87
Figure 5.25: Total DC resistance (R_{dc}) values of all MEAs from ECM fitting of EIS data	88
Figure 6.1: UI curves for single cell with varying hydrogen concentration on the anode side, cathode gas: air, anode/cathode λ = 2/6, T= 160°C	90

Figure 6.2: Nyquist plots for different anode gas concentrations for 50mA cm ⁻² anode/cathode $\lambda = 8/24$, T= 160°C.....	91
Figure 6.3: : Nyquist plots for different anode gas concentrations for 100mA cm ⁻² anode/cathode $\lambda = 4/12$, T= 160°C.....	92
Figure 6.4: UI curves for single cell with varying hydrogen concentration on the anode side, cathode gas: oxygen, anode/cathode $\lambda = 2/6$, T= 160°C	93
Figure 6.5: Nyquist plots for different anode gas concentrations for 50mA cm ⁻² anode/cathode $\lambda = 8/24$, T= 160°C.....	94
Figure 6.6: Nyquist plots for different anode gas concentrations for 100mA cm ⁻² anode/cathode $\lambda = 4/12$, T= 160°C.....	94
Figure 6.7: UI curves for single cell with varying oxygen concentration on the cathode side, Anode gas: hydrogen, anode/cathode $\lambda = 2/6$, T= 160°C.....	95
Figure 6.8: Nyquist plots for different cathode gas concentration for 50mA cm ⁻² anode/cathode $\lambda = 8/24$, T= 160°C.....	96
Figure 6.9: Nyquist plots for different cathode gas concentration for 100mA cm ⁻² anode/cathode $\lambda = 4/12$, T= 160°C.....	96
Figure 6.10: Comparison of R_p for increasing hydrogen content in the fuel stream, anode/cathode $\lambda = 8/24$ (left) and 4/12 (right), T= 160°C.....	97
Figure 6.11: Comparison of R_{act} for increasing hydrogen content in the fuel stream, anode/cathode $\lambda = 8/24$ (left) and 4/12 (right), T= 160°C.....	98
Figure 6.12: Comparison of C_{dl} for increasing hydrogen content in the fuel stream, anode/cathode $\lambda = 8/24$ (left) and 4/12 (right), T= 160°C.....	98
Figure 6.13: R_{oxp} (as calculated by AM) with increasing hydrogen content in the fuel stream, anode/cathode $\lambda = 8/24$ (left) and 4/12 (right), T= 160°C.....	99
Figure 6.14: R_{Ω} as calculated by ECM with increasing hydrogen content in the fuel stream, anode/cathode $\lambda = 8/24$ (left) and 4/12 (right), T= 160°C.....	100
Figure 6.15: Comparison of R_{dc} for increasing hydrogen content in the fuel stream, anode/cathode $\lambda = 8/24$ (left) and 4/12 (right), T= 160°C.....	100
Figure 6.16: Comparison of R_p for increasing hydrogen content in the fuel stream (O ₂ on cathode side), anode/cathode $\lambda = 8/24$ (left) and 4/12 (right), T= 160°C.....	101
Figure 6.17: Comparison of R_{act} for increasing hydrogen content in the fuel stream (O ₂ on cathode side), anode/cathode $\lambda = 8/24$ (left) and 4/12 (right), T= 160°C	101
Figure 6.18: Comparison of C_{dl} for increasing hydrogen content in the fuel stream (O ₂ on cathode side), anode/cathode $\lambda = 8/24$ (left) and 4/12 (right), T= 160°C.....	102
Figure 6.19: R_{oxp} (as calculated by AM) with increasing hydrogen content in the fuel stream (O ₂ on cathode side), anode/cathode $\lambda = 8/24$ (left) and 4/12 (right), T= 160°C	102
Figure 6.20: R_{Ω} (as calculated by ECM) with increasing hydrogen content in the fuel stream (O ₂ on cathode side), anode/cathode $\lambda = 8/24$ (left) and 4/12 (right), T= 160°C	102
Figure 6.21: Comparison of R_{dc} for increasing hydrogen content in the fuel stream (O ₂ on cathode side), anode/cathode $\lambda = 8/24$ (left) and 4/12 (right), T= 160°C.....	103
Figure 6.22: Comparison of R_p for increasing oxygen content in the cathode gas, anode/cathode λ $= 8/24$ (left) and 4/12 (right), T= 160°C.....	103

List of Figures

Figure 6.23: Comparison of R_{act} for increasing oxygen content in the cathode gas, anode/cathode $\lambda = 8/24$ (left) and $4/12$ (right), $T = 160^\circ\text{C}$	104
Figure 6.24: Comparison of C_{dl} for increasing oxygen content in the cathode gas, anode/cathode $\lambda = 8/24$ (left) and $4/12$ (right), $T = 160^\circ\text{C}$	104
Figure 6.25: R_{oxp} (as calculated by AM) with increasing oxygen content in the cathode gas, anode/cathode $\lambda = 8/24$ (left) and $4/12$ (right), $T = 160^\circ\text{C}$	105
Figure 6.26: R_{Ω} (as calculated by ECM) with increasing oxygen content in the cathode gas, anode/cathode $\lambda = 8/24$ (left) and $4/12$ (right), $T = 160^\circ\text{C}$	105
Figure 6.27: Comparison of R_{dc} for increasing oxygen content in the cathode gas, anode/cathode $\lambda = 8/24$ (left) and $4/12$ (right), $T = 160^\circ\text{C}$	106
Figure 6.28: Comparison of the predicted values of R_{oxp} by the suggested ECM with AM values for increasing hydrogen content on the anode side with pure oxygen on the cathode side and anode/cathode λ of $8/24$ (left) and $4/12$ (right). $T = 160^\circ\text{C}$	107
Figure 6.29: Comparison of the predicted values of R_{oxp} by the suggested ECM with AM values for increasing oxygen content on the cathode side with hydrogen on the anode side and anode/cathode λ of $8/24$ (left) and $4/12$ (right). $T = 160^\circ\text{C}$	108
Figure 7.1: Ut curves for constant current density operation for 100 hours of the three Advent MEAs. Operating conditions: current density: 0.2A cm^{-2} , anode λ : 2 (gas: H_2), cathode λ : 2 (gas: air), $T = 160^\circ\text{C}$	112
Figure 7.2: BOL averaged UI curves for the three MEAs, anode/cathode $\lambda = 2/2$, $T = 160^\circ\text{C}$	113
Figure 7.3: EOL averaged UI curves for the three MEAs, anode/cathode $\lambda = 2/2$, $T = 160^\circ\text{C}$	113
Figure 7.4: Degradation rates (voltage loss over time) of the three MEAs as a function of current density, anode/cathode $\lambda = 2/2$, $T = 160^\circ\text{C}$	114
Figure 7.5: Comparison of EOL UI curves after different stress modes (AAM MEA, anode/cathode $\lambda = 2/2$ $T = 160^\circ\text{C}$).....	115
Figure 7.6: Comparison of EOL degradation rates for stressors (AAM MEA, anode/cathode $\lambda = 2/2$, $T = 160^\circ\text{C}$).....	116
Figure 7.7: Comparison of EOL UI curves after different stress modes (APM MEA, anode/cathode $\lambda = 2/2$, $T = 160^\circ\text{C}$).....	117
Figure 7.8: Comparison of EOL degradation rates for stressors (APM MEA, anode/cathode $\lambda = 2/2$, $T = 160^\circ\text{C}$).....	118
Figure 7.9: Comparison of the EOL ohmic resistance (R_{Ω}), current density = 200mA cm^{-2} , anode/cathode $\lambda = 2/2$	119
Figure 7.10: Comparison of the EOL activation resistance (R_{act}), current density = 200mA cm^{-2} , anode/cathode $\lambda = 2/2$	120
Figure 7.11: Comparison of the EOL protonic resistance (R_p), current density = 200mA cm^{-2} , anode/cathode $\lambda = 2/2$	121
Figure 7.12: Comparison of the EOL mass transport resistance (R_m), current density = 200mA cm^{-2} , anode/cathode $\lambda = 2/2$	122
Figure 7.13: Comparison of the EOL double layer capacitance (C_{dl}), current density = 200mA cm^{-2} , anode/cathode $\lambda = 2/2$	123
Figure 7.14: Comparison of the EOL electrochemical surface area (ECSA).....	124

List of Tables

Table 1.1: Major types of fuel cells with their properties and application areas	2
Table 2.1: OFAT experimental design for two factors	17
Table 2.2: A 2 Level full factorial DoE for two factors	17
Table 2.3: Basic electrical elements with their voltage and current relation and ideal impedances	22
Table 2.4: Elements used to fit the impedance data in the two ECMs with the physical parameters they are used to model.....	25
Table 3.1: Measurement equipment and their range and accuracy (Source: Test station manual) 36	
Table 3.2: Important specifications of the Zahner Zennium workstation used for EIS measurements (Source: Zahner product catalog)	37
Table 3.3: Important specifications of the PP241 power potentiostat used for EIS measurements (Source: Zahner product catalog)	37
Table 4.1: Commercial HT-PEFC MEA information	41
Table 4.2: List of factors and their investigated levels.....	42
Table 4.3: Design matrix for a 2 level four factor (2^4) DoE with middle points	42
Table 4.4: Calculation of average cell voltage for Daposity MEA (n=5)	43
Table 4.5: Yates algorithm for calculation of main effects and interactions for Daposity MEA	44
Table 4.6: Comparison of middle point standard deviation for Daposity MEA	44
Table 4.7: Normal probability calculation table for Daposity MEA	45
Table 4.8: Main effects and interactions with their statistical significance for Daposity MEA (n=5)	46
Table 4.9: Transformation of factors to a range of -1 to 1	47
Table 4.10: Comparison of predicted and measured cell voltages at selected points for MEA D.47	
Table 4.11: Degradation rates for all MEAs at current densities upto 0.6A cm^{-2}	54
Table 5.1: Considered factors with their respective ranges.....	58
Table 5.2: MEA IDs and their factor levels	58
Table 5.3: Cathode catalyst layer recipes and spacer thicknesses used for GDE preparation (Reprinted with permission from [151], Copyright [2017], The Electrochemical Society.)	59
Table 5.4: Ratios (by weight) of PTFE, Pt/C catalyst and additional carbon in the CCL of each MEA	60
Table 5.5: Cell voltage at selected current densities for anode/cathode λ of 2/2, T= 160°C	61
Table 5.6: Cell voltage at selected current densities for anode/cathode λ of 2/6, T= 160°C	61
Table 5.7: Stoichiometries of the anode and cathode sides for the impedance measurements	82
Table 6.1: Different gas concentrations used for the anode and cathode side	89
Table 7.1: List of commercial MEAs from Advent technologies [®] used for degradation testing.110	
Table 7.2: Used stressors, their ranges, implementation modes and dominant degradation modes	111

Acknowledgments

First of all, I would like to thank Allah, the almighty, for giving me the strength and ability to perform this monumental task.

There are many people I would like to thank at the end of my stay at IEK-3 as a PhD student. First and foremost, my heartfelt thanks go to my PhD supervisor Prof. Dr. Werner Lehnert. It would never have been possible to achieve this without his constant support and encouragement. He has been a beacon of light and a source of inspiration throughout my PhD studies. He was always full of innovative ideas, patient and to the point in the many fruitful discussions we had.

I would also like to thank my group leader Dr. Holger Janßen. I still remember my early days at the institute when I had little knowledge about fuel cells and Holger would listen to my basic questions very patiently and then discuss in great detail until the matter was clear. I have learned a lot from him and found him to be very knowledgeable, practical, and flexible as the group leader. He also very kindly agreed to read my thesis on a chapter by chapter basis, which helped me a great deal in improving my writing style for future chapters from the immediate feedback I received from him.

I would also like to say a special thanks to Dr. Klaus Wippermann and Prof. Andrei Kulikovskiy for most valuable discussions about EIS measurements and modelling. I always valued and appreciated their input and comments and found them very helpful. My thanks also go to Dr. Remzi Can Samsun and Dr. Uwe Reimer for very helpful discussions. I also want to thank all the people in my group, especially Birgit Schumacher for all the help she gave me during my experimental work; it really would not have been possible to complete my experimental work without her extensive help.

I also want to thank all my colleagues at IEK-3, especially the PhD students. My sincere thanks go to Bhunesh Kumar, Vitali Weißbecker, Maximilian Schalenbach, Manuel Langemann, Alexander Otto, Geert Tjarks, Daniel Krekel, Maximilian Engelbracht, Michael Höh, Qing Cao, Huijie Zhang, Mathias Frank, Yu Lin, Junliang Yu, Shuai Liu, Shidong Zhang, Philipp Irmscher, Eugen Hoppe, Stefan Schemme, Severin Ryberg, Yan Yulin, Michael Hehemann, Jannik Ehlert, Walter Zwaygardt, Rabah Lekehal, Mathias Prawitz, Bernd Pelzer, Thomas Pütz, Nadja, Manuel and many others who helped me at various points during my studies. I really appreciate your help, feedback, suggestions and cooperation.

Last but not the least; I would like to thank my parents, my wife and my kids for being very supportive and patient during my four years away from home. I will never be able to pay you back for this.

Finally, I would like to thank the higher education commission (HEC) of Pakistan for the financial support which made this research possible. My thanks also go to the German

Acknowledgments

educational exchange service (DAAD), which organized everything to perfection during my stay in Germany.

Band / Volume 424

**Synthesis and Stability Assessment of Uranium Microparticles:
Providing Reference Materials for Nuclear Verification Purposes**

R. Middendorp (2018), X, 145 pp

ISBN: 978-3-95806-330-3

Band / Volume 425

**Herstellung und Charakterisierung von Lithiumlanthanzirkonat-
Funktionsschichten für Lithium-Festkörperbatterien**

T. Reppert (2018), vii, 187 pp

ISBN: 978-3-95806-331-0

Band / Volume 426

**Proton Conduction and Gas Permeation through Polymer Electrolyte
Membranes during Water Electrolysis**

M. Schalenbach (2018), VI, 212 pp

ISBN: 978-3-95806-333-4

Band / Volume 427

**Improved characterization of root zone soil moisture by assimilating
groundwater level and surface soil moisture data in an integrated
terrestrial system model**

H. Zhang (2018), x, 125 pp

ISBN: 978-3-95806-335-8

Band / Volume 428

**Manipulation of magnetism in iron oxide nanoparticle / BaTiO₃
composites and low-dimensional iron oxide nanoparticle arrays**

L. Wang (2018), VI, 151 pp

ISBN: 978-3-95806-338-9

Band wurde nicht veröffentlicht. Erscheint als Schlüsseltechnologieband 180

Band / Volume 429

**Characterization of spatial-temporal varying riverbed hydraulic
conductivity and its role on the estimation of river-aquifer
exchange fluxes with data assimilation**

Q. Tang (2018), xv, 117 pp

ISBN: 978-3-95806-339-6

Band / Volume 430

**Der Einfluss von Wasserdampf auf den Sauerstofftransport
in keramischen Hochtemperaturmembranen**

F. Thaler (2018), ii, 93, XXXI pp

ISBN: 978-3-95806-340-2

Band / Volume 431

**Analysis & modeling of metastable photovoltaic technologies:
towards dynamic photovoltaic performance models**

M. Görig (2018), 246 pp

ISBN: 978-3-95806-342-6

Band / Volume 432

Laser Treatment of Silicon Thin-Films for Photovoltaic Applications

C. Maurer (2018), vii, 165 pp

ISBN: 978-3-95806-347-1

Band / Volume 433

Mentalitäten und Verhaltensmuster im Kontext der Energiewende in NRW

K. Schürmann & D. Schumann (Hrsg.) (2018), 236 pp

ISBN: 978-3-95806-349-5

Band / Volume 434

**Adhäsionsverhalten von wässrigen Nafion-Lösungen an
dispersen Phasengrenzen**

A. Schulz (2018), xii, 129 pp

ISBN: 978-3-95806-354-9

Band / Volume 435

**Alterungs- und fehlertolerante optimale Betriebsführung
eines Direktmethanol-Brennstoffzellensystems**

R. Keller (2018), XX, 175 pp

ISBN: 978-3-95806-355-6

Band / Volume 436

**Chamber study of biogenic volatile organic compounds:
plant emission, oxidation products and their OH reactivity**

Y. Zhujun (2018), ix, 139 pp

ISBN: 978-3-95806-356-3

Band / Volume 437

Characterization of High Temperature Polymer Electrolyte Fuel Cells

Y. Rahim (2018), iii, 162 pp

ISBN: 978-3-95806-359-4

Weitere **Schriften des Verlags im Forschungszentrum Jülich** unter
<http://wwwzb1.fz-juelich.de/verlagextern1/index.asp>

Energie & Umwelt / Energy & Environment
Band / Volume 437
ISBN 978-3-95806-359-4